Corrosion Protection Properties of Formed, Organically Coated Electro-galvanised Steel

PhD Thesis

Dr. rer. nat.

Faculty of Science

at the

University of Paderborn

Submitted by

Ingo Klüppel

from Düsseldorf

Paderborn, 2008

Defence on December 5, 2008

First referee: Prof. Dr.-Ing. Guido Grundmeier

Second referee: Prof. Dr. Wolfgang Bremser

Acknowledgements

The present work was carried out between June 2004 and June 2007 at the Dortmunder Oberflächencentrum (DOC), a company of ThyssenKrupp Steel and the Max-Planck-Institut für Eisenforschung (MPIE).
I want to thank Dr.-Ing. Michael Steinhorst and Prof. Dr. Martin Stratmann for giving the opportunity to work at both the DOC and the MPIE and Dr. Christoph Filthaut for working in his group.

My special thanks go to Prof. Dr.-Ing. Guido Grundmeier, my workgroup leader at the MPIE and my first referee at the University of Paderborn. He was always ready to listen to questions and gave productive advice for solving problems that occurred during this thesis.
I also would like to thank my tutor at the DOC Dr.-Ing. Bernhard Schinkinger who introduced me to the industrial work and gave me a lot of hints for following in his foodsteps.

Prof. Dr. Bremser gets my acknowledgement for taking over the refereeing of my thesis and the support with polyelectrolytes synthesised by Dr. Oliver Seewald.

Further thanks go to my roommates Dr. Krasimir Nikolov, Dipl.-Ing. Richard Weinhold, Dipl.-Phys. Tobias Titz and Dipl.-Phys. René Vlasak for their discussions which were sometimes not content-related but always interesting and rewarding. These discussions went on with Dr. Miroslaw Giza during our travel times by train and car, I also thank him.
There are a lot more people at both DOC and MPIE I would like to thank but the space would not suffice to name all of them.
I wish to thank the Fraunhofer Group at the DOC for supporting me by the laser cutting of the miniature and corrosion samples. I am grateful to the group of Dr. Kessler for its help in analysing the forming behaviour of the different samples. Many thanks go to Mr. Petzold for some of the FE-SEM images.

Last but not least I would like to thank Lirija, my parents and my sister for their support and patience during the preparation of this work.

The work was carried out with a financial grant from the Research Fund for Coal and Steel of the European Community (contract no. RFS-CE-04031).

Index

Symbols

A	cross section, breaking elongation, area
B	rotation constant
C	capacitance
c	concentration, speed of light
C_f	quartz sensitivity factor
D	spring constant
d	thickness, piezoelectric tension module
E	voltage, absorbance
E_{loc}	electromagnetic field
e	Euler constant
F	force
F(J)	rotation term
f	frequency
h	Planck constant, height
I	current, intensity of light
I_{corr}	corrosion current
J	rotation quantum number
k	absorption factor
L	elongation, length, induction
m	mass
N	number of molecules
n	harmonic number
P	power of ion beam
R	resistance
R_e	elastic limit of deformation
R_p	polarisation resistance
$R_{p,0.2}$	0.2 % plastic deformation
R_m	maximum strength during deformation
r	radius
t	time
w	width

x	extension, length
Z	impedance
Δm	mass change
Δf	frequency change
ΔJ	quantum number of rotation
ΔT	temperature difference
Δv	quantum number of vibration
Φ	phase shift
α	polarisability
β_a	anodic coefficient
β_c	cathodic coefficient
ε	decade absorption coefficient
ε_0	dielectric constant in vacuum
ε_r	dielectric constant of a certain material
ε_{el}	sum of plastic and elastic deformation
ε_{us}	area of uniform deformation
ε_{H2O}	dielectric constant of water
κ	thermal conductivity
λ	wave length
μ	reduced mass, dipole moment
μ_q	effective piezoelectric stiffened shear modulus
ν	frequency
π	Pi
ρ	solution resistivity
ρ_q	quartz density
φ	logarithmic forming degree, water uptake
ω	radial frequency

1 Motivation

Coil coated steel is a composite material of a normally galvanised steel coated with one or more organic layers. It is one of the premium products of the steel industry and gives large benefits to the costumer like the effort reduction in their paint shops and further improvements in corrosion resistance. Furthermore the coil coating facilities are equipped with comprehensive waste water recycling and exhaust gas cleaning systems which allow a much more environmentally friendly production than the coating of bulk goods.

The continuous production process is based first on an alkaline cleaning step to provide an optimal surface of the galvanised steel coil. Afterwards the pretreatment and the organic lacquer layers are applied by roll coaters in the thickness of some nm for the pretreatment and some µm for the organic coating. The cross linking of the coating can be done by classic thermal curing or in recent times by radiation curing where e.g. UV or IR radiation is used. Finally the coated steel is coiled again and ready for the further production steps at the customer facilities.

The flexible lacquer choice allows the production of optimised products for the different demands which find a wide use in the household, building and automobile industry. Typical household products that are made of coil coated steel are so called white goods (named according to their colour) such as dish washers, refrigerators and washing machines. The building industry uses pre-coated steel for the construction of dividing walls, cladding and roof elements. In both industries, household and building, the colour appearance, corrosion, UV and chemical resistance are the major demands.

The automotive industry uses coil coated material mainly in the form of corrosion protection primers. These are thin pigmented, organic coatings (about 2 – 4 µm) which are applied on galvanised steel and give a further improvement of the corrosion protection properties of the substrate by the formation of a barrier layer. This allows the improvement of guaranteeing or the reduction of secondary corrosion protection measures for the built cars. Next to the good corrosion properties the coatings have to be weldable, glueable, must show good forming features and must not disturb the further production steps during the car manufacturing process, like phosphating and ED-paint application. Fig. 1 shows the typical production cycle of coil coated material by the example of corrosion protection primers.

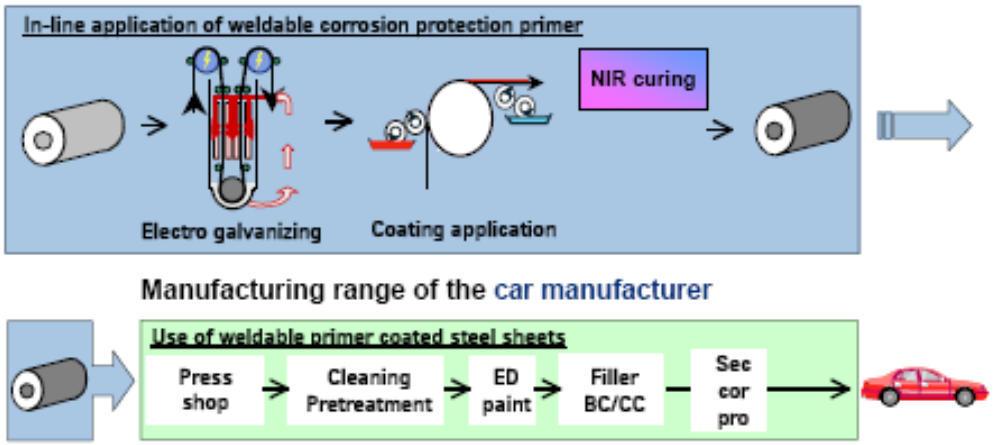

Fig. 1. Production and application way of weldable corrosion protection primers for the automotive industry

The formability of organic coatings on steel is a precondition for the application of pre-coated (coil-coated) steel in various technical applications. Especially at high forming degrees or at cut edges, defects appear within the organic coating. These defects influence the ensuing processing technology as well as the long-term stability of the material.

The mechanical stress induced by the forming process leads to a reduction of the coating thickness and the formation of cracks inside the organic matrix as well as at the pigment/binder interfaces [1, 2]. This induces a loss of barrier properties [3, 4]. The loss of corrosion protection of the layered material depends on the defect size, location, change in the adhesion to the substrate and also on the surface modification steps applied subsequently.

It is therefore extremely important to correlate the forming degree with the change in the barrier and structural properties of the coating.

Methods of investigating these barrier properties are common industrial tests like salt-spray or cyclic corrosion tests, during which the lifetime of the coating is investigated in relation to the forming degree [5]. These tests have the disadvantage of a long testing period and high rates of systematic errors resulting from the visual evaluation by the operator.

Another well established way of monitoring the barrier properties of organic coatings in contact with corrosive solutions is Electrochemical Impedance Spectroscopy (EIS) [6-28].

Recently Bastos et al. were able to show that ex-situ EIS is a powerful tool for correlating the barrier properties of an organic coating with the local degree of forming [29].

Dynamic Electrochemical Impedance Spectroscopy was used by Darowicki et al. for the in-situ monitoring of the passive layer cracking on 304L stainless steel and for evaluating the performance of organic coatings under periodical stress [30, 31].

The aim of the present work was to investigate and understand the defect formation and self-healing properties of organic coatings like corrosion protection primers. Therefore, a new electrochemical setup had to be established that allows the monitoring of electrochemical impedance spectra with a common three electrode arrangement during the uniaxial forming of a miniaturised model sample. This setup should allow a detailed correlation between the forming degree and the barrier properties of the organic coating. The correlation is necessary for predicting the maximum forming degree suitable for an organic coating during the construction.

Furthermore, new setups for the combined spectroscopic and electrochemical analysis should be developed which allow investigating the formation and characterisation of corrosion products and the absorption kinetic of inhibitors used in organic coatings. This allows a fast and comprehensive analysis of the efficiency and reactivity of new inhibitors and helps to follow the self-healing potential of polymeric coatings.

Finally a new coating system the so called polyelectrolytes were investigated with respect to their formability and curing state in order to understand the defect formation of lower cross linked coatings which should be highly flexible. They are promising lacquer systems that could provide huge benefits for corrosion protection as they can be specially tailored to the different applications [32-46]. These flexible coatings should lead to a reduced defect formation within the coating and thereby increase barrier properties.

The electrochemical measurements will be complemented by the Field Emission Scanning Electron Microscopic (FE-SEM) and Focused Ion Beam (FIB) analyses to visualise the location and size of the formed defects. The local reactivity should be correlated with the formation of defects by means of a phosphating process and the common corrosion test.

2 Fundamentals

2.1 Forming of polymer coated metals

2.1.1 Forming of metals

In the solid state metal atoms are regularly arranged and form a lattice of close-packed balls. Within the material the atoms form small crystals (grains); these grains have slightly different orientations to each other. The size of grains can vary from some micrometres up to some millimetres. During the forming process the atoms move against each other within the lattice. At grain boundaries between the single crystals the movement is hindered and requires a much higher strength. Therefore, micro crystalline materials show a much higher maximum strength.

The mechanical properties of metals can be evaluated by so-called elongation-strain diagrams. The amount of elongation in the different directions in space is expressed by the forming degree which is furthermore used to define the forming limit expressed in the forming limiting curve (FLC) of the material under investigation [47, 48].

2.1.1.1 Stress-Strain diagram

Forming is the shape change of a material induced by an external force. Forming of metals can be divided into a reversible, elastic and irreversible plastic deformation. The mechanical properties of a material are shown in a Stress-Strain diagram. Fig. 2 shows the strain-elongation diagram of a DC 06 ZE 75/75 steel sheet (thickness 0.8mm), a typical material used for deep drawing. The diagram can be separated into the following parts:

- Hook's straight, area of elastic tension. The material behaves like a spring and returns to its original form according to Hook's law

$$F = D \cdot \Delta l \qquad \textbf{(eq. 1)}$$

with F the force, D the spring constant and Δl the elongation.

- The end of Hook's straight is called elastic limit R_e. At this point the plastic deformations starts and the material will get a permanent shape change.

- Most metals don't show a defined elastic limit. Therefore, a limit at the 0.2 % plastic deformation will be defined ($R_{p0.2}$). The overall elongation is thereby the sum of the elastic elongation (ε_{el}) and the plastic deformation. At the point $R_{p0.2}$ the elastic elongation can be calculated accordingly.

$$\Delta\varepsilon_{el} = \varepsilon_{R_{P0.2}} - 0.2\% \qquad \textbf{(eq. 2)}$$

- The maximum in the diagram is called tensile strength (R_m). Until R_m the sample will be formed without constriction and the area is called uniform strain (ε_{us}).

- Beyond R_m the samples constrict and the further forming until breaking elongation (A) only appears in that area.

Typical mechanical properties for different deep drawing steel grades are given in Tab. 1.

Tab. 1. Mechanical properties of typical deep drawing steel grades according to DIN EN 10130

Steel grade	**$R_{p0.2}$ / MPa**	**R_m / MPa**	**A / %**
DC 01	140 - 280	270 - 410	≥ 28
DC 03	140 - 240	270 - 370	≥ 34
DC 04	140 - 210	270 - 350	≥ 38
DC 05	140 - 180	270 - 330	≥ 40
DC 06	140 - 180	270 - 350	≥ 38

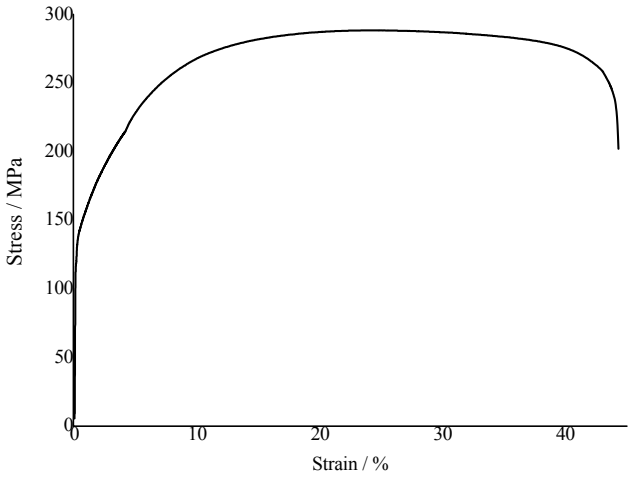

Fig. 2. Stress-Strain diagram of a tensile tested DC 06 ZE 75/75 sample (sheet thickness 0.8mm)

2.1.1.2 Elastic and plastic deformation of single crystals

The deformation of metals can happen in an elastic and inelastic way. During the elastic deformation the induced stress leads according to Hook's law to a linear translation (eq. 1). In the case of a single crystal the induced stress causes deformation in the lattice. The deformation is so small, that after removing the external force the atoms return to their origin (Fig. 3).

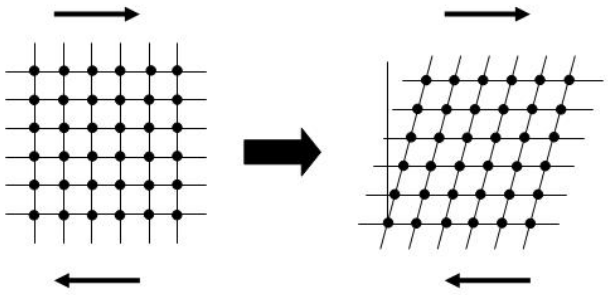

Fig. 3. Elastic deformation of a single crystal lattice during application of external stress (according to [48])

With increasing strain the elastic deformation leads to the plastic deformation of single crystals which consist of two mechanisms, the formation of twins and the sliding.

The formation of twins appears along the twin plane, thereby a part of the lattice will be transformed into a mirror image of the original one (Fig. 4).

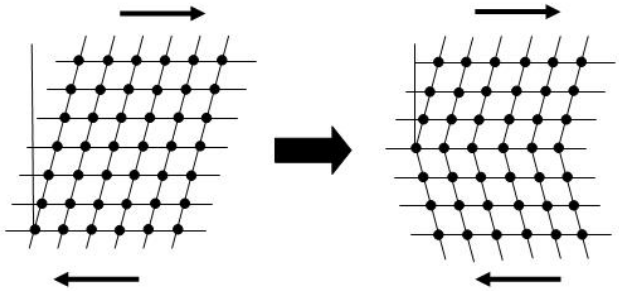

Fig. 4. Formation of twins in single crystals due to external stress (according to [48])

Sliding can be separated into the fixed sliding and the sliding by moving of dislocations. Fixed sliding only appears if all atoms on both sides of the sliding plane are simultaneously moved (Fig. 5). The length of one step is similar to the lattice constant (b).

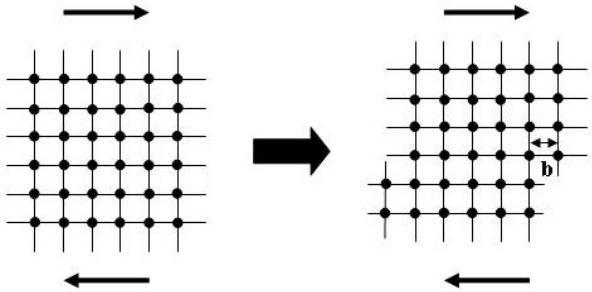

Fig. 5. Fixed sliding along the sliding plane by the length of the lattice constant b (according to [48])

Technical materials differ from ideal crystals by the formation of lattice defects. The reduction of bonds between the atoms leads to a decrease of the force which is necessary for moveing the atoms along the sliding plane (Fig. 6).

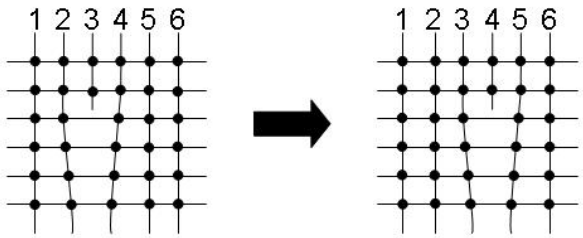

Fig. 6. Defect migration during the formation of non-ideal crystals (according to [48])

This explains the 100 – 1000 times smaller value found for the shear stress of materials containing dislocations [48].

2.1.1.3 Forming of zinc and electrogalvanised zinc surfaces

Zinc crystallises into a hexagonal lattice structure with a height to edge ratio (c/a) of 1.856 [49]. Due to the complex and high anisotropic structure hexagonal systems show only 6 basal slip systems [48]. These preferred sliding planes (in direction c) can be activated by a tension of at least 0.3 MPa. For the activation of non-basal sliding (pyramidal sliding or twinning) a shear stress which is 30 times higher has to be applied perpendicular or parallel to the basal plane. During the uniaxial elongation a heterogeneous forming with sliding on the grains, recrystallisation and the formation of twins occur [49].

The electrogalvanised zinc coating of steel shows the formation of parallel terraces with a 0001 orientation. Two cases of microstructure can be divided depending on the deposition conditions. For hot electrolytes and low current densities the basal plane of the zinc lattice are tilted between 35 – 55° to the steel substrate. In contrast to that for low temperatures and high current densities the basal planes are mainly parallel to the substrate. Due to the crystal structure and the ductility mainly basal plane slipping appears during plastic deformation. Here the orientation of the sliding planes to the direction of strain is of great importance. Grains with their basal planes in the direction of the strain can undergo a much higher local forming than the global forming degree. The zinc coating shows no formation of defects during the forming until the rupture of the steel substrate [50].

2.1.1.4 Forming degree

The shape change of a body by deformation is quantified by the deformation degree. Two deformation degrees can be separated. First the logarithmic forming degree φ and second the based forming degree ε which is normally written as a technical deformation in percent. In this work only the logarithmic forming degree will be used.

In eq. 3 and 4 the derivation of the logarithmic deformation degree is shown. The change of φ is based on the actual dimensions of a body l and the length change dl. By solving the integration of eq. 3 φ is defined as the logarithm of the ratio before (l_0) and after deformation (l_1).

$$d\varphi = \frac{dl}{l} \quad \textbf{(eq. 3)}$$

$$\varphi = \int_{l_0}^{l_1} \frac{dl}{l} = \ln \frac{l_1}{l_0} \quad \textbf{(eq. 4)}$$

For the description of a forming process three forming degrees are defined (one for each direction in space). The different degrees are marked by the index 1, 2 and 3. Index 1 indicates the major strain, this is the direction in which the highest dimension change happens. In case of a simple tensile test it is the direction of the elongation. Index 2 displays the minor strain which is the width change of the sample. The last deformation degree with index 3 describes the thickness change of the sheet.

Using the logarithmic deformation degree leads to certain advantages. The sum of the deformation degrees is independent of the numbers of deformation steps (eq.5). Due to the fact that the volume of the formed body is constant the sum of all three forming degrees is zero (eq. 6) [48].

$$\varphi_{tot} = \sum_{i=1}^{n} \varphi_i \quad \textbf{(eq. 5)}$$

$$\varphi_1 + \varphi_2 + \varphi_3 = 0 \quad \textbf{(eq. 6)}$$

2.1.1.5 Forming-limiting-diagram

The forming of metal sheets can be divided into four major groups: uniaxial, biaxial, plane strain and deep drawing. These are separated by the different interconnections of the deformation degrees.

The simplest way of forming is the uniaxial deformation. It appears during tensile testing. Thereby the sample will be elongated in the direction of φ_1 while the width φ_2 decreases. In eq. 9 the interaction between the major and the minor strain is given. Uniaxial forming often appears during the production of real automotive parts.

$$\varphi_1 = -2\varphi_2 \quad \textbf{(eq. 7)}$$

Biaxial forming is also known as stretch-forming. The sample will not only be elongated in one direction as known from the uniaxial forming but in two directions φ_1 and φ_2 (eq. 8). Biaxial forming leads to high stresses in the material and is unusual for most automotive parts. This way of deformation is used for material investigations and needs especially shaped samples like Marciniak or Nakajima specimen where the material is hindered by the blank holder from flowing into the form [48].

$$\varphi_1 = \varphi_2 \qquad \textbf{(eq. 8)}$$

Plane strain deformation is often found in real automotive parts. The forming only appears in direction of the major strain φ_1 and by a change in the sheet thickness φ_3. The minor strain φ_2 remains constant during the whole process (eq. 9). In this forming process the material flow is similar to the biaxial forming which is hindered by the blank holder.

$$\varphi_2 = 0 \qquad \textbf{(eq. 9)}$$

During deep drawing the metal sheet will be formed by a stamp similar to the biaxial and plane strain forming. The difference is that the blank holder force is negligible or adjusted to such small forces that the material flow is not hindered. Thereby the width φ_2 will be reduced by the same amount as the length φ_1 will be increased (eq. 10). The thickness of the sheet will be constant during the forming procedure.

$$\varphi_1 = -\varphi_2 \qquad \textbf{(eq. 10)}$$

The whole forming process is described by three deformation degrees and the connection between them is completely different for the four major forming procedures. This makes it extremely difficult to compare different deformations just by a look at the deformation degrees. Therefore von Mises defined the equivalent strain (eq. 11) which allows an easy comparison of the forming processes [47, 48].

$$\varphi_v = \sqrt{\frac{2}{3}\left(\varphi_1^2 + \varphi_2^2 + \varphi_3^2\right)} \qquad \textbf{(eq. 11)}$$

For the forming process it is of great interest to get detailed information about the maximum strain that can be applied to the material before it breaks. In the forming limiting diagram the major strain φ_1 is plotted versus the minor strain φ_2 and the forming limiting curve shows the maximum strain before rupture (Fig. 7).

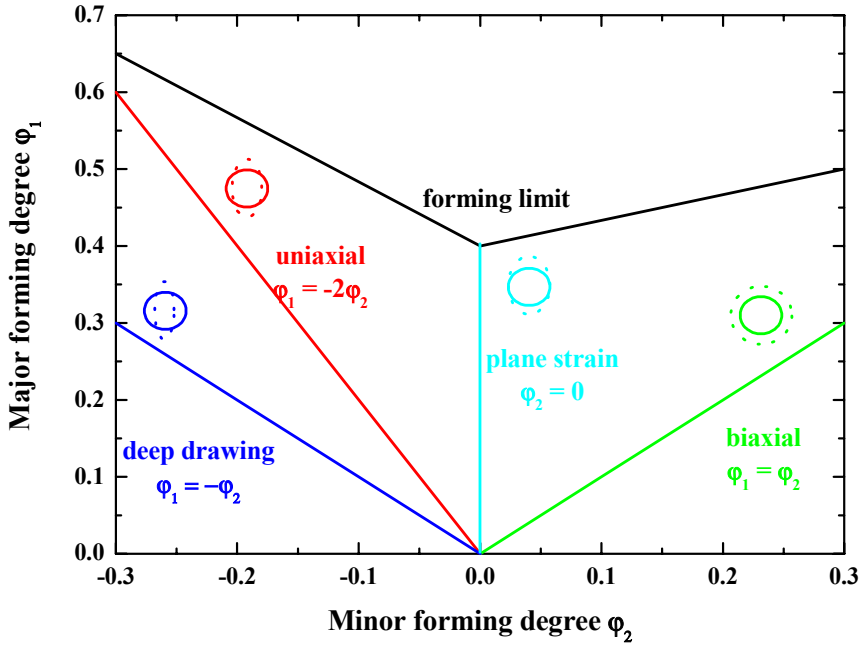

Fig. 7. Forming limiting diagram indicating the maximum forming degrees possible for the material (black line) and the major forming operations

During the production of formed parts it is important to be 10 % below this curve to guarantee the necessary process reliability.

2.1.2 Forming of polymers and thin polymer films

2.1.2.1 Molecular understanding

In contrast to metals that consist of single atoms which form a crystalline grid, polymers consist of long molecule chains. Depending on the chemistry and the production parameters of the polymer these chains can also form partly crystalline areas. Molecules with only few branches have a high tendency to form crystalline areas while strongly cross-linked and branched molecules are mainly amorphous. Furthermore the cooling speed after the production influences the arrangement of the molecules. Low cooling rates strongly increase the number of crystalline areas in the polymer. The different crystalline structures of polymers show also different behaviours during forming. On the one hand they can be brittle and break already at small elongations on the other hand they behave elastically and can be highly elongated. The forming behaviour is strongly dependent on temperature and can change from brittle at low degrees to elastic at higher degrees [51].

Brittle polymers show just a linear increase in the strain until they break. Partly crystalline polymers show a high stretch ability before rupture due to the intricate structure of the molecules. During elongation the molecule fibres orient themselves into the direction of the applied force and reach a stress maximum (Fig. 8).

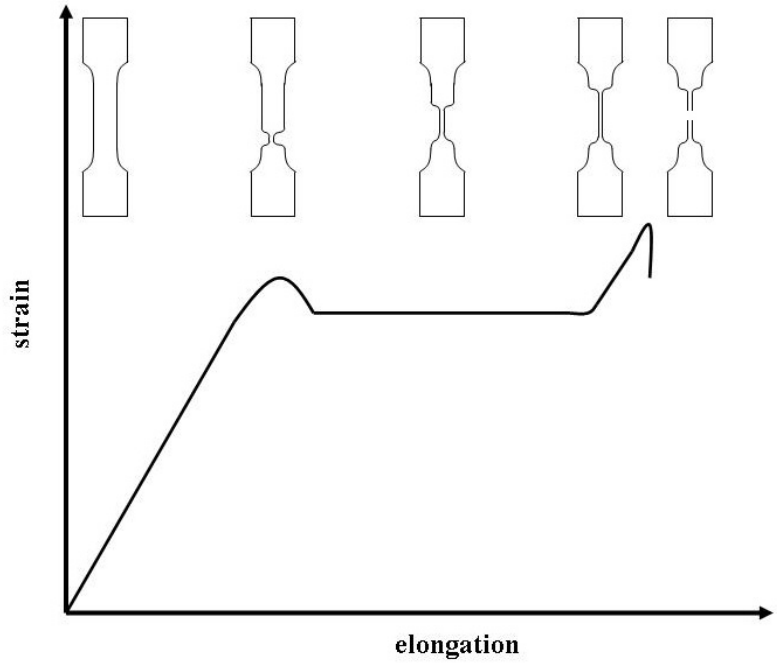

Fig. 8. Stress-strain diagram of a polymer under tensile stress showing the different areas of elastic and plastic deformation until rupture (according to [51])

With further elongation the sample starts to constrict and the stress decreases until it reaches a plateau. Further elongation doesn't lead to an increase in the stress over a large strain range. In this region the crystalline parts break up and the molecule fibres become parallel. When all fibres are arranged in parallel the strain strongly increases again until the polymer ruptures. Elastomeres don't show a specific maximum and only a slightly defined plateau. The strain increases nearly continuously until the rupture.

2.1.2.2 Relevance of interfaces

Beside the formability of the polymer itself the interface between the coating and the metallic substrate is of great importance. The interface is responsible for the adhesion of the coating to the substrate. Weak adhesion leads to detachment or the delamination of the organic layer and thereby to a loss of the barrier properties which accelerate corrosion. Typical industrial tests for analysing the adhesion after forming are the Erichsen cupping and the ball impact [52]. Both lead to a biaxial forming of the specimen and an adhesive tape is used for testing the adhesion.

A lot of work was done to stabilise the coating / substrate interface. One of the best-known and widely used processes is phosphating [53]. Hereby the etching attack of the metallic surface leads to a precipitation layer of phosphate crystals with a thickness between 1 and 50 µm. The micro rough surface structure of the phosphate layer allows a good mechanical interlocking with the following coating and thereby increases the adhesion. The phosphate crystals also act as a further barrier and thereby improve the corrosion resistance of the system. Commonly this effect is increased by a passivation step after phosphating. Recently it was changed from Cr (VI) passivation to Chromium free passivation.

In the case of coil coatings the pretreatment consists of ultra thin layers in the range of some nm, which allows a Chromium free passivation of the substrate and increases the paint adhesion [54-58] (Fig. 9).

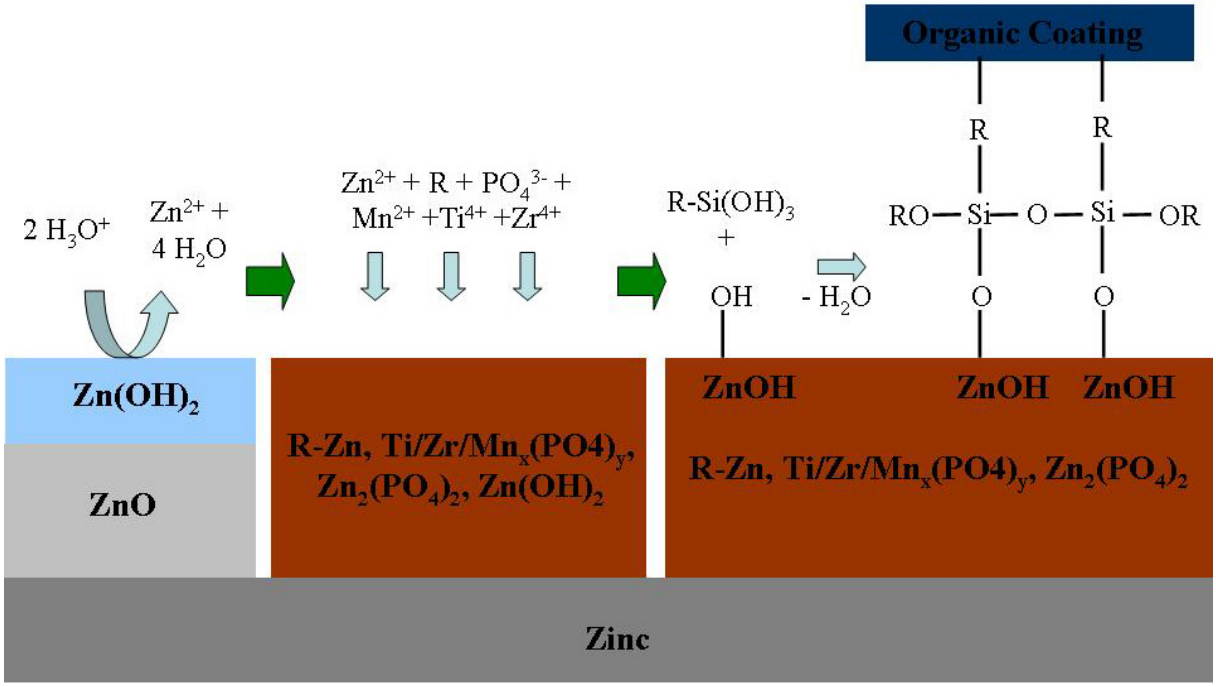

Fig. 9. Schematical illustration of the pretreatment (Granodine 1456) layer formation on a zinc surface including an organo silane adhesion promoter

For the surface passivation mainly salts of Manganese, Titanium and Zirconium in combination with complexing agents and phosphoric acid are used. Together they form with the dissolved zinc ions a protective precipitation layer on the zinc surface. The adhesion promotion is achieved by chemical bonding of bi-functional organo silanes between the organic coating and the zinc substrate.

2.1.2.3 Theory of crack formation in polymers and at polymer / oxide interfaces

The defect formation within polymers or at the polymer / oxide interface strongly depends on the adhesion along the interface. In the case of a weak adhesion the coating delaminates from the substrate and an adhesive failure is formed. If the adhesion between the coating and the substrate is good the stress inside the coating can reach high values until the polymer cracks by cohesive failure. If the load is applied uniaxially to the system the cohesive defects will grow perpendicular to the stress direction and new cracks appear mainly in the middle of existing fragments [59].

In the case of welded polymers the crack formation mechanism depends strongly on the interface width between the polymers. For most polymers three regimes were found which can be attributed to different failure mechanisms. For small interface widths the interdiffusion

of polymer chains is only very weak and they are pulled out of the opposite polymer. With increasing interface widths the separation is done by pull out and by chain scission of the polymers. For high values of interdiffusion the main mechanism is the chain scission and the force reaches the value of the bulk adhesion [60].

Moloney et. al. show that in front of the crack tip propagating within a highly crosslinked, unfilled epoxy resin a zone of micro cracks is formed [61]. The filling of polymers can lead to a toughening of brittle polymers. Thereby the particles initiate a high number of very small local yield events. Examples are inorganic particles which lead to a large number of microcracks and a reduction of the local stress. Another way is the implementation of ductile particles which are plastically formed by the crack tip and help bridging the two sides of the crack [62].

The propagation of a crack can be stopped if the crack hits e.g. a local volume of higher strength, a weak second phase or another microcrack and the propagation into an unloaded region between other cracks or strong fibres [62].

2.1.3 Repair mechanisms of defects in protective coatings

The repair mechanisms of defective coatings can be divided into two major groups. On the one hand are the traditional ways of repairing the defects by e.g. welding and patching, on the other hand are the recently developed self-repair systems that heal the defects without external support [63-73]. The traditional repair processes are mainly used for macroscopic defects while the self-repair focuses on the healing of microscopic defects as they might occur during forming [74].

Self-healing can appear if the two sides of a defect are still in contact with each other and the system is above its glass temperature. Than the crack heals due to molecular diffusion across the interface [75]. Other mechanisms are the recombination of chain ends by the catalytic redox reaction under oxygen atmosphere, the use of living polymers with radical functions at the chain end and the inclusion of reservoirs that contain a healing agent [75].

Two different approaches were developed as reservoirs, the hollow fibre and the microencapsulation. In the first case the glass fibres ranging from of 15 to 60 µm in diameter were filled with a healing agent and embedded into the coating. If a defect hits such a fibre it breaks and the crack will be filled with the healing monomer that cures within. The microencapsulation works similar to the hollow fibre but instead of a fibre micro capsules are used which are embedded together with a catalyst into the coating. The propagating crack

front ruptures the microcapsules and the released healing agent reacts with the embedded catalyst and seals the defect [63, 74, 76-78].

A further recently described method for healing defects in protective coatings is the use of expandable materials like phyllosilicates (clays) [79]. If they are exposed to air inside a crack these materials will absorb moisture and implement the water into their crystal structure. This leads to a lattice growth and allows the defect to be filled.

Another approach is the intelligent and controlled release of inhibiting agents into defects to passivate these corrosion sites. Shchukin et. al. describe the pH controlled release of benzotriazol from nano particles and tubes due to the response of polyelectrolytes to a pH shift. At low or high pH, as they appear at the cathodic or anodic corrosion sites, the polyelectrolytes become permeable for the inhibitor. The release rate can be adjusted by the properties of the used polyelectrolytes [80]. Paliwoda-Porebska et. al. show that the inhibitor $[PMo_{12}O_{40}]^{3-}$ can be potentially released from conductive polymers (polypyrrole) [71] and leads to a reduction of the cathodic delamination of coatings. Thereby the reduction of the polymer film due to the corrosive reaction leads to the release of the inhibitor.

3 Fundamentals of applied microscopic, spectroscopic and electrochemical methods

3.1 Electrochemical Impedance Spectroscopy

Electrochemical Impedance Spectroscopy (EIS) is widely used in material and surface science to investigate the properties of e.g. metallic substrates, batteries and fuel cells [81-95]. A special focus is thereby set on the characteristics of polymer coatings. One of the key features is the barrier properties of coatings over time which are in contact with a corrosive electrolyte on order to gain information about the corrosion protection. Mansfeld describe in detail the used equivalent circuit and the interpretation of data [96]. Further focus was laid on the evaluation of the water uptake of organic coatings [19, 97-102]. In recent times EIS was used to investigate ultra thin conversion coatings [55, 58] and zinc rich coatings [103-105]. The combination of EIS with spectroscopic tools like FTIR to observe the water uptake was also developed by different groups [106-108].

3.1.1 General description of the impedance

The behaviour of an ideal resistor which hinders the current flow in a circuit is described by Ohm's law (eq. 12). The resistor R follows the law at all currents I and voltages E and its value is independent of the applied frequency. The current answer to an applied AC voltage is always in phase [109-111].

$$E = R \cdot I \qquad \textbf{(eq. 12)}$$

The description of Ohm's law can only be used in the case of the ideal resistor. A much broader approach to handle the resistance of a circuit is the impedance which is not limited to the simplifications mentioned above. The electrochemical impedance is measured by applying a sinusoidal potential excitation to an electrochemical cell. The current answer will be analysed and the impedance can be calculated.
The frequency f in Hz used for the voltage modulation can also be written by the radial frequency ω in radians / second (eq. 13).

$$\omega = 2\pi \cdot f \qquad \textbf{(eq. 13)}$$

The applied excitation voltage E_t has as a sinusoidal function of time and can be described by eq. 14.

$$E_t = E_0 \sin(\omega t) \quad \textbf{(eq. 14)}$$

The response of the current I_0 will be shifted in phase by a certain angle ϕ (eq. 15).

$$I_t = I_0 \sin(\omega t + \phi) \quad \textbf{(eq. 15)}$$

The dependence between the applied voltage and the phase shifted current answer is shown in Fig. 10.

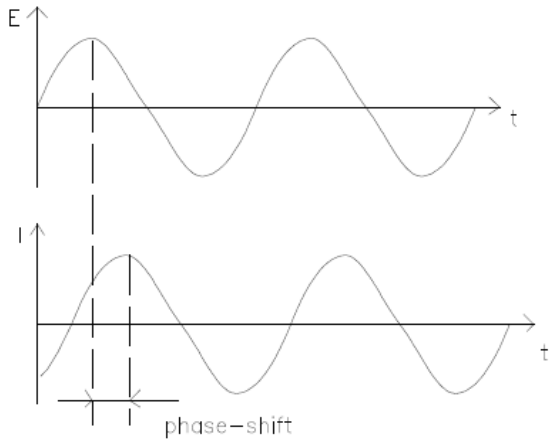

Fig. 10. Phase shift between a sinusoidal excitation voltage and the current response (taken from [112])

The impedance can be described similar to Ohm's law with the time dependent voltage and current. The magnitude of the impedance is expressed by $|Z|$ (eq. 16).

$$Z(\omega) = \frac{E_t}{I_t} = \frac{E_0 \sin(\omega t)}{I_0 \sin(\omega t + \phi)} = |Z| \frac{\sin(\omega t)}{\sin(\omega t + \phi)} \quad \textbf{(eq. 16)}$$

The Euler relation allows the transformation of the voltage and current into a complex function (eq. 17-20). It can be described by a real and an imaginary part.

$$E_t = E_0 \cdot e^{(i\omega t)} \quad \textbf{(eq. 17)}$$

$$I_t = I_0 \cdot e^{(i\omega t+\phi)} \quad \textbf{(eq. 18)}$$

$$Z(\omega) = |Z| \cdot e^{(i\phi)} = |Z|(\cos\phi + i\sin\phi) \quad \textbf{(eq. 19)}$$

$$Z(\omega) = \mathrm{Re}\,Z + i\,\mathrm{Im}\,Z \quad \textbf{(eq. 20)}$$

The real part Re and the imaginary part Im are given by eq. 21 and 22.

$$\mathrm{Re}(Z) = |Z|\cos\phi \quad \textbf{(eq. 21)}$$

$$\mathrm{Im}(Z) = |Z| i\sin\phi \quad \textbf{(eq. 22)}$$

3.1.2 Plotting of impedance data

Two ways of plotting the impedance data are common in electrochemistry. The Nyquist plot displays the imaginary part on the y-axis and the real part on the x-axis (Fig. 11). The plot is based on a simple vector plot; every impedance data on the semicircle can be displayed by a vector. The length of the vector is the impedance $|Z|$ while the angle between the x-axis and the vector is the phase shift ϕ. The major disadvantage of the Nyquist plot is that the frequency at any data point can not be taken from the diagram.

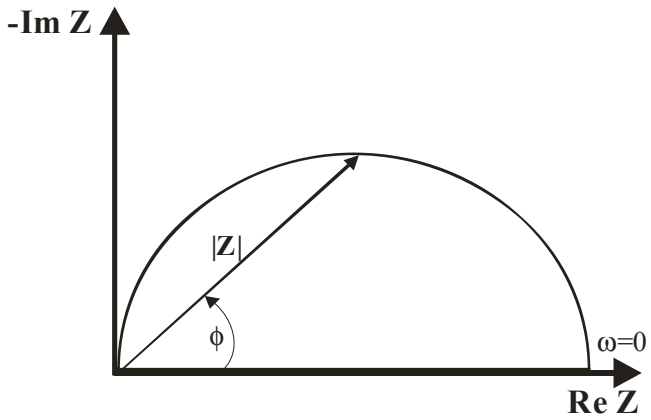

Fig. 11. Schematical Nyquist plot of a metal electrode indicating the phase shift (ϕ) and the impedance shown as vector ($|Z|$)

Another way of presenting the impedance data is the Bode plot (Fig. 12).

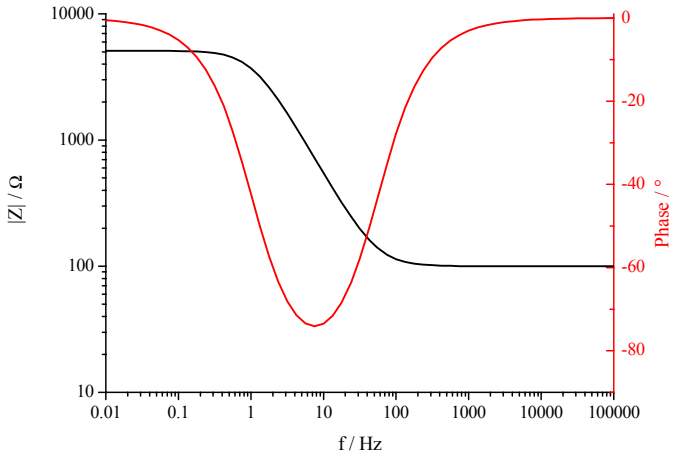

Fig. 12. Schematical Bode plot of metallic substrate showing the impedance (black) and the phase shift (red)

The logarithm of the impedance $|Z|$ is plotted on the y-axis while the logarithm of the frequency is plotted on the x-axis. The phase shift ϕ is thereby plotted on a second y-axis. The Bode plot allows an easy interpretation of the electrolyte resistance (at high frequencies) and the polarization resistance (low frequencies) in simple equivalent circuits.

3.1.3 Pseudo-Linearity of the system

The measurement of impedance spectra can take hours depending on the selected frequency range. During the whole measurement it is necessary that the system is in a steady state and will not change with time. Changes in the system can be caused by temperature changes, adsorption of molecules, degradation of the coating and so on. These effects might lead to misinterpretations of the results.

A further quite important point is the linearity of the system under investigation. In the case of an ideal ohmic resistor the current increases linearly with the applied voltage. For an electrochemical cell this linearity is not strictly given (Fig. 13). Therefore it is necessary to create a pseudo linear system [112].

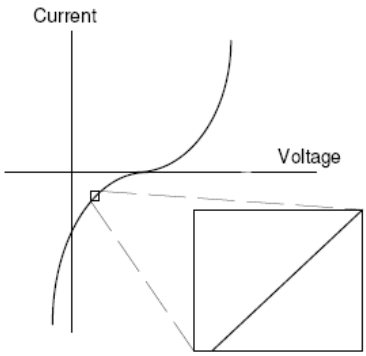

Fig. 13. Pseudo linearity of an electro chemical system if a small excitation voltage is used (taken from [112])

If the excitation of the system is very small (1-10 mV) the system can be supposed as pseudo linear.

3.1.4 Elements of the equivalent circuit

For the interpretation of impedance data commonly known electrical elements are taken and an equivalent circuit will be modelled. Each element stands for a certain electrochemical property. The most common properties are described in Tab. 2 [112, 113]:

Tab. 2. Common electrical element

Component	Current vs. Voltage	Impedance
Resistor R	$U = R \cdot I$	$Z = R$
Capacitor C	$I = C\frac{dU}{dt}$	$Z = \frac{1}{i\omega C}$
Inductor L	$U = L\frac{dI}{dt}$	$Z = i\omega L$

3.1.4.1 Electrolyte resistance

Even by the use of Haber-Luggin-Capillaries, which allow the positioning of the reference electrode directly in front of the working electrode, the resistance of the electrolyte between the reference and the working electrode cannot be completely eliminated. This impedance is found in the spectra as an ideal ohmic resistor which dominates at high frequencies and

ranges from 10 - 100 $\Omega \cdot cm^2$ for common setups. The uncompensated electrolyte resistance R_u is defined as

$$R_u = \rho \frac{l}{A} \quad \textbf{(eq. 23)}$$

With ρ the solution resistivity, A the area and l the length.

3.1.4.2 Double layer capacitance

If an electrode is in contact with an electrolyte, ions from the solution can stick to the electrode surface by van der Waals or Coulomb forces. The charges in the electrolyte and at the electrode boundary are of opposite sign and form a capacitor. Due to the small distance of just a few Ångström between the charge carriers extremely high capacitances of 10 to 40 µF/cm² can appear.

3.1.4.3 Polarisation Resistance

Whenever an electrode is polarised a current flow at the electrode surface can occur due to an electrochemical reaction. This leads to either an anodic or cathodic current whose density is controlled by the kinetics of reaction and diffusion of the reactants. In case of a metal electrode that corrodes at the open circuit potential two electrochemical (a cathodic and an anodic) reactions appear at the electrode surface. At the open circuit potential the current of both reactions are equal and it is known as the corrosion current. The current of a kinetically controlled reaction can be described by the Butler-Volmer equation. In the case of a mixed electrode it can be written as eq. 24.

$$I = I_{corr}\left(e^{\frac{2.303(U-U_{OC})}{\beta a}} - e^{\frac{-2.303(E-E_{OC})}{\beta c}}\right) \quad \textbf{(eq. 24)}$$

With I the cell current, I_{corr} the corrosion current, E_{oc} the open circuit potential, β_a the anodic coefficient and β_c the cathodic coefficient.

If only a small potential signal is applied to the cell the eq. 24 can be simplified to eq. 25 with R_p the polarisation resistance.

$$I_{corr} = \frac{\beta_a \beta_b}{2.303(\beta_a + \beta_c)} \cdot \left(\frac{1}{R_P} \right) \qquad \textbf{(eq. 25)}$$

3.1.4.4 Coating capacitance

The capacitance of a coating can be described by a plate condenser. The condenser consists of two plates formed by the surface or the electrode and the electrolyte. Between these two plates the coating exists as a dielectric. The capacity C of the condenser is proportional to the plate area A, the dielectric constant of the vacuum ε_0, the dielectric constant of the material between the plates ε_r and inverse proportional to the thickness of the dielectric d (eq.26).

$$C = \frac{\varepsilon_0 \cdot \varepsilon_r \cdot A}{d} \qquad \textbf{(eq. 26)}$$

3.1.5 Modelling of equivalent circuits

For the interpretation of impedance data so-called equivalent circuits are built from simple electrical elements like resistor, capacitor and inductor. The equivalent circuits reflect the physical properties of the electrode under investigation. Some of the most common circuits are shown in the following chapters [8, 13, 28, 111-118].

3.1.5.1 Ideal coating

A metal electrode covered by an ideal coating without any defects can be described by a pure capacity C_c. In contact with an electrolyte an ohmic resistor for the electrolyte resistance R_u must be added in series to the capacitor (Fig. 14).

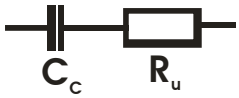

Fig. 14. Equivalent circuit for an ideal coating in contact with an electrolyte

At high frequencies the impedance of the capacitor can be neglected and the cell impedance is just dominated by the ohmic resistance of the resistor (parallel to the x-axis, phase shift 0) (Fig. 15).

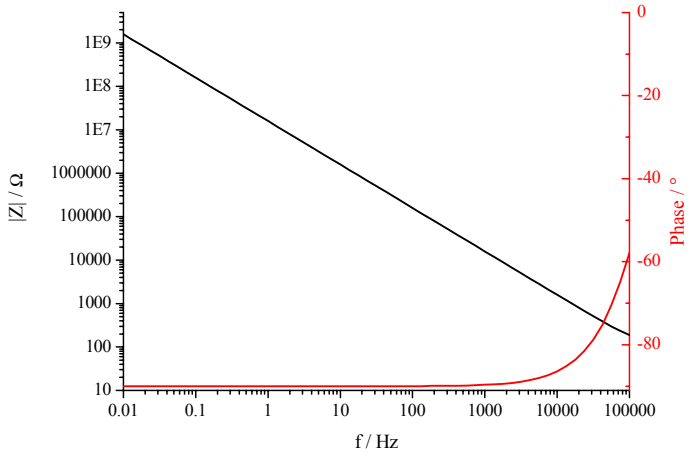

Fig. 15. Bode plot of an ideal coating with a capacity of 10 nF and an uncompensated electrolyte resistance of 100 Ohm

In the medium and low frequency the capacitor dominates and the impedance of the cell increases linearly with a slope of -1 in the bode plot. The phase shift of an ideal coating is 90°.

3.1.5.2 Metal electrode

Metal electrodes are described by a parallel circuit of an ohmic resistor that reflects the polarisation resistance R_{Ct} and a capacitor which describes the double layer capacity C_{Dl} of the electrode. Furthermore, the uncompensated electrolyte resistance R_u is added in row.

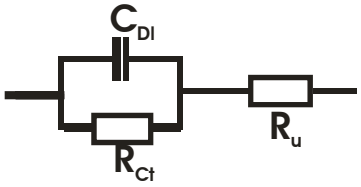

Fig. 16. Equivalent circuit of a metal electrode in contact with an electrolyte

In the bode plot the domination of the electrolyte resistance is shown as a parallel to the x-axis at high frequencies (Fig. 17).

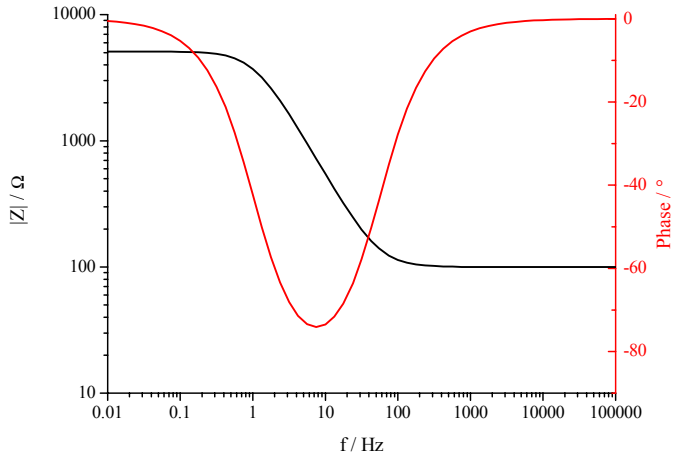

Fig. 17. Bode of a metal electrode with C_{Dl} = 30 µF, R_P = 5000 Ohm and R_u = 100 Ohm

At the medium range the double layer capacitance shows a straight line with a slope of -1 while at low frequencies a series connection of the electrolyte and the polarisation resistance prevails.

3.1.5.3 Non-ideal coating

For a defective coating the equivalent circuit for an ideal coating can no longer be taken. Defects occur by pores within the coating and allow the electrolyte to penetrate and reach the surface of the metal electrode. The penetrating electrolyte is reflected similar to the uncompensated electrolyte resistance R_u by an ohmic resistor R_C that is parallel to the coating capacitance C_c. If the electrolyte reaches the metal surface it will react like an electrode in contact with an electrolyte and can be described by a normal metal electrode circuit with double layer capacitance C_{Dl} and polarisation resistance R_{Ct}. This sub-circuit is in series with the pore resistance and parallel to the coating capacitance (Fig. 18).

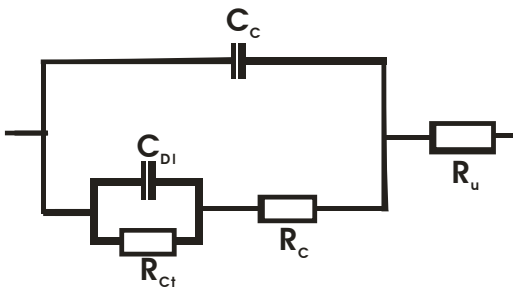

Fig. 18. Equivalent circuit of a non-ideal coating in contact with an electrolyte

The bode plot shows two time constants at high and medium frequencies displaying the coating and the double layer capacitance (Fig. 19).

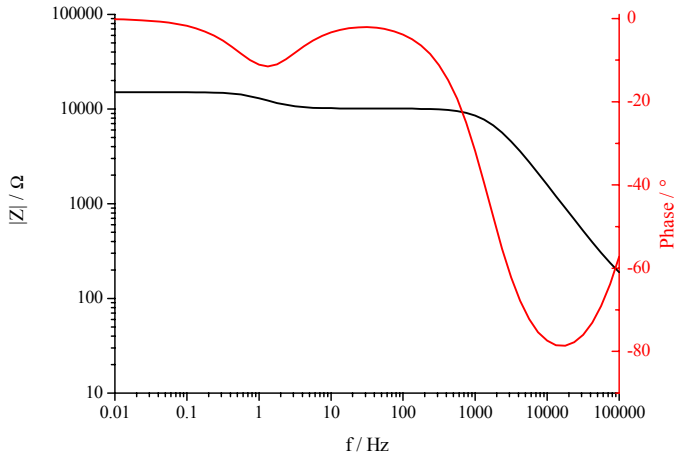

Fig. 19. Bode plot of non-ideal coating with C_C = 10 nF, R_{Pore} = 10000 Ohm, C_{Dl} = 30 µF, R_P = 5000 Ohm and R_u = 100 Ohm

The two time constants are separated by the ohmic behaviour of the pore resistance while at low frequencies a series circuit of the polarisation, the pore and the electrolyte resistance dominates.

3.2 Quartz crystal mircobalance

The quartz crystal microbalance is a sensor that allows the detection of mass changes within a few ng/cm^2. It has been used for over 40 years for measuring the deposition of materials within gas and liquid phases.

The system is based on the piezoelectric effect found by Pierre and Jacques Curie [109]. If a piezoelectric material is deformed by an external force the charge carrier will be dislocated and the material will be polarised which leads to an electrical charge at the surface. A dipole moment along the polar axis appears which is proportional to the applied force. For the QCM the inverse piezoelectric effect is used. In that case an external voltage will deform the material. For small amplitudes the extension is proportional to the applied voltage (eq. 27).

$$x = dE \qquad \textbf{(eq. 27)}$$

With x the extension, d the piezoelectric tension module and E the applied voltage

The quartz used for the QCM setup is so-called AT-cut quartz [119, 120]. The advantage of these special cuts is the small temperature dependence of the resonance frequency in the range from 0 – 50 °C. Metal electrodes applied by physical vapour deposition cover the parallel surfaces of the quartz. These electrodes are used for applying the external AC voltage and for the detection of the quartz vibration.

During the measurement the quartz is driven at its resonance frequency. At this frequency a stationary wave orthogonal to the electrode surface appears. The condition for the wave length λ is given by the thickness of the quartz d (eq. 28). For n = 1 the quartz is driven at its fundamental mode while higher numbers lead to overtones which don't have the same frequency stability.

$$\lambda = \frac{2d}{n} \qquad \textbf{(eq. 28)}$$

The first to describe the principle of the QCM was Sauerbrey in 1959 [121]. The resonance frequency of an oscillating quartz is proportional to its mass. Sauerbrey described the change in resonance frequency by the deposition of a film on the quartz surface. He pointed out that the frequency change Δf is directly proportional to the applied mass change Δm (eq. 29).

$$\Delta f = -C_f \cdot \Delta m \qquad \textbf{(eq. 29)}$$

C_f is the quartz sensitivity factor which can be calculated from the quartz density ρ_q, the number of harmonic n, the resonance frequency f and the effective piezoelectric stiffened shear modulus μ_q according to eq. 30.

$$C_f = \frac{2n \cdot f^2}{\sqrt{\rho_q \cdot \mu_q}} \qquad \textbf{(eq. 30)}$$

The mass change can be calculated after eq. 31 if eq. 30 will be inserted into eq. 29.

$$\Delta m = \frac{-\Delta f}{C_f} = \frac{(f_q - f)\sqrt{\rho_q \cdot \mu_q}}{2n \cdot f^2} \qquad \textbf{(eq. 31)}$$

Van Dyke and Butterworth showed that the oscillating quartz can be described by a simple equivalent circuit (Fig. 20) [122]. The setup is a parallel coupling of a capacitor and a vibration branch. R, C and L describe the ideal resonance of the pure quartz. Here R represents the energy lost by friction, L represents the mass load (inductance) and C the mechanical elasticity of the material (capacitance). C_s represents the capacity of the two gold electrodes and the quartz as dielectric in between.

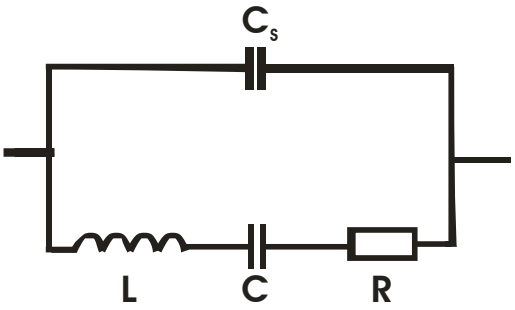

Fig. 20. Van Dyke and Butterworth equivalent circuit of an oscillating quartz crystal

The impedance Z of L and C is given by

$$Z = Z_L + Z_C = \omega L + \frac{1}{\omega C} \qquad \textbf{(eq. 32)}$$

At the resonance frequency both impedances compensate each other (eq. 33). Therefore the resonance frequency can be calculated according to eq. 34.

$$Z_L = Z_C \qquad \textbf{(eq. 33)}$$

$$f_0 = \frac{1}{2 \cdot \pi \cdot \sqrt{L \cdot C}} \qquad \textbf{(eq. 34)}$$

At frequencies below the resonance frequency the capacitive part of the circuit dominates and the phase shift of the current is positive. At higher frequencies the inductance dominates and the phase shift becomes negative.

The mission of the QCM setup is to keep the quartz at its resonance frequency while the load changes and to transfer the measured frequency to a computer for storage. This is done by the so-called Phase Lock Oscillator (PLO) which uses an internal voltage controlled oscillator to drive the crystal. The PLO also includes a phase detector continuously monitoring the phase differences between the crystal's current and voltage. The output of the phase detector is connected to an integrator. The integrator summarizes the phase error a positive phase shift causes the output to climb and a negative phase shift to fall. If no phase error occurs the integrator output holds steady. The integrator output is connected to the voltage controlled oscillator and changes the frequency of the oscillator until the phase error becomes zero at the resonance frequency.

3.3 Vibration spectroscopy for thin film analysis

In recent times the classical spectroscopic methods like Raman and IR have often been used for in-situ experiments. Especially Surface Enhanced Raman Spectroscopy (SERS) came into focus as it allows to investigate even mono layers on the SERS active substrate. Furthermore, Raman and IR spectroscopy are combined with other investigation methods to gain a more comprehensive knowledge of the system under investigation. A widely used setup is ATR FT-IR which allows an easy combination with liquid or electrochemical cells.

Different authors used ATR to study the diffusion of water through polymer film [123, 124]. Wapner et. al. used it to investigate the water transport along an adhesive / metal interface [125]. The combined Impedance and FT-IR spectroscopic analysis of the water uptake were carried out by Ohman et. al. on a metal / polymer while Vlasak et. al. used it on a semiconductor / polymer interface [106-108].

In the past SERS was used to study the adsorption of organic molecules on coin metals and the inhibition effect of these layers [126-130]. Recently Gu et. al. showed that SERS can also be extended for the use with zinc surfaces [131]. Furthermore, the combination with electrochemical methods for comprehensive in-situ investigations came into focus analysing the potential dependence of the adsorbed films [132, 133].

3.3.1 DRIFT and FTIR-ATR spectroscopy

3.3.1.1 Fundamentals

IR spectroscopy allows the detection of rotation and vibration transitions of molecules by the adsorption of light within the range of 4000 to 400 cm^{-1}. Only transitions of molecules with a permanent dipole are IR active or those where the dipole moment changes during the transition. The periodic change of a dipole moment can only happen at discrete frequencies. The adsorption intensity depends on the dipole moment change and on the orientation of the dipole to the light vector. Maximum adsorption appears with maximum dipole change and if the dipole and the light vector are parallel.

Every molecule has about 3N degrees of freedom with N the number of atoms. These degrees are separated into vibration, rotation and translation. Every molecule has 3 translation degrees one for each direction in space independent from the shape. Linear molecules have 3N-5 vibrations while non-linear molecules have 3N-6. The remaining degrees of freedom belong to the rotations of the molecule [134-136].

If light interacts with material the intensity will be weakened by the absorption, reflexion and scattering. The loss of intensity –dI is proportional to the intensity of the beam I, the absorption factor k and the length dx and the concentration c of the illuminated material [137].

$$-dI = k \cdot I \cdot c \cdot dx \qquad \textbf{(eq. 35)}$$

The vibrations of a molecule can be divided into two classes. First the valance vibration ν which leads to deformations along the bonding axis of the atoms. On the one hand this vibration can be symmetric and on the other hand asymmetric. The second class is the deformation vibration δ which can be separated in the rocking, twisting and waging vibration. Further details concerning IR spectroscopy can be found in the general literature [135, 136].

3.3.1.2 DRIFT

During classic infrared reflection absorption spectroscopy the infrared beam hits the flat sample in a certain angle of incidence and is reflected with the same angle. In the case of rough surfaces or powders the light is scattered in all directions which means that it can also be reflected a few times inside the sample before it returns to the surface. The angle of reflection at which the light leaves the sample is hardly the same as the angle of incidence. Large spherical mirrors are therefore necessary for collecting the light from the sample and focusing it to the inlet of the detector. The high number of reflections that occur before the light hits the detector leads to a loss in the signal intensity. For a standard analysis the sample needs no special preparation but has to be comparable for the quantitative analysis of the roughness or the particle size of the samples. Most often the semi-quantitative Kubelka-Munk equation is used for analysing the spectrum [138].

3.3.1.3 FTIR-ATR spectroscopy

Attenuated Total Reflection (ATR) FTIR spectroscopy is a versatile tool to investigate gaseous, liquid and solid specimen without special preparation steps. The ATR setup consists of a crystal (often ZnSe, Ge, Si or diamond) which is pressed against the sample. If the medium in contact with the crystal has a lower refractive index the incident light will be totally reflected under certain angles. Depending on the angle of incident and the size of the crystal the light can be more than one time reflected which improves the signal from the

sample. Behind the reflective interface an evanescent wave penetrates the sample and interacts with it, leading to a frequency dependent absorption as it is known from transmission spectroscopy. The penetration depth depends on the angle of incident and the wave length of the used light. In a rough estimation the penetration depth d can be seen as in the order of the incident light but can be calculated in detail with eq. 36.

$$d = \frac{\lambda}{2 \cdot \pi \cdot \sqrt{n_1^2 \sin^2 \Theta - n_2^2}} \quad \textbf{(eq. 36)}$$

With λ the wave length, n_1 the refractive index of the ATR crystal, n_2 the refractive index of the material under investigation and Θ the angle of incidence [138-140].

3.3.2 Raman spectroscopy

For the detection of an IR spectrum a change of the dipole moment during the adsorption of light is necessary. In the case of a Raman spectrum the sample is irradiated with monochromatic light and the scattered light is detected. The frequency of the light can vary in wide ranges but it mustn't be adsorbed by the sample. The demand for the Raman Effect is the polarisability of the molecule. This means the repositioning of the electron hull. The influence of the electromagnetic field E_{loc} induces a dipole moment μ to a molecule with the polarisability α (eq. 45) [134-136, 141].

$$\mu = \alpha \cdot E_{loc} \quad \textbf{(eq. 37)}$$

Light with the frequency υ_0 causes a periodic change of the dipole moment and the molecule emits light with the same frequency (Rayleigh scattering) (eq. 38).

$$\mu = \alpha \cdot E_0 \sin 2\pi\nu_0 t \quad \textbf{(eq. 38)}$$

Rotation and vibration of the molecule in the electromagnetic field cause a periodic change of the polarisability.

$$\text{For vibration: } \alpha = \alpha_{0v} + \alpha_{1v} \sin 2\pi\nu_v t \quad \textbf{(eq. 39)}$$

$$\text{For rotation: } \alpha = \alpha_{0r} + \alpha_{1r} \sin 2\pi 2\nu_r t \quad \textbf{(eq. 40)}$$

with α_0 the average and α_1 the maximum polarisability, υ_v the vibration frequency and υ_r the rotation frequency.
Combining the equation for vibration and rotation with equation 38 leads to the expression for the vibration and rotation transition.

$$\mu_i = \alpha_{ov} E_0 \sin 2\pi v_0 t + \frac{1}{2}\alpha_{1v} E_0 [\cos 2\pi (v_0 - v_v)t - \cos 2\pi (v_0 + v_v)t] \quad \textbf{(eq. 41)}$$

$$\mu_i = \alpha_{or} E_0 \sin 2\pi v_0 t + \frac{1}{2}\alpha_{1r} E_0 [\cos 2\pi (v_0 - 2v_r)t - \cos 2\pi (v_0 + 2v_r)t] \quad \textbf{(eq. 42)}$$

From equation 41 and 42 the quantum number for the vibration and rotation follows:

$$\Delta v = \pm 1$$
$$\Delta J = 0; \pm 2$$

3.3.2.1 Surface Enhanced Raman Spectroscopy (SERS)

The Raman scattering width of a molecule is normally very small so that either a high number of molecules or a high laser power is necessary to get an adequate signal. In 1974 Fleischmann et al. [142] found an increased signal during their investigations of pyridine adsorped on a rough silver sample. They attributed this effect to the increase of the active surface by the roughening. Later on other researchers realised that the significant signal increase cannot only result from the larger sample surface.
The so-called Surface Enhanced Raman Spectroscopy (SERS) is based on the effect that the signal of molecules in contact or close to SERS active material undergoes an enhancement by up to 8 orders of magnitude. SERS active substrates are certain metal substrates (e.g. gold and silver) which show a nano rough or island structure with a size between 5 and 100 nm. Mainly two models which are also complementary to each other are used to explain this effect, the electromagnetic enhancement and the chemical enhancement [143-145].
During the electromagnetic enhancement the molecule comes close to the hemispheric nano structure of the metallic substrate. The molecule thereby influences the electric field of incident light and the induced dipole field of the sphere. Both fields add each other and lead to a magnification of the signal by up to 8 orders of magnitude.

For the chemical enhancement the molecule needs to have direct contact with the metal sphere. The incident light can create an excited electron and a corresponding hole. If the Fermi level is in between the HOMO and the LUMO of the adsorbed molecule the electron can transfer into the LUMO of the molecule, resulting in an exited charge transfer state. The electron-hole recombination leads to the emission of light of a certain frequency. This effect should lead to a lower magnification of the signal than the electromagnetic enhancement but this has not yet been clarified.

3.4 Scanning electron microscopy

The scanning electron microscope (SEM) allows a detailed surface analysis of condensed materials. During the analysis a focused electron beam that is formed by the interaction with the surface secondary and back-scattered electrons scan the specimen. These electrons are detected and used for imaging. Two main classes of SEMs exist which are separated by the electron formation. The conventional SEM uses a hot cathode for the electron generation while the latest Field Emission devices use either cold or Schottky Field Emission [146, 147]. After the generation the electrons are accelerated with up to 50 kV through the vacuum column of the SEM where they are focused by electro-magnetic lenses.
Depending on the acceleration voltage ΔE the theoretical resolution can be calculated with the de-Broglie wavelength of the electron λ (eq. 51).

$$\lambda = \frac{h}{m \cdot v} = \frac{h}{\sqrt{2m_e \cdot e \cdot \Delta E}} \qquad \textbf{(eq. 51)}$$

with λ the de-Broglie wavelength, h the Planck constant, m the mass, v the speed, m_e the electron mass, e the electron charge and ΔE the acceleration voltage.

The theoretical resolution for electrons accelerated with 1 kV is 38 pm. Due to the fact that the energy source is not infinitely small and by lens errors the real resolution is about 10 nm.
When the electrons hit the sample surface they can interact elastically or inelastically with the material. The interaction area and depth depends on the acceleration voltage and the atomic number of the sample material. From the sample surface emitted electrons are separated by their energy into secondary electrons (below 50 eV) and back-scattered electrons (50 eV up to the acceleration voltage). Secondary electrons are formed by the inelastic interaction (ionisation) of surface atoms. Further reactions of the electron beam with the sample are the formation of Auger-electrons and X-Rays, both are not used for the standard SEM imaging. Either a chamber or an in-lens detector can perform the detection of secondary electrons. Chamber detectors mainly consist of an Everhart-Thornley detector that uses a grid with an applied voltage between -200 V to +200 V to collect the electrons. The electrons hit the scintillation counter and generate photons, which are amplified by a photomultiplier. The signal is converted into an electrical signal and used by the image processor. High electron yields thereby lead to lighter and lower electron yields and to darker pixels in the image.

In-lens detectors also collect the electrons by an applied voltage but the detection of the electrons happens by a semi-conductor. When an electron hits the detector it generates electron-hole pairs that lead to an electric signal. In-lens detectors allow a much smaller working distance and collect the electrons at the point of impact. These advantages lead to higher resolutions in contrast to the chamber detectors.

3.5 Focused Ion Beam (FIB)

The Focused Ion Beam (FIB) is very similar to the scanning electron microscope mentioned above, except that the beam scanning the sample surface consists of ions rather than of electrons. The FIB can be either used to image the sample surface or to process the surface by sputtering it with ions. Secondary ions are generated during the scanning by the interaction of the ions with the sample atoms and can be detected in a similar way as in the SEM.

In most commercial FIBs Gallium is used as ion source for the beam. The low melting point of Ga allows the easy setup of liquid metal ion sources based on a tungsten needle from where the Ga is extracted by field emission (10^{10} V/m) with a current of up to 2 µA. Similar to the SEM the columns in which the ion beam is accelerated by 5 – 30 kV consist of lenses which focus the ion beam. Due to the fact that the focusing strength of electromagnetic lenses is directly related to the charge / mass ratio electrostatic devices are used to reduce the weight.

During the investigation the ion beam scans over the sample and interacts by different processes like ion backscattering, electron emission, sputtering, sample damaging and heating [148, 149].

As already mentioned the formation of secondary electrons can be used to image the surface but thereby the sample will be contaminated by Ga-ions. This effect can be used to investigate non-conductive samples as they are plated by a conductive Ga layer.

Highly accelerated ions can be used to sputter the surface and thereby create structures in the micro and nano meter scale. Sputtering is often used to prepare lamellae for TEM applications. During the milling the sample is heated due to the current flow by the ion beam. The maximum power reached by commercial systems is in the range of 1 mW. Depending on the thermal conductivity of the material negligible or significant temperature changes appear. The temperature increase can be calculated accordingly eq. 52.

$$\Delta T = \frac{P}{(\pi \cdot r \cdot \kappa)} \qquad \textbf{(eq. 52)}$$

with ΔT the temperature change, P the power of the ion beam, r the radius of the ion beam and κ the thermal conductivity of the sample.

In commercial FIB P/a values of 1 W/m up to 1000 W/m can be archived, causing a ΔT for iron (κ = 80 W/mK) to be about 4°C while for polymers (κ = 0.2 W/mK) ΔT can reach up to 1600°C.

4 Experimental

4.1 Materials, Electrolytes and Parameters

4.1.1 Substrate and sample preparation

4.1.1.1 Preparation of corrosion protection primer samples

The material used for coating applications consists of ductile electro-galvanised steel recommended for high forming degrees (DC 06 ZE 75/75, thickness 0.8mm), coated with a 7.5 µm zinc layer on both sides. Before coating with organic layers, the steel sheets (500 x 200 mm) were cleaned using an alkali brush cleaning line (Wesero, Germany) and rinsed with deionised water.

Afterwards all steel samples were first treated with a chromate-free conversion layer (Granodine 1456, Henkel, Germany). Additionally, the metal substrates were coated with a 3.5 µm thick primer containing microscopic zinc particles and corrosion inhibition pigments (Granocoat ZE, Henkel, Germany) and applied using a lab roller coater (Mathis, Switzerland). The coating was cured in a continuous furnace at the peak metal temperature of 260 °C.

In-situ uniaxial forming was applied to specially shaped, miniature stretching samples. The samples were cut from the coated steel sheets using a pulsed 300 W YAG laser (Lasag Vega, Switzerland).

For the open circuit measurements during the phosphating step, ex-situ stretched samples (see below) were cut to 50 x 30 mm and sealed in the non-coated areas with a corrosion protection lacquer. The laquer was dried at room temperature for 24 h.

4.1.1.2 Preparation of polyelectrolyte coated samples

Steel substrate used for the preparation of polyelectrolyte (PET complex synthesised by O. Seewald, University of Paderborn) coated samples are similar to those used for the preparation of corrosion protection primer samples (DC 06 ZE 75/75, thickness 0.8 mm). The laser cut miniature stretching samples and the manually cut samples (20 x 40 mm) were first cleaned by a three step solvent cleaning and afterwards by an alkaline cleaning bath.

The solvent cleaning consists of ultra sonic cleaning in “pro analysis” tetrahydrofuran, isopropanol and ethanol (Merck, Germany). The alkaline cleaning was undertaken in a mild

alkaline bath at 55 °C (Ridoline 1553, Henkel, Germany), afterwards the samples were rinsed with ultra-purified water (Elga Purelab, Germany) and dried in a nitrogen stream.
The coating procedure took place with a home-built dip coater at a dipping speed of 2 mm / s. The PET complex was diluted 1:3 by weight with butylglycol. The curing of the coating was carried out at room temperature (24h and 30d), 130 °C and 230 °C (both 2h) under standard and nitrogen atmosphere.

4.1.2 Forming of samples

4.1.2.1 Forming for Ex-Situ Analysis

Biaxially formed, so-called Marciniak samples were prepared from 225 x 225 mm coated steel sheets using a hollow round shaped stamp with a diameter of 100 mm on an Erichsen deep drawing machine (Erichsen, Germany). The blank holder was adjusted to maximum force and forming degrees of φ_v = 0.10, 0.15 and 0.25 were prepared.
Plane strain formed samples were prepared from round shaped steel sheets (diameter 200 mm) with special laser cut-outs at the edges (Fig. 22). The same setup as for Marciniak samples was used and forming degrees of φ_v = 0.10, 0.15 and 0.25 were prepared.
Uniaxial forming with elongations between 5 and 20 % was performed by means of a Z 100 (Zwick, Germany) tensile testing device using 500 x 80 mm organically coated steel strips. The positions of the odometer were marked on the strips and the samples were cut from between the marks to guarantee reproducible forming.
These samples were used for FE-SEM investigations, focused ion beam cross section measurements and open circuit potential measurements during phosphating.

4.1.2.2 GOM® Grid Evaluation

Forming degree evaluation of the stretched samples was performed using an optical grid evaluation system (GOM®, Gesellschaft für Optische Messtechnik, Germany). An electrochemically etched grid with equidistant spots (1 mm distance) was applied to the sample surface and optically analysed with a digital camera after forming. Following the grid detection, all three forming degrees can be calculated using the PC-based software when comparing the original with the formed grid.

4.1.2.3 Finite Element Simulation

The different elongations of the miniature stretching sample were also analysed with regard to homogeneity and forming degree by means of finite element simulation (INDEED®, Gesellschaft für numerische Simulation, Germany). For easier analysis, the three forming degrees (φ_1, φ_2, φ_3) were combined to the equivalent strain.

4.1.3 Preparation of biaxial formed samples for corrosion testing

For the phosphating, ED-paint application and finally corrosion testing of biaxially formed samples a special mounting was constructed (Fig. 21). First the samples were formed like a standard Marciniak sample with a defined forming degree (φ_v = 0.25). Afterwards the round shaped, flat middle part was cut out with a diameter of 75 mm by a 300 W Nd:YAG laser (Lasag Vega, Switzerland).

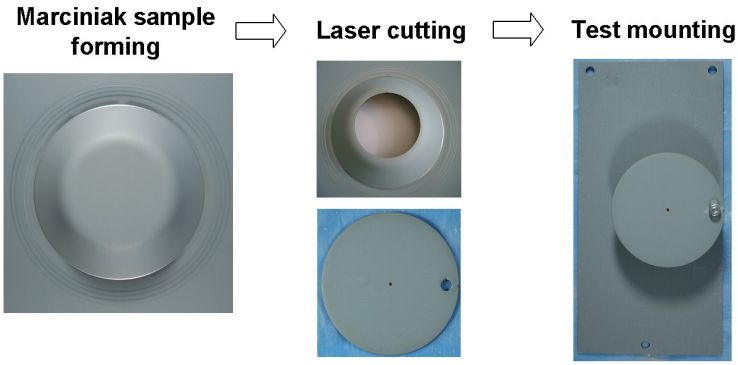

Fig. 21. Sample mounting for corrosion testing of formed corrosion protection primers

The circular blank was perforated at one edge and mounted to a carrier sheet (100 x 200 mm). These carrier sheets fit into the mountings of the phosphating and ED-paint station. After the phosphating and ED-paint application the samples were placed in racks inside the corrosion chamber.

4.1.4 Preparation of plane strain formed samples for scanning in-situ Raman / EIS investigation

For the scanning in-situ Raman / EIS investigation plane strain formed samples were prepared. Before the forming operation round shaped specimen with defined cut-outs were prepared from the coated samples by laser cutting (Fig. 22).

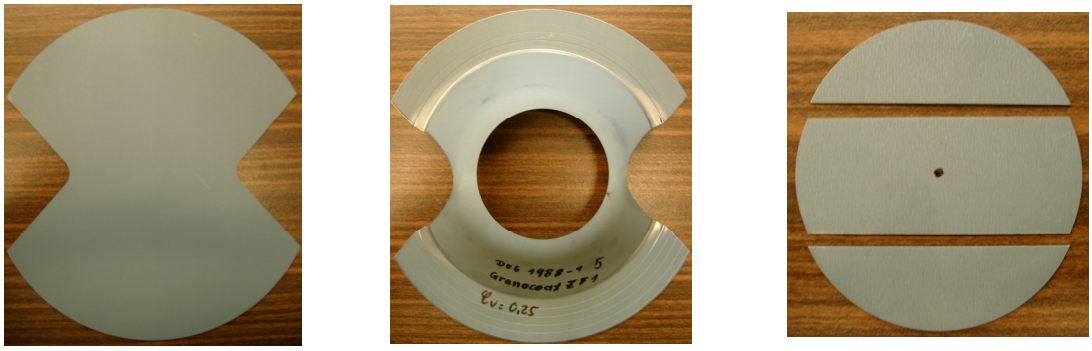

Fig. 22. Preparation of plane strain formed samples for in-situ Raman / EIS analysis

Afterwards the samples were mounted in an Erichsen device and formed similar to the Marciniak samples. Again the round shaped middle part of the sample was cut out with a laser and used for further investigations. The circular blanks were cut into three pieces with the middle part orthogonal to the homogeneously formed area of the sample (see forming of plane strain samples for details).

4.1.5 Phosphating and ED-paint application of formed corrosion protection primer coated samples

The phosphating of the stretched SEM samples was performed in a car phosphating simulator based on the real automotive process with cleaning, activation and phosphating steps at 55°C (Chemetall, Germany). If applied the ED-paint application followed the phosphating step. The paint was applied in a laboratory scale by cathodic deposition (Cathoguard 310, BASF, Germany).

The in-situ open circuit potential measurement during phosphating was conducted after activation in a standard phosphating bath at 55 °C (Henkel Surface Technologies, Germany).

4.1.6 FE-REM investigations and FIB preparation

FE-SEM pictures of surfaces and cross sections were taken for different forming degrees using a LEO-Zeiss 1530 Gemini (Germany). The acceleration voltage was set at 0.5 kV and the in-lens detector was used to achieve a high surface resolution and to monitor the formation of cracks in the organic coating. Focused ion beam (FIB) cross sectioning was prepared on a LEO-Zeiss 1540 XB. The cut was milled by a gallium ion beam with a current of 30 nA. Finally surface images of ex-situ stretched, phosphatised samples and of

polyelectrolyte samples were taken by a LEO-Zeiss 1550 VP with a secondary electron detector using different acceleration voltages.

4.1.7 Raman and IR spectroscopy

Raman spectroscopy was carried out using a Raman microscope system (Dilor, LabRAM, ISA Instruments, France). It consists of a red HeNe laser (632.8 nm) with 20 mW power and a green Ar^+ laser (514.5 nm) with adjustable output power. Four objectives with 10x and 100x magnification were selectable. During the measurements the laser power was set at 2 mW for the adsorption measurements of MBT (Ar^+ laser) and 20 mW (HeNe laser) for the corrosion product identification of CPP. The pinhole was set to 1000 µm and the size of the slit to 100 µm. The integration time was set to 10 seconds and 10 spectra were taken to optimize the signal to noise ratio.

For the IR spectroscopy a Fourier transformation infrared spectrometer (Biorad, USA) was used with a microscope ATR unit. A liquid nitrogen cooled MCT detector was used and the spectra were acquired with 512 scans at a resolution of 4 cm^{-1}.

4.1.8 Glow Discharge Optical Emission Spectroscopy (GDOES)

The Glow Discharge Optical Emission Spectroscopy (GDOES) was performed with a LECO GD-OES 750 (LECO, USA) system. The system was driven with a current of 20 mA at 700 V DC voltage and a sampling rate of 20 Hz.

4.1.9 Laser Optical Emission Spectroscopy (Laser-OES)

Laser Optical Emission Spectroscopy (Laser-OES) was conducted with a home-built scanning spectrometer which allows scanning the sample surface. The sample size was chosen to be 5 x 5 mm and scanned with 500 x 500 spots. For the pretreatment distribution only titanium was taken as tracer element.

4.1.10 Electrochemistry and electrolytes

During the in-situ impedance analysis the whole setup was placed in a Faraday cage and connected to a highly sensitive potentiostat (Gamry Femtostat FAS2, USA) with an implemented frequency analyser.
The in-situ Raman / EIS measurements were also done with a Gamry Femtostat.
All measurements were performed at room temperature between 100 kHz – 0.1 Hz (or 1 Hz) using 0.05 M NaCl or borate buffer as electrolyte. 10 points per decade were recorded at open circuit potential.
Pro analysis grade chemicals (Merck, Germany) and ultra-purified water (Elga Purelab, Germany) were used for the preparation of the borate buffer electrolyte (pH 8.3) and the 0.05 M NaCl solution.
For the open circuit measurements during the phosphating step the ex-situ stretched samples were measured versus a 3 molar Ag/AgCl reference electrode (Metrohm, Switzerland).

4.1.11 Corrosion Testing

Two accelerated corrosion tests were used to investigate the protective properties and the corrosive behaviour of the formed corrosion protection primers. The first test in the common salt spray test according to DIN 50021-SS due to the continuous load with corrosive medium galvanised samples undergoes a fast attack (metal removal of ≈ 1µm Zn / 10h). The following conditions are given during the testing:

- Salt concentration: 50 ± 5 g/l NaCl
- Amount of salt solution: 1.5 ± 0.5 ml/h
- pH-value of the salt solution: 6.6 – 7.2
- Temperature: 35 ± 2 °C
- Sample orientation: 60 – 70 °

The salt spray test shows a strong corrosive attack which is uncommon for the corrosive load appearing during the use of an automobile. Cyclic corrosion tests show a much better correlation between the field results and the laboratory testing. The standard test for cyclic corrosion testing is the VDA 621-415. It is a combination of salt spray testing, wet and dry periods. The testing details are given below and in Tab. 3:

- 24 h salt spray testing according to DIN 50021-SS
- 8 h at 40 ± 3 °C with 100 % relative humidity, 16 h at 18 – 28 °C with 55 – 65 % relative humidity according to DIN 50017
- 24 h at 18 – 28 °C with 55 – 65 % relative humidity according to DIN 50014

Tab. 3. One cycle (one week) of the accelerated corrosion testing according to VDA 621-415

Monday	**Tuesday**	**Wednesday**	**Thursday**	**Friday**	**Saturday**	**Sunday**
Salt spray testing DIN 50021	Climate change testing DIN 50017				Constant climate testing DIN 50014	

4.2 In-situ Electrochemical Impedance Spectroscopy (EIS) and Forming Setup

The major disadvantage of the ex-situ EIS of formed materials is the time-consuming sample preparation and experiment procedure. Each sample has to be prepared and measured individually for each forming degree.

A much faster approach is measuring the impedance at the same time as the forming of the sample. Capillary cells provide a useful electrochemical technique for reducing the sample preparation time and achieve a high local resolution [150-152]. Pilaski et al. show that they are also suitable for EIS experiments on metal substrates [153].

During the process, a glass capillary is pressed to the sample surface. The inner area forms the working electrode. The sample needs no special preparation or handling and due to this fact, the capillary diameter can range from millimetres to micrometres. The sample size can be much smaller and the required quantity of material is reduced. One limiting factor for the reduction of the capillary tip is the input impedance and resolution of the potentiostat (Gamry Femtostat FAS2, USA), which works in the femto ampere range and therefore restricts the total maximum detectable impedance of the system to about 10^{12} Ω (with 10 mV amplitude) [154]. The capacity of the wires used becomes more and more important as the working electrode area is reduced, since it reaches the same range as the monitored signal and the two values can no longer be distinguished. The capacity of 50 cm long connection wires can be calculated to be nearly 50 pF. This means that the lowest detectable capacity must be larger than 50 pF in order to remain separate.

A few disadvantages arise as a result of combining capillary cells with standard stretching devices. The sample holder is mainly erected vertically, which leads to problems when positioning the capillary. Moreover, the advantage of the smaller sample size is invalidated since the sample holder is too large to handle these small samples. Custom-built miniature stretching devices avoid these problems and allow horizontal sample mounting. Furthermore, the setup size can be reduced to take advantage of the sample size reduction achieved by the use of a capillary cell. Such devices need specially shaped, smaller samples to avoid an overload and to enable homogeneous material flow over a wide forming range. A special point of interest is the formed area in the middle of the sample where the measurement data for the electrochemical experiment is obtained. Here it is crucial to have a uniform strain distribution in order to achieve high reproducibility for the experiments.

For the in-situ measurment of EIS during tensile testing, a new setup was designed, which combines the advantages of localised electrochemistry with those of miniature stretching samples. The setup consists of three main parts:

- Custom-built, miniature tensile testing device with home-made, isolated sample holder
- Home-made three-electrode electrochemical capillary cell
- Home-made mounting for capillary cell and stretching device

The miniature tensile testing device is a custom-built setup (Kammrath & Weiß, Germany) which allows the uniaxial forming of samples with a load of up to 5 kN. The sample holder is specially designed (home-made) in order to allow the electrical isolation of the sample from the device (Fig. 23).

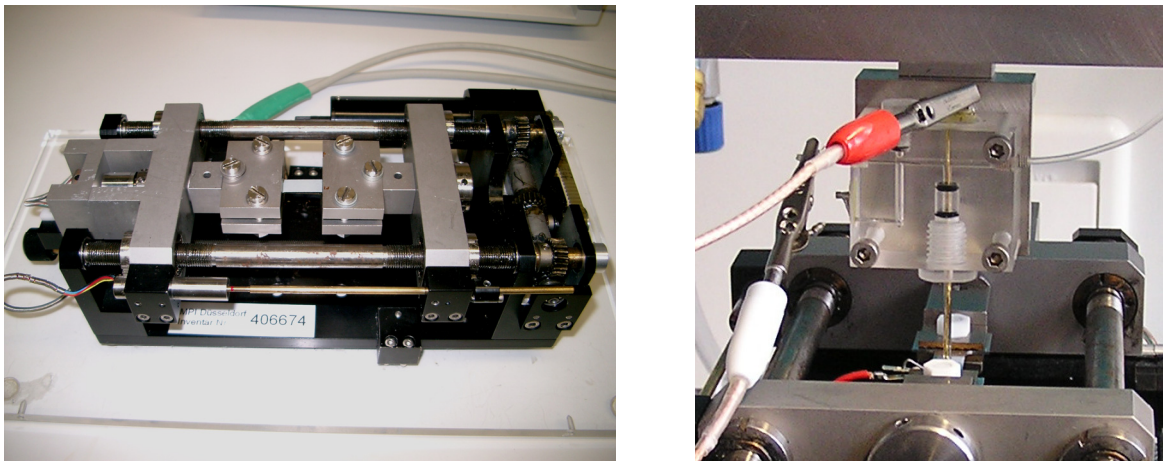

Fig. 23. Miniature stretching device with isolated sample holder and mounted sample; (right) detailed view of a capillary cell positioned on a sample during in-situ EIS analysis.

The external controller displays the elongation and stretching force and can send the data to a personal computer for storage and further processing. A new stretching sample was designed which features both a small size and a homogeneous forming characteristic over a large elongation range (Fig. 24).

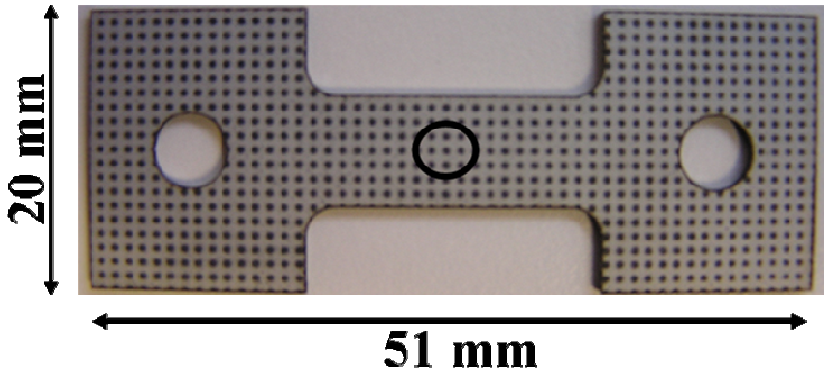

Fig. 24. Specially designed miniature stretching sample

For highly reproducible spectra during EIS analysis, it is important to measure in an area with a homogeneous forming degree. This requires a special sample geometry and a high local resolution. The high local resolution was achieved by means of a capillary-based cell where the working electrode is formed by the inner area of the capillary. The cell setup used is related to one described by Lohrengel et al. [155]. It consists of a Plexiglas® carrier including a reference electrode, gold counter electrode and a glass capillary which forms the junction between the counter/reference and the working electrode (sample surface). The area of the working electrode is formed by the inner area of the capillary and was calculated to be $8 \cdot 10^{-3}$ cm^2. To avoid leaking and evaporation of the electrolyte and to form a reproducible working electrode area, the capillary tip is equipped with a flexible silicon gasket. The gasket is pressed against the sample surface during the measurement process. A force sensor measures the level of contact and allows the force between the capillary and the sample to be controlled. Two different kinds of reference electrodes can be used depending on the electrolyte: mercury electrodes such as mercury/mercury sulphate electrodes or environmentally friendly silver/silver chloride or silver electrodes.

The mounting consists of a stainless steel tripod and z-axis stage (Owis-Staufen, Germany) with 3 µm resolution and a maximum lift of 30 mm. The stretching device is placed on top of the stage. The electrochemical cell is fixed to the mounting and the stretching unit, and with the sample in place, is pressed against the capillary tip during the measurement process. Fig. 23 shows the complete setup with tripod, capillary cell and stretching device.

4.3 In-situ Quartz Crystal Microbalance / Raman Setup

The adsorption kinetics of monolayers is of great interest for the effectiveness of inhibitors and conversion layers and for the crystal growth in general. A perfect tool that has enough sensitivity for detecting mass changes in the ng/cm² range is the Quartz Crystal Microbalance (QCM). The QCM consists of quartz oscillating at its resonance frequency, additional load to the quartz leads to a frequency shift that is proportional to mass changes (eq. 31). The QCM can be used either in a gas or in a liquid environment where it can be combined with electrochemical tools for detecting the mass change under potential control.

Raman Spectroscopy on the other hand gives information about the structure of molecules and can be used to identify them. In the case of monolayers the Raman signal is weak and cannot be detected by common systems. Fleischmann et. al. [142] show that certain metal nano particles can lead to an amplification of the signal. The so-called Surface Enhanced Raman Spectroscopy (SERS) allows the detection even of monolayers attached to the nano porous material. The combination of both tools allows the in-situ investigation of the adsorption process of molecules.

For the combined in-situ measurement a new QCM flow cell was designed which allows the simultaneous Raman investigation of the quartz crystal surface. The used QCM (Maxtek RQCM, USA) is specially designed to work with high mass loads and in a liquid environment. The setup consists of an oscillation circuit, a Teflon quartz holder and a polished gold coated 5 MHz quartz. The holder of the quartz crystal was extended by the newly designed and home-built flow cell.

The flow cell consists of a circular Teflon® body which is pressed against the quartz crystal by an o-ring. The setup forms a volume of about 100 µl between the quartz and the Teflon® body. For a constant electrolyte flow an in-let and out-let are adapted and connected by Teflon® tubes to a computer controlled pulsation free syringe pump (MDSP3f, Micro Mechatronic GmbH, Germany). The electrolyte can either flow from a beaker through the pump and the cell back to the beaker, or from a reservoir beaker through the setup into a waste compartment. The middle of the cell consists of an 11 x 11 mm quartz glass window to couple the laser beam from the Raman microscope (Dilor, LabRAM, ISA Instruments. SA, INC, France). The laser is focused on the surface of the quartz crystal and the emitted radiation of the molecules is scattered back to the spectrometer. To allow the detection of adsorbed monolayers the SERS effect is used. Therefore the gold electrode of the quartz was

covered by a nano porous SiO_2 and a 100 nm thick silver or gold layer [156]. Fig. 25 shows a schematic sketch of the measurement setup.

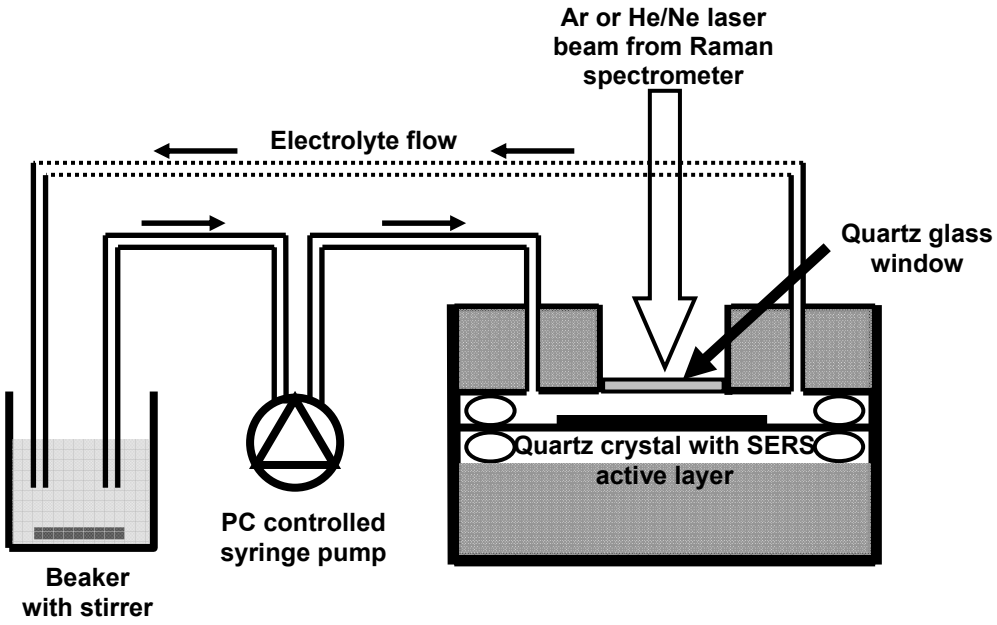

Fig. 25. Schematic sketch of the in-situ Raman / QCM flow through concept. The electrolyte cycles through the system and the inhibitor under investigation can be added after the system comes to a steady state

The cell can be used in two configurations on the one hand just for in-situ Raman / QCM measurements and on the other hand for in-situ Raman / QCM measurements under potential control. For investigations under potential control the cell body can be further equipped with a counter and a reference electrode (Fig. 26). As reference electrode a micro silver / silver chloride electrode similar to the one described by Hassel et. al. [157] can be connected.

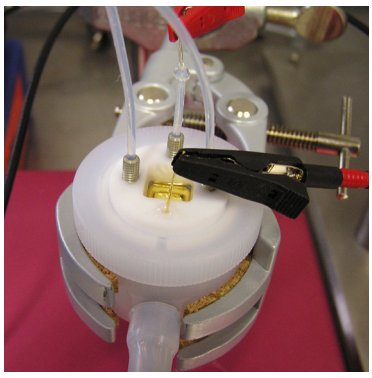

Fig. 26. Photo of the newly developed in-situ Raman / QCM flow cell, showing the electrolyte inlet / outlet and the connections for the counter and reference electrode

The counter electrode consists of a gold wire which is mounted around the Raman window in the middle of the cell. The working electrode will be in this case formed by the gold electrode of the quartz crystal.

4.4 Scanning in-situ Raman / Electrochemical Impedance spectroscopy Setup

The investigation of localised corrosion phenomena appearing on organically and / or metallically covered substrates is of great interest for understanding the corrosion mechanism in small defects and on impurities. In this case investigation methods confined to small areas allow gaining detailed information about the processes. The demand of high local resolution is fullfilled by both Raman spectroscopy and electrochemical capillary cells. While Raman spectroscopy delivers detailed information about the corrosion products formed, electrochemistry and in particular impedance spectroscopy can give detailed information about the protective properties of organic and metallic coatings.

The combination of both techniques delivers a detailed view of the processes that occur during corrosion. Therefore an electrochemical capillary cell was designed which can be mounted into a Raman microscope (Dilor, LabRAM, ISA Instruments, France) and allows the spectroscopic and electrochemical investigation in the same area of the sample surface. The basic cell used is related to the capillary cell described in chapter 4.2. It consists of a Plexiglas® carrier including a reference electrode, gold counter electrode and a glass capillary which forms the junction between the counter/reference and the working electrode (sample surface). The area of the working electrode is formed by the inner area of the capillary and was calculated to be $8 \cdot 10^{-3}$ cm^2. The sample is placed on a special stage equipped with a force sensor which measures the level of contact between the capillary and the sample. The reference electrode can either consist of a mercury electrode like e.g. a mercury/mercury sulphate electrode or silver/silver chloride electrode. The complete capillary cell is mounted as an exchange for one of the objectives in the Raman microscope and is connected to a potentiostat (Gamry Femtostat FAS2, USA) (Fig. 27).

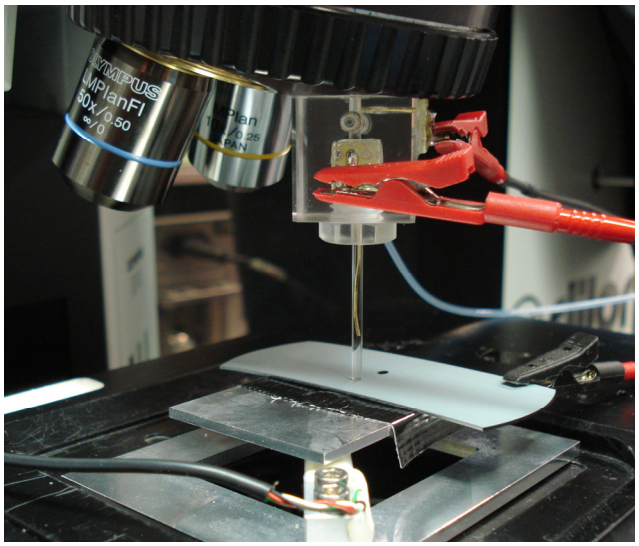

Fig. 27. Photo of the in-situ Raman / impedance setup showing the capillary cell mounted to the Raman spectrometer and in touch with a formed sample

During the analysis the same spot on a sample can be investigated by either Raman spectroscopy or electrochemistry just by turning the objective holder of the microscope.

5 Results

5.1 Characterisation of corrosion protection primers (CPP)

Corrosion protection primers (CPP) are applied on all grades of electrogalvanised steel which are covered by 5 or 7.5 µm zinc. The zinc layer leads to a homogeneous, micro-structured surface without the typical grain boundaries known from hot dip galvanised steel. Fig. 28 shows the undirected terrace structure of the zinc layer on high ductile steel (DC 06). The layered structure leads to a good paint adhesion and thereby in a macroscopic view to an excellent formability of the applied CPP.

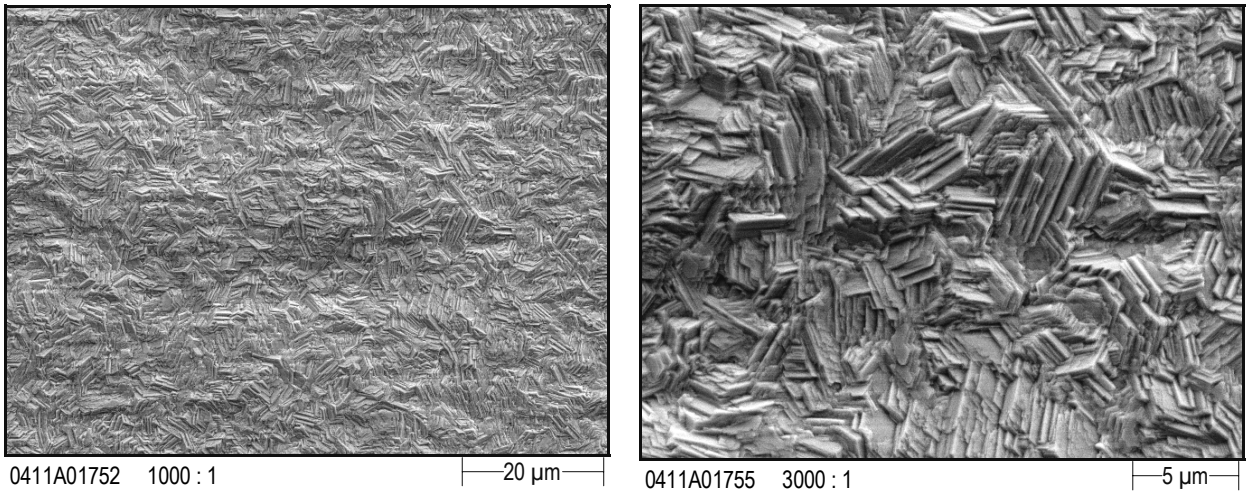

Fig. 28. FE-SEM image of an unstrained DC 06 ZE 75/75 (electro-galvanised steel) used for the coil coating application showing the parallel layers of the tilted zinc crystals

Before CPP application the sample was coated with a chromium free pretreatment containing silane, Zirconium and Titanium which increases the paint adhesion and leads to a reduction of the under paint corrosion by a passivating layer. The pretreatment (8 mg/m^2 Titanium) forms a thin layer of some nano meter on top of the zinc structure which is visible by the roughening of the terraces (Fig. 29). Furthermore, the zinc layer edges are rounded by etching attack of the pretreatment.

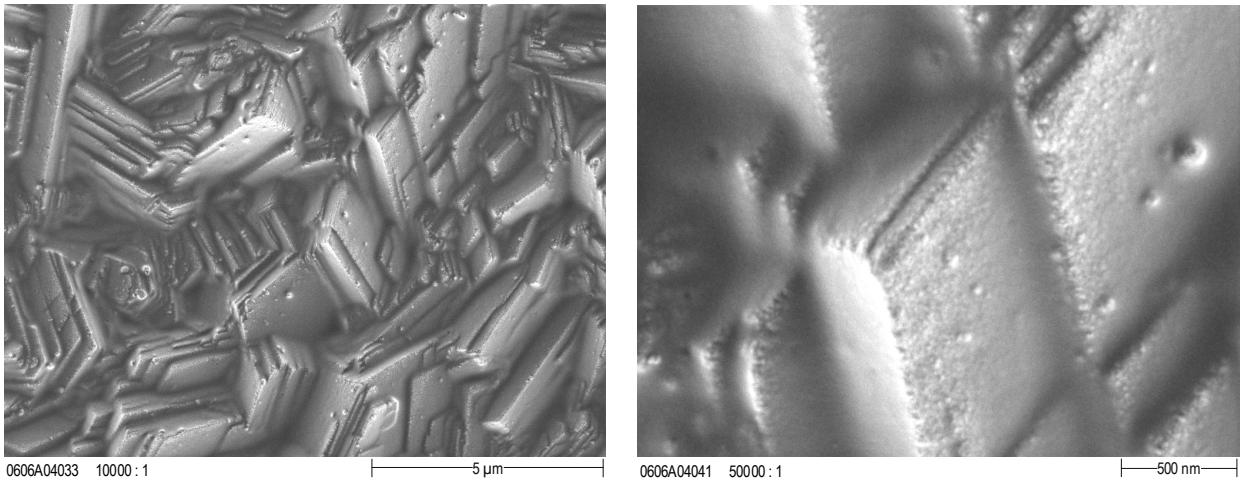

Fig. 29. FE-SEM image of an unstrained DC 06 ZE 75/75 (electro-galvanised steel) used for the coil coating application covered with a chromium free pretreatment of few nm thickness. The detailed view (right) shows only a very thin roughening by the layer

For an optimal adhesion of the corrosion protection primer to the steel substrate the uniform application of the pretreatment with an average amount of 6 – 10 mg/m² Titanium as trace element is necessary. The distribution profile acquired by Laser-OES of a 5 x 5 mm sample shows a homogeneous surface coverage of the pretreatment applied by the roll coater. The average Titanium amount taken as indicator for the pretreatment is about 8 mg/m².

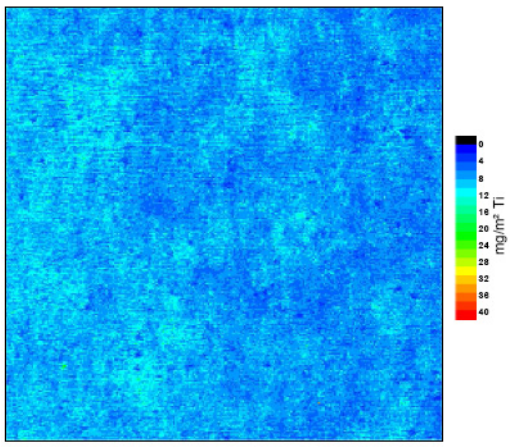

Fig. 30. Laser-OES measurement of the lab coil coated pretreatment distribution on a 5 x 5 mm electro galvanised steel sample using titanium as tracer element. The measurement shows a homogeneous coverage of the complete sample

The top view SEM picture of an unstrained CCP sample with a layer thickness of 3.5 µm is shown in Fig. 31. The coating shows a rough surface caused by the mostly spherical zinc particles with a size of 2 – 7 µm. These particles are homogenously distributed in the organic

matrix. Furthermore, angularly shaped silicate pigments are visible which are also distributed within the organic binder system.

The detailed view indicates that the particles are mainly embedded within the resin matrix, only a small hemispheric part sticks out of the coating and is covered by a porous oxide film.

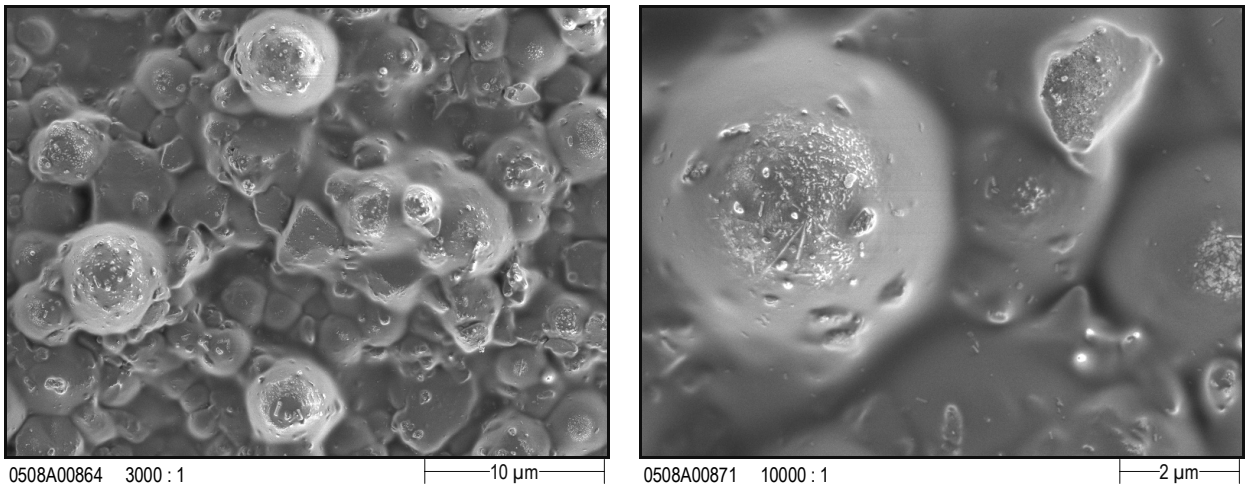

Fig. 31. FE-SEM image overview (left) and detail view (right) of an unstrained zinc pigmented coil coating primer, showing round shaped zinc particles mainly embedded in the organic binder matrix

The cross section shows the steel substrate covered with the electro galvanised zinc layer (7 µm thickness) and the CPP layer on top (Fig. 32). The boundary between the organic binder of the CPP and the resin for the cross section preparation is clearly visible.

The cross section of the CPP displays the roundly shaped zinc particles and the angularly shaped corrosion inhibition pigments already known from the top view. Most of the zinc particles are completely covered and float within the organic matrix. Only very few have contact with the underlying zinc coating, but none of them leads to a direct conducting path from the base material to the coating surface.

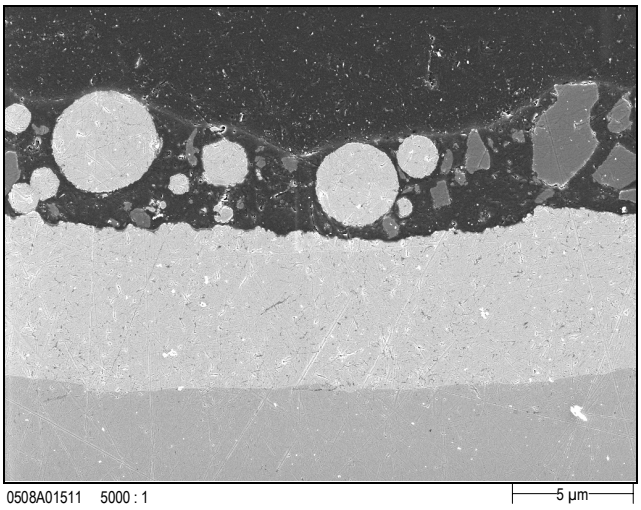

Fig. 32. FE-SEM cross section of an unstrained zinc pigmented coil coating primer, showing roundly shaped zinc particles and angularly shaped corrosion inhibition particles

The cross section prepared by the Focused Ion Beam (FIB) has the advantage of sample preparation without the smearing effect of the resin known from the preparation of a metallographic cross section. Here, the occurrence of defects within the coating can be studied. Unfortunately the gallium ion beam can locally lead to a high thermal influence within the coating which might result in a local shrinking of the polymer film. External force during the handling of the coated steel (coiling, cutting etc.) can cause a stretching of the polymer film and thus an energetically non-optimised molecule orientation. At higher temperatures the molecule chains can reorient due to the higher mobility and might form a closer, energy optimised package. The calculated local heating of the sample according to eq. 52 (chapter 3.5) can increase by up to 1600 K for a pure polymer coating. Due to the good thermal conductivity of the steel substrate (maximum heating of steel $\Delta T = 4$ K, see chapter 3.5) the heating of the applied polymer film should be lower than 1600 K but cannot be clearly calculated.

The FIB cross section shows the steel matrix covered by the electro galvanised zinc layer and the CPP on top (Fig. 33). The roundly shaped zinc particles are distributed within the organic binder. Small defects are visible in the higher magnification at the pigment / binder interface which can be caused by the heating of the ion beam. At the substrate / binder interface no defects are visible which proves the good paint adhesion.

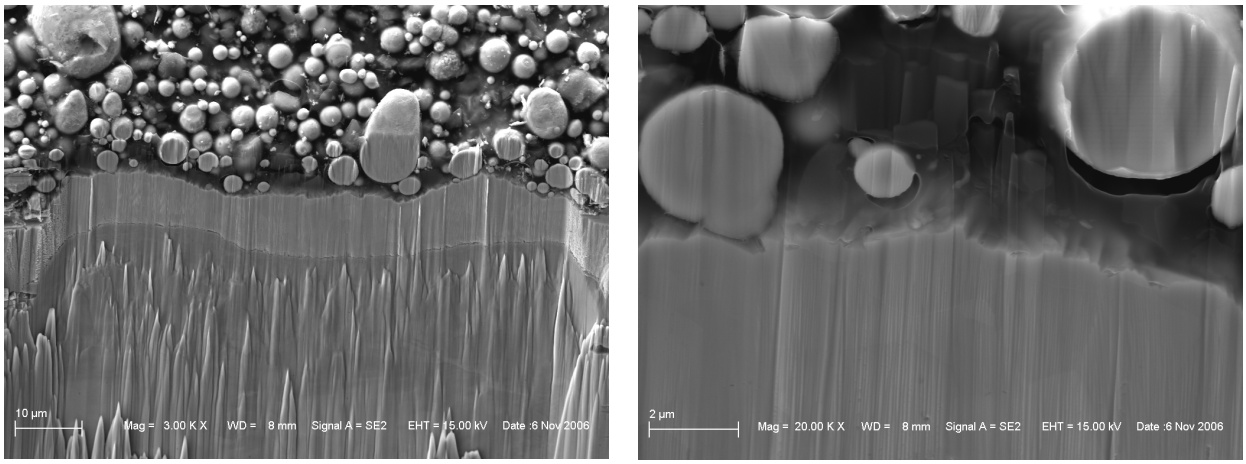

Fig. 33. Focused ion beam cross section of an unstrained zinc pigmented coil coating primer, indicating a good adhesion of the coating to the substrate and just local detachment from the zinc particles

The GDEOS depth profile of a CPP covered steel substrate is shown in Fig. 34. Up to three µm the profile is dominated by the ingredients of the CPP and the pretreatment. Due to the inhomogeneous sputtering of materials with different atomic numbers the maximum of C, O and P is at about 200 nm while Si and Ca have their maximum at 1.2 µm. Ti and Mn are found in the pre-treatment and show their highest value at 2.2 µm.

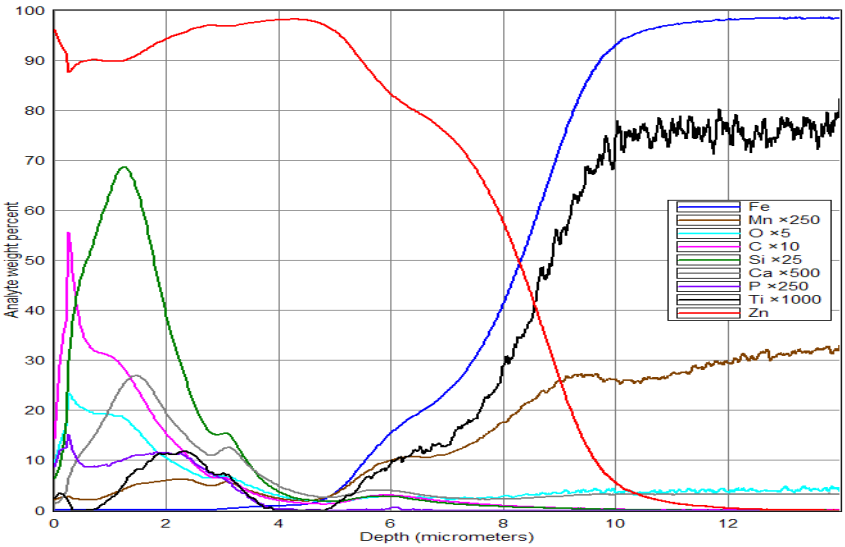

Fig. 34. GDOES element and depth profile analysis of a corrosion protection primer

As the two pretreatment atoms Ti and Mn have the maximum at nearly the same sputtering depth the pre-treatment can be well distinguished from the CPP. The galvanised zinc layer dominates from 3 to 10 µm with an increasing amount of iron for longer sputter times. The non-uniform sputtering leads furthermore to a fluent crossover between the different layers (CPP, galvanised zinc and steel) and the sputter depth can only be used as a rough orientation.

5.2 Uniaxial, biaxial and plane strain forming of corrosion protection primers

5.2.1 Strain evaluation of formed samples

Uniaxially, biaxially and plane strain stretched samples were used to study the behaviour of CPPs during forming. The homogeneous forming in the whole sample area is crucial for a reproducible sample preparation. Therefore a set of model samples was formed and afterwards analysed with respect to their forming state.

The GOM® evaluations of uniaxial stretched samples (5, 10, 15 and 20 % elongation) show at all elongations a homogeneous strain distribution over the complete sample area (Fig. 35). Even at high forming degrees the sample is still in the range of uniform strain and has no tendency for constriction. The forming degrees range from $\varphi_v = 0.05$ for 5 % elongation to $\varphi_v = 0.18$ for 20 % elongation.

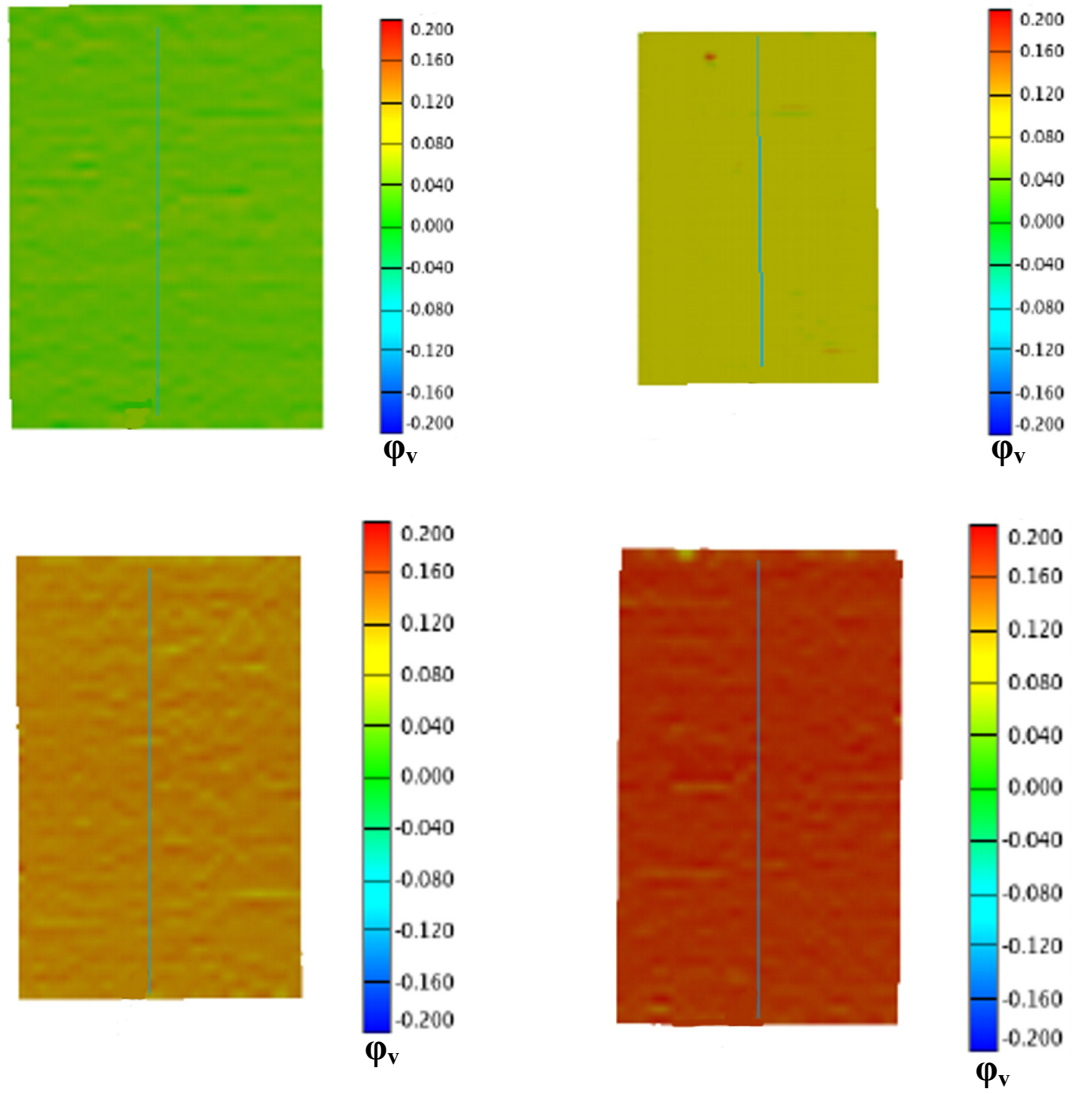

Fig. 35. GOM® analysis of uniaxial stretched steel samples with 5 % (upper left), 10 % (upper right), 15 % (lower left) and 20 % elongation (lower right hand side) showing a homogeneous strain distribution over the complete sample

The forming degrees of the biaxially stretched Marciniak samples were investigated by finite element simulation and by in-situ GOM® analysis during forming in the Erichsen device. The same stamp way was used in both the experiment and the simulation. Three forming degrees φ_v = 0.10, 0.15 and 0.25 were chosen for evaluation from the experiment. All samples show in the middle part a flat area with a homogeneous strain distribution. At the outer rounding the forming degrees are significantly higher. The simulated samples show a slightly lower forming degree especially at the highest forming degree ($\Delta\varphi_v \approx 0.2$). This difference might come from an inaccuracy of the position encoder in the experimental system but all formed

samples showed a reproducible forming. Due to the constant strain in the inner part of the sample this area was cut out and used for further investigations.

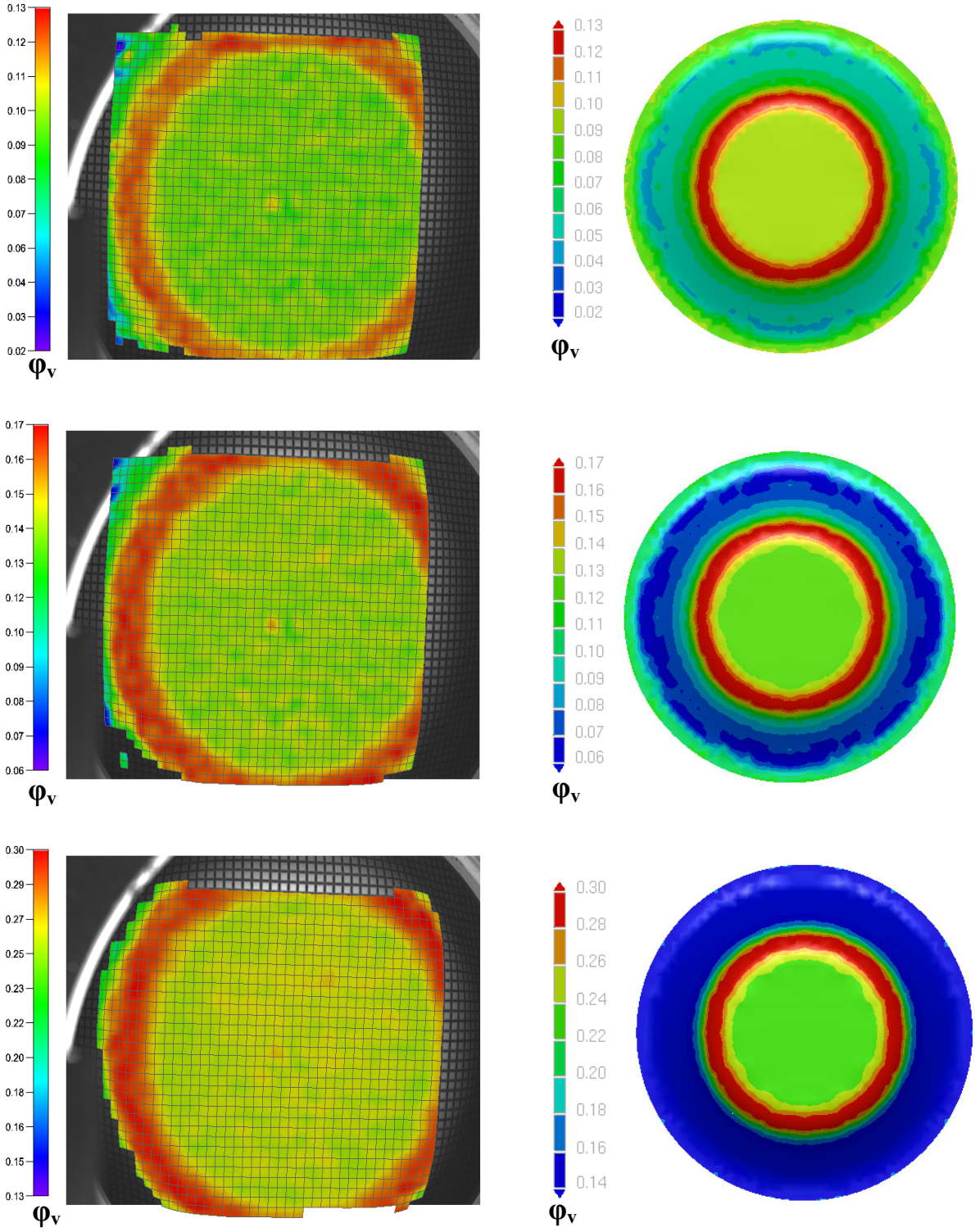

Fig. 36. Optical evaluation (left) and FEM-simulation (right) of a Marciniak samples; top $\varphi_v = 0.10$, middle $\varphi_v = 0.15$ and bottom $\varphi_v = 0.25$ indicating a homogeneous strain distribution in the middle area of the sample

In-situ analysis of plane strain samples shows significant differences in contrast to the biaxially formed samples (Fig. 37). The area of homogeneous forming is limited to a stripe in the middle of the round shaped, flat area of the specimen. The samples were formed with an equivalent forming degree (φ_v) of 0.10, 0.15 and 0.25 in the middle part of the sample.

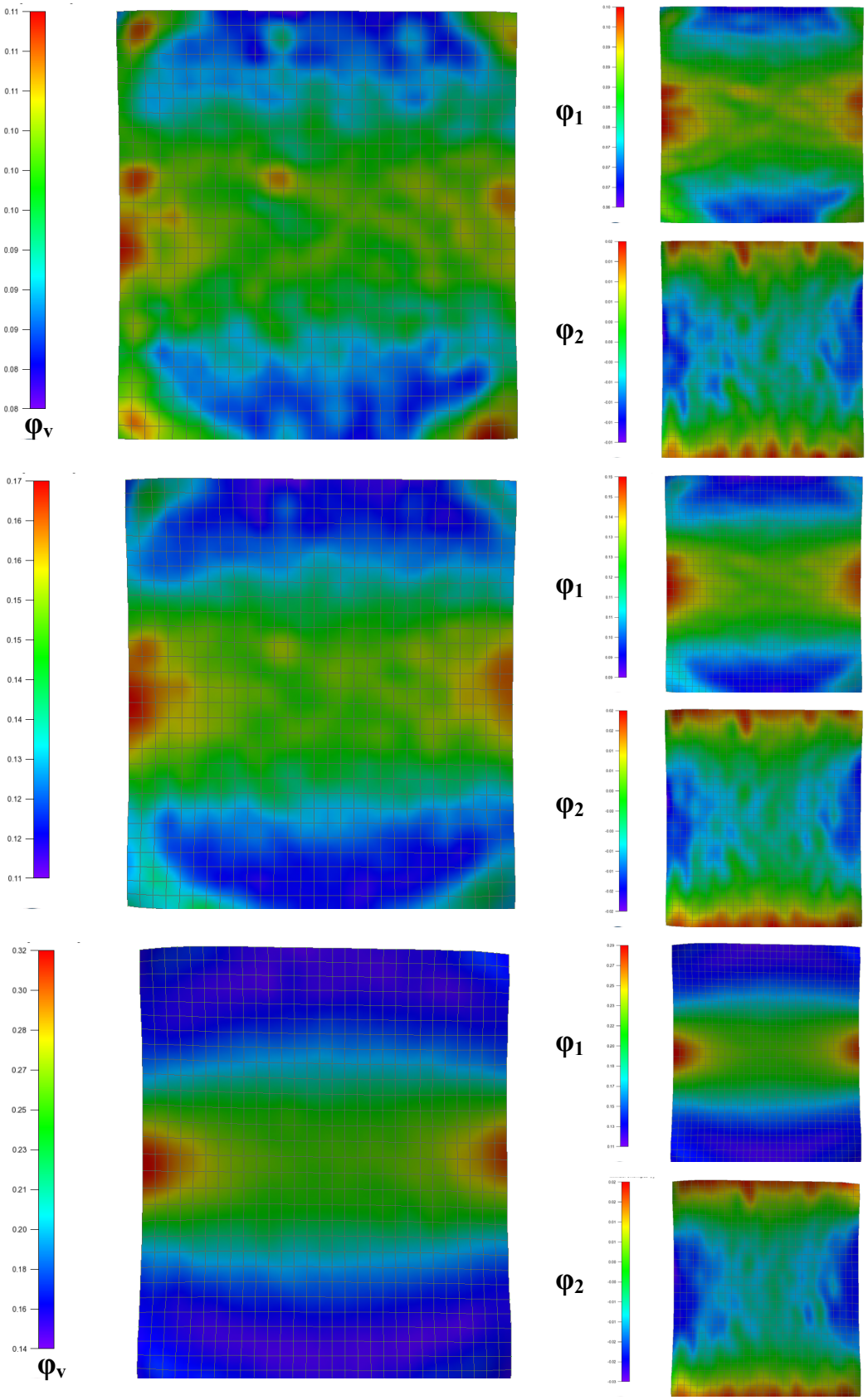

Fig. 37. Optical evaluation of plane strain formed samples ($\varphi_v = 0.10$ top, $\varphi_v = 0.15$ middle, $\varphi_v = 0.25$ bottom), left hand side the equivalent forming degree φ_v right hand side the forming degrees φ_1 and φ_2. The analysis shows only a small area in the middle with a homogeneous strain distribution

Close to the edges where the cut-outs are located (top and bottom of the sample), the major forming degree φ_1 decreases, while the minor forming degree φ_2 rises from zero indicating non-plane strain forming. Also on the left and right sides of the sample the forming becomes inhomogeneous, which becomes visible by the increase of the major forming degree. With higher deformations the transition from the homogeneously to the inhomogeneously formed area becomes more defined and the area of plane strain forming decreases.

5.2.2 Forming behaviour of the electro galvanised steel substrate

The forming behaviour of the electro galvanised steel substrate is of great importance for the corrosion resistance of the complete sample system including the CPP. Defects within the zinc layer lead to conduction pathways and a much faster occurrence of red rust during corrosion tests. Furthermore, defects in the metal coating can result in defects within the organic coating due to an inhomogeneous strain distribution. Therefore, the most demanding forming operation (biaxial forming) was used to investigate the forming performance of the steel substrate.

The SEM images (Fig. 38) of biaxially formed samples (φ_v = 0.10, 0.15 and 0.25) show no damages within the zinc layer.

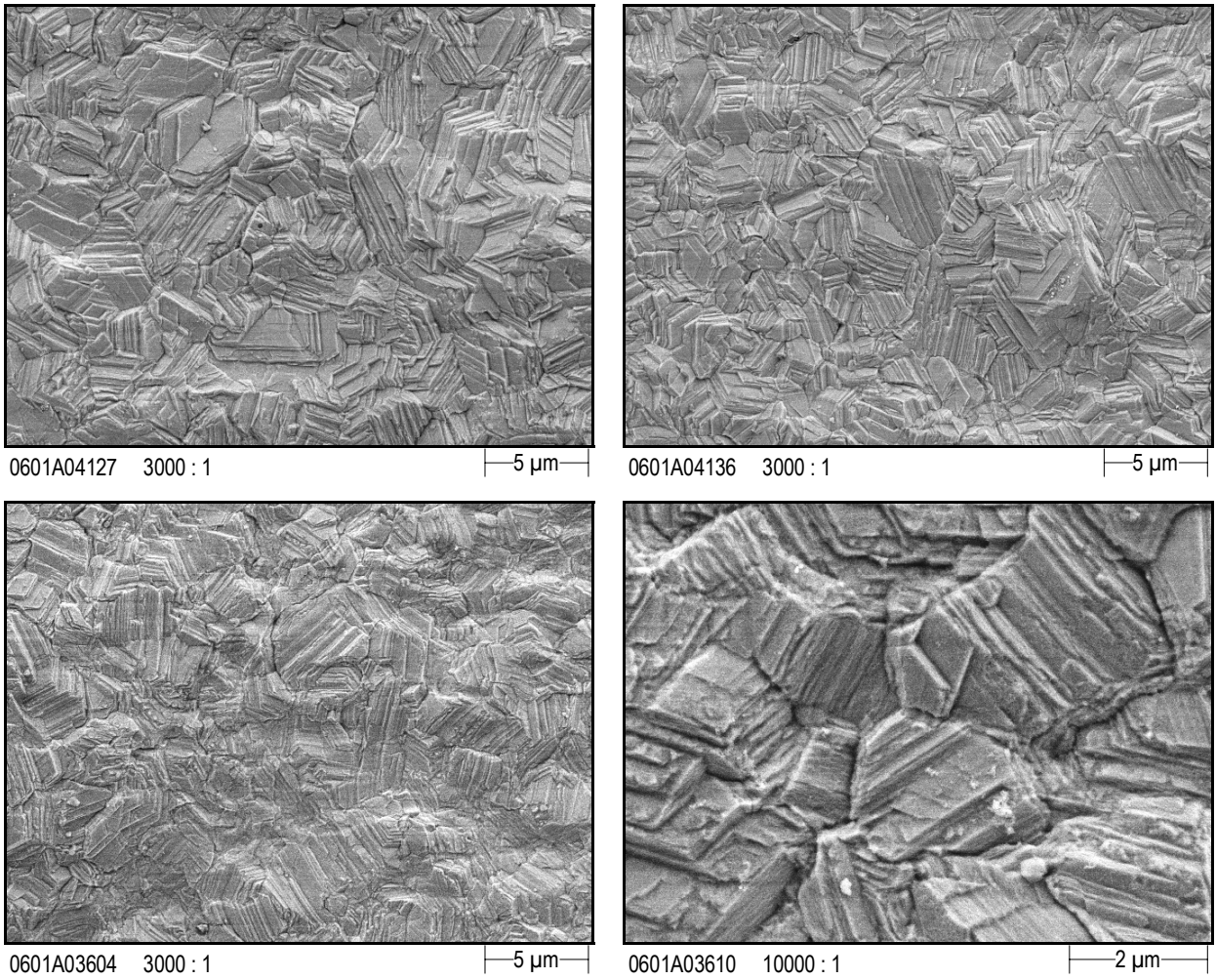

Fig. 38. FE-SEM images of the biaxially formed sample; top left $\varphi_v = 0.10$, top right $\varphi_v = 0.15$ and bottom $\varphi_v = 0.25$ (overview and detail). The images show no damages of the zinc layer due to the forming even for high forming degrees

With increasing strain the surface looks smoother due to the sliding along the terraces of the electrogalvanised zinc structure.

5.2.3 Uniaxial forming of dry corrosion protection primers

The surface morphology of a dry, ex-situ uniaxially stretched corrosion protection primer was studied by FE-SEM (Fig. 39). The samples were elongated to 5, 10, 15 and 20 % ($\varphi_{v,max}$ = 0.18). Even at very low extensions small defects occur within the organic matrix. These defects mainly arise perpendicular to the elongation direction at the interface between the binder and the zinc particles. With increasing strain the defect size rises from a few hundred nm at 5 % elongation to about some µm at 20 % elongation. Furthermore, the number of

defects rises with increasing strain and provides conduction pathways for the electrolyte through the coating.

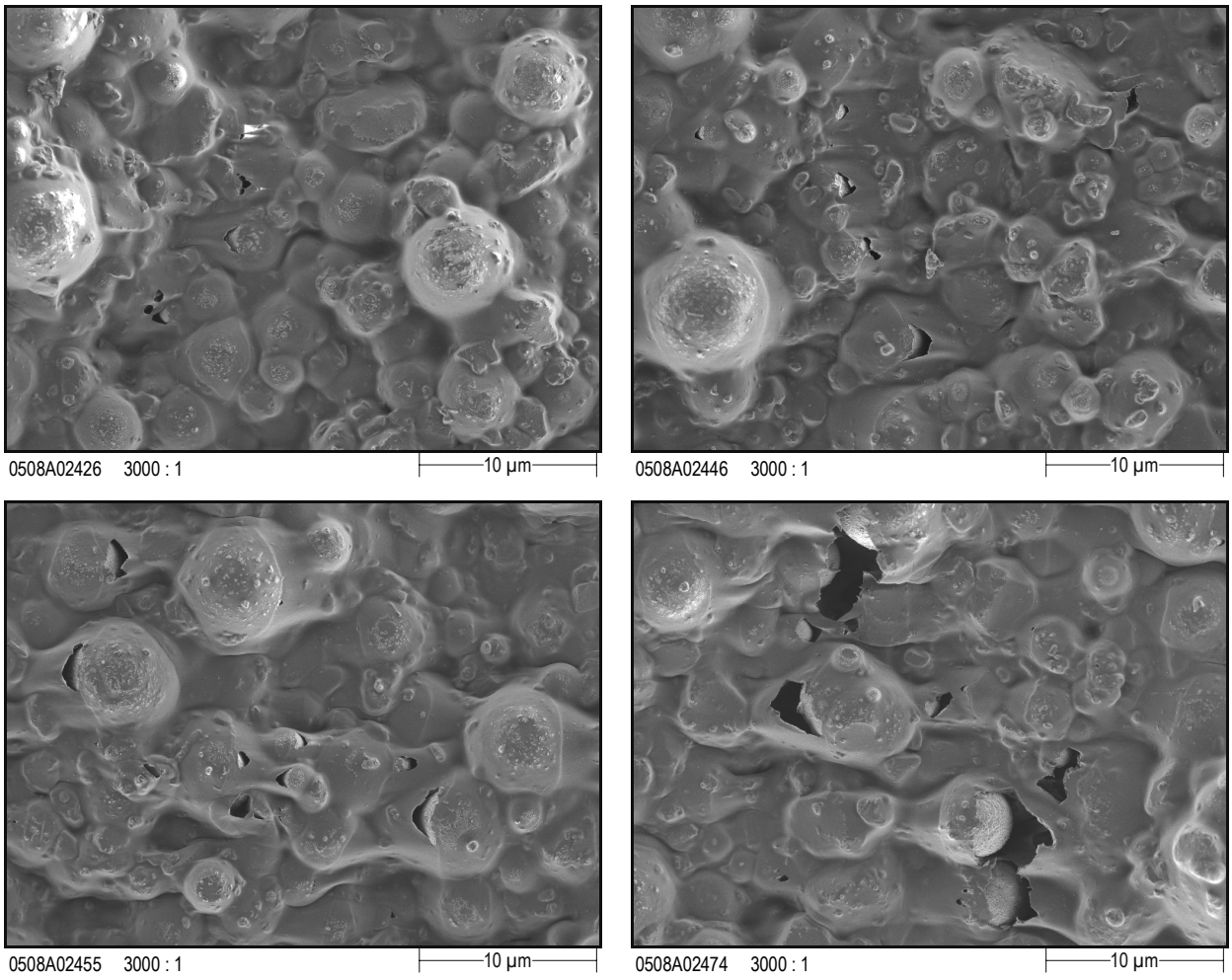

Fig. 39. FE-SEM images of uniaxially formed coil coated electrogalvanised steel samples; top left 5% (φ_v = 0.05), top right 10% (φ_v = 0.08), bottom left 15% (φ_v = 0.15) and bottom right 20% elongation (φ_v = 0.18). Crack formation occurs already at the lowest forming degree. The defect size increases with increasing forming

The FIB cross section of 20 % elongated sample shows the steel substrate covered with the electrogalvanised zinc layer and the corrosion protection primer on top (Fig. 40). The elongated sample not only shows defects at the surface between the particles and the binder but also within the coating. Most of the zinc particles are mainly detached from the binder and float in the organic matrix. Some of these defects might arise by the shrinking of the binder system caused by the thermal input from the gallium ion beam (compare FIB cross section of an unformed sample) but most of them are generated by the sample forming. Apart from the defects visible inside the coating, the binder locally detaches from the zinc surface and forms caverns underneath the coating.

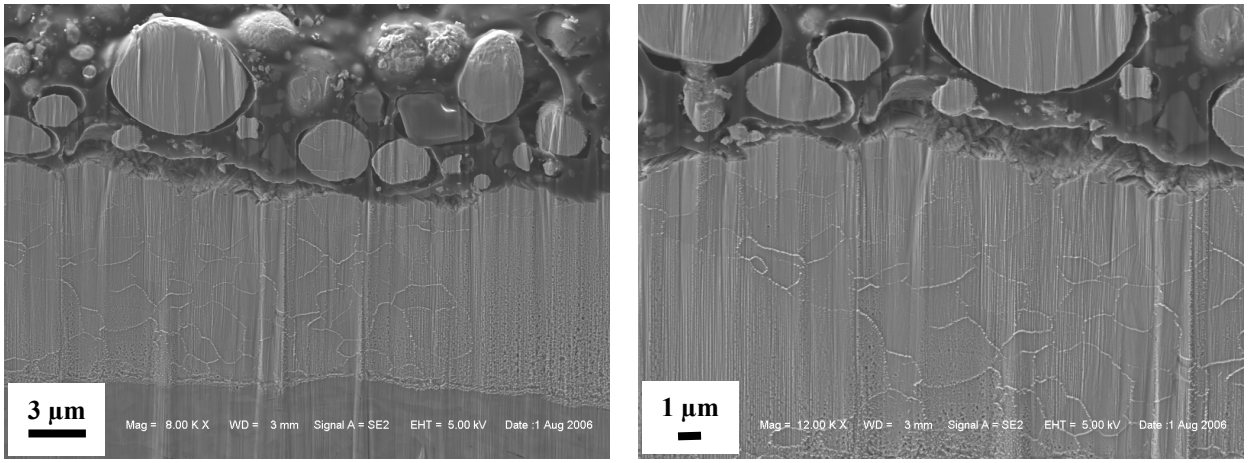

Fig. 40. Focused ion beam cross section of a uniaxially (20% elongation, $\varphi_v = 0.18$) formed primer on electrogalvanised steel, indicating the formation of defects along the particle / binder interface and the binder / substrate interface

In case of good adhesion forces at the particle / binder and the binder / substrate interface some strain might be still unloaded and keep the coating under tension. This could lead to a fast formation of further defects if some external force will be applied as the interface is already weak.

5.2.4 Uniaxial forming of wetted corrosion protection primers

For further in-situ electrochemical investigations during stretch forming it is of great importance that the forming behaviour of a wetted corrosion protection primer is similar to a dry one. Therefore a sample was stored in wet conditions (wrapped in wet tissues and sealed with a plastic foil) for 48 h and was elongated under these wet conditions to 20 %. Afterwards the sample was dried and FE-SEM images were taken (Fig. 41).

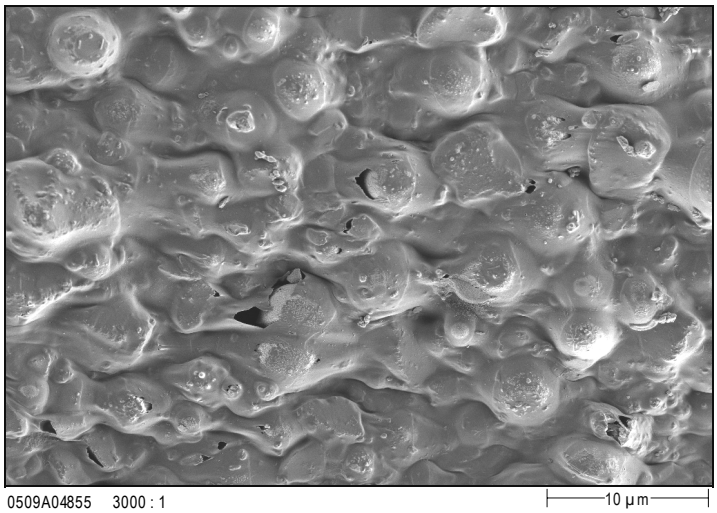

Fig. 41. Uniaxially stretched (20 % elongation, φ_v = 0.18) corrosion protection primer stored for 48 hours under wet conditions. The primer shows the same defect formation as a dry one (see Fig. 39)

The sample shows the same defect formation at the particle / binder interface in the range of some µm which is also visible for a dryly formed CPP. The highly cross linked binder seems to show only a very low water uptake and swelling of the organic film which would cause a softening of the coating and lead to less or no defect formation. Instead the coating shows similar forming properties even under wet conditions. This allows the estimation that the much shorter electrolyte contact (some minutes) during in-situ EIS / stretch forming will have no influence on the forming behaviour of the coated sample.

5.2.5 Biaxial forming of corrosion protection primers

The biaxial forming (Marciniak sample) of corrosion protection primers to φ_v = 0.10, 0.15 and 0.25 leads to similar defects at the pigment binder interface as already known from the uniaxial forming (Fig. 42).

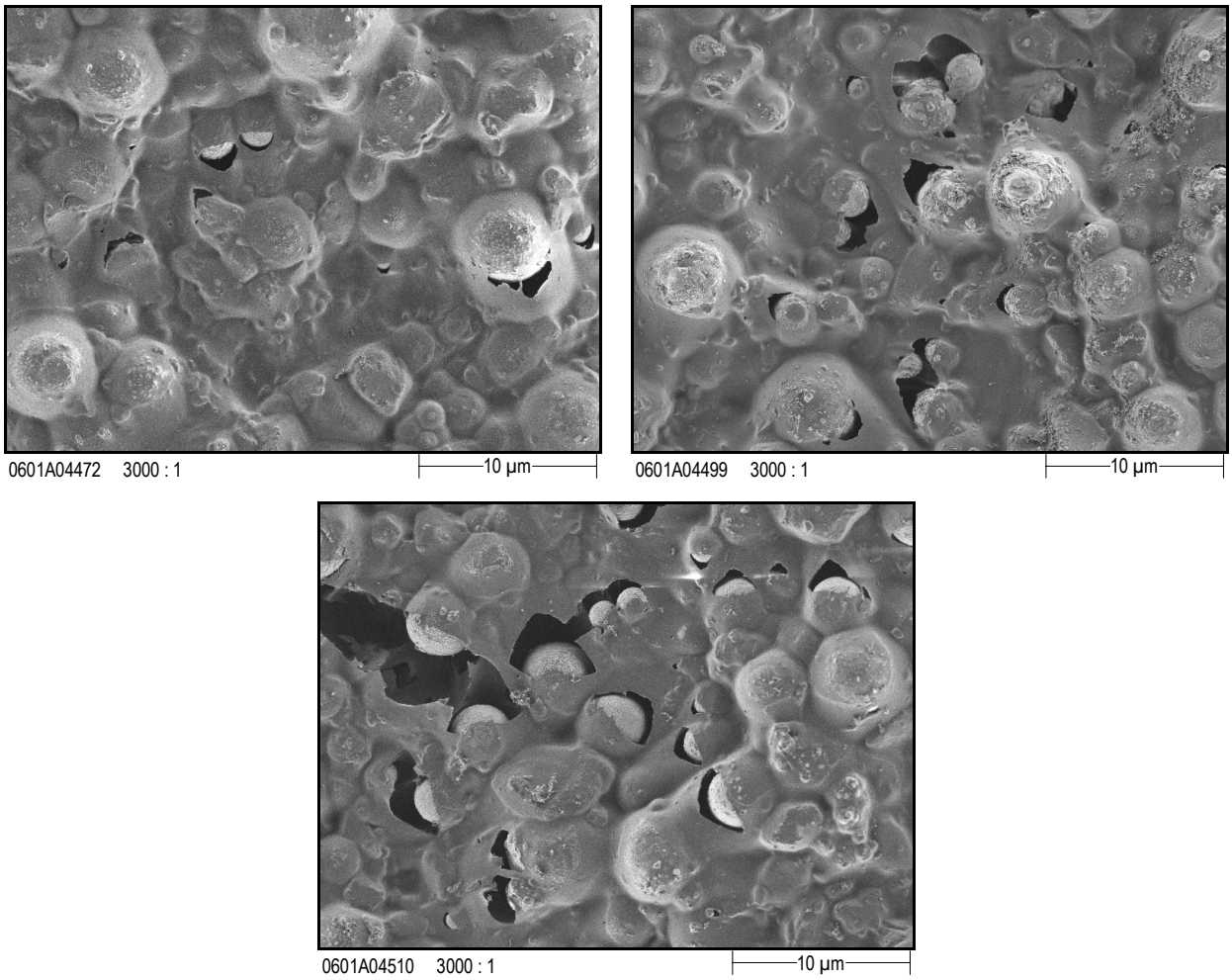

Fig. 42. FE-SEM images of a biaxially formed primer; top left $\varphi_v = 0.10$, top right $\varphi_v = 0.15$ and bottom $\varphi_v = 0.25$. The formed defects show no preferred orientation and grow with increasing strain

The size of the defects increases with the level of strain applied to the sample and reaches up to 15 µm at an equivalent strain φ_v of 0.25. In contrast to the uniaxial forming the defects don't show a preferred orientation anymore as the biaxial strain forces the coating to elongate in equal amounts into the x and y direction. The coating failures lead to partly uncoated zinc particles and to the formation of electrolyte pathways directly to the zinc coated substrate underneath (compare cross section of phosphated sample 5.2.7).

5.2.6 Plane strain forming of corrosion protection primers

Plane strain is the forming step that is placed between the biaxial and uniaxial forming in the forming limiting curve. This means that there is a major forming direction φ_1 in which the material flows. Unlike the uniaxial forming the minor forming degree φ_2 is in this case zero.

The only elongation along the major forming degree leads to the formation of cracks perpendicular to the forming direction which reduces the strain within the coating.
The FE-SEM images show for an equivalent strain of $\varphi_v = 0.10$ initial defects at the particle binder interface in a range of up to one µm (Fig. 43).

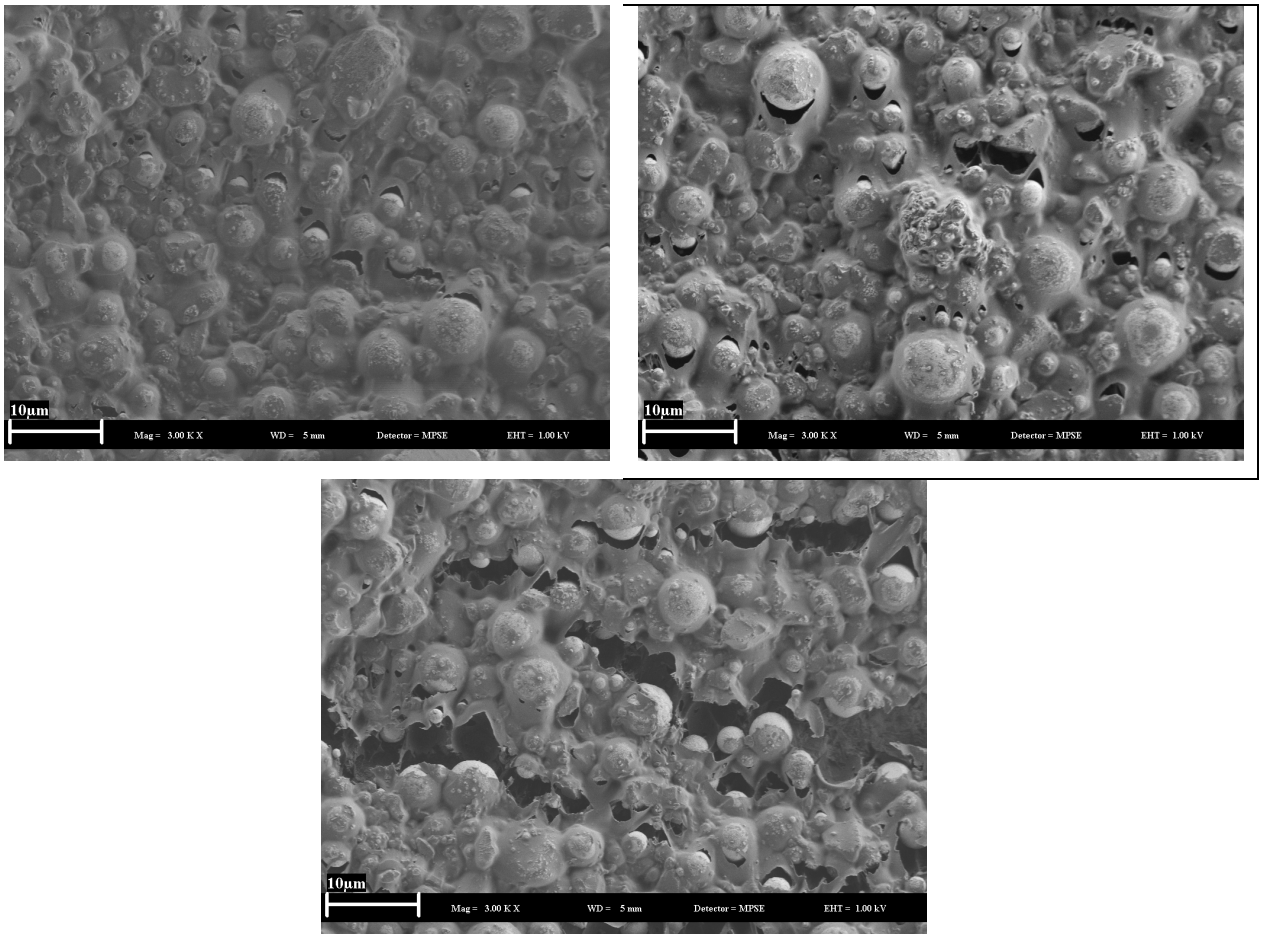

Fig. 43. FE-SEM images of plane strain formed primer, top left $\varphi_v = 0.10$, top right $\varphi_v = 0.15$ and bottom $\varphi_v = 0.25$. The images show the formation of defects along the particle / binder interface which combine at high forming degrees to large defects of some 10 µm

With increasing elongation ($\varphi_v = 0.15$) the number and size of the cracks rises until the separated defects are combined and form large valleys with a size of some 10 µm ($\varphi_v = 0.25$).

5.2.7 Cleaning and phosphating of biaxially formed primers

The automotive tri-cation phosphating is used to increase the paint adhesion on galvanised steel and to passivate the surface. It leads to the homogeneous formation of phosphate crystals on top of the metal surface. The formation of crystals is coupled to an etching process of the

free zinc and the resulting pH-shift of the solution in front of the surface. This leads to a precipitation layer on the metal.

On corrosion protection primers the deposition of phosphate crystals can only happen in areas where the zinc particles of the coating or the zinc layer of the steel substrate are in contact with the phosphating solution to provide the necessary reaction sites. Another important point for the reactivity of the activator (titanium phosphate) and thereby the nucleation of crystals is the surface morphology and the oxide thickness of the zinc. The cleaning procedure (commonly an alkaline cleaning) before the phosphating influences the zinc oxide layer and maybe the morphology of the particles. Therefore, the influence of benzene, mild alkaline and strong alkaline cleaning to the surface structure and the phosphate crystal appearance on formed CPPs was investigated.

The FE-SEM images of the biaxially formed and differently cleaned samples (Fig. 44) show no visible change of the surface structure. The forming induced defects still have a similar size and direction compared to the non-cleaned (see above). The free zinc area of the particles shows a smooth surface and no influence due to the cleaning procedure. Changes in the zinc oxide thickness cannot be assessed by the FE-SEM investigation.

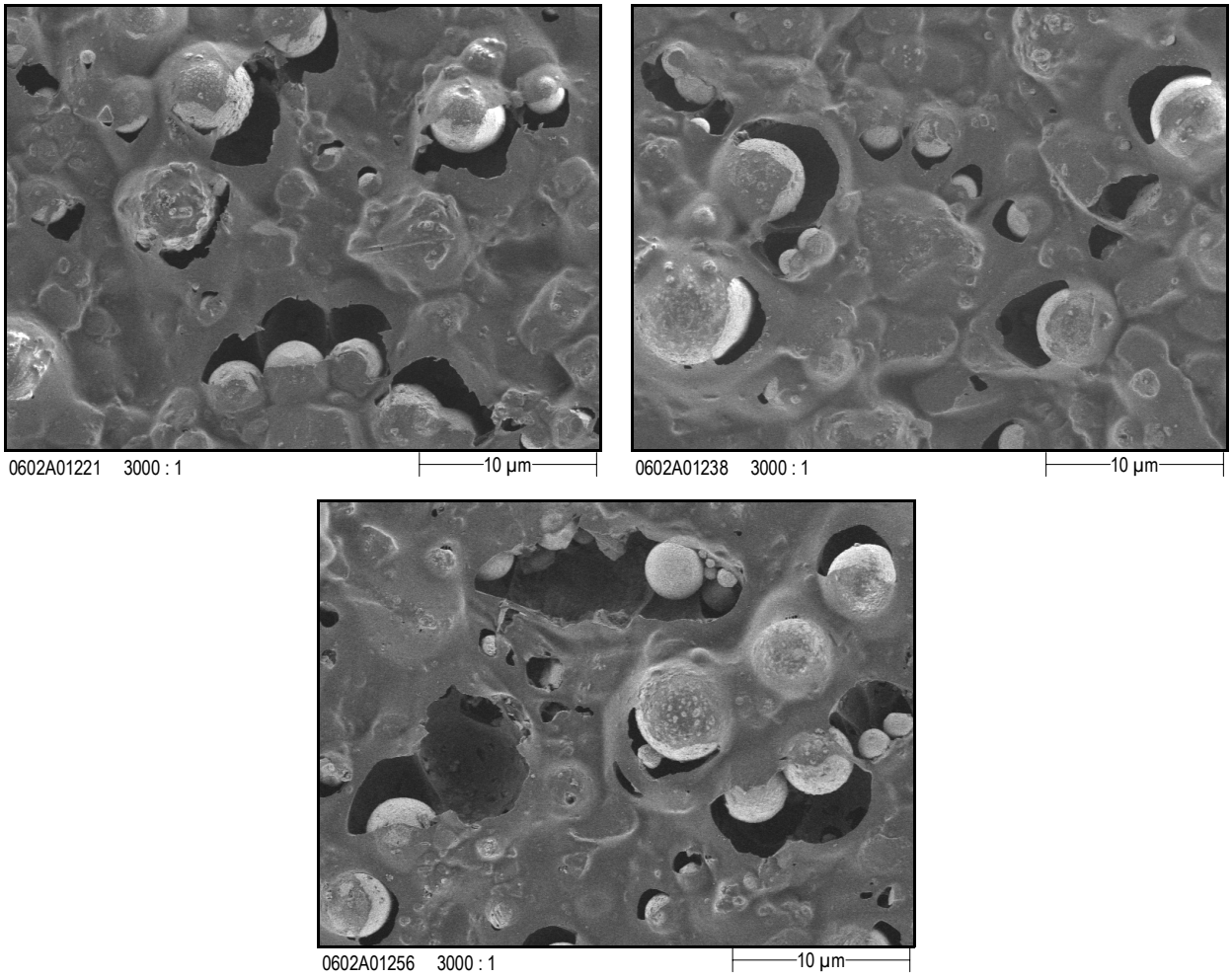

Fig. 44. SEM images of benzene (top left), mild alkaline (top right) and strong alkaline (bottom) cleaned coil coated samples. The cleaning procedure shows no visible influence on the formed primer

The images of the formed and phosphated samples show influences due to the different cleaning procedures (Fig. 45). The benzene cleaning leads to the formation of large phosphate crystals on top of the zinc particles and inside the forming-induced defects. The crystal formation only occurs on free zinc surfaces and defects are partly sealed by the crystals. The mild alkaline cleaning leads to the formation of smaller crystals inside the defects, while the crystals on top of the particles still have the same size compared to benzene cleaning. For the strong alkaline cleaning the crystals inside the defect areas are comparable to the mild alkaline cleaning but in contrast to that the crystals on top of the particles also become much smaller.

First the alkaline treatment seems to influence the free zinc area in the formation induced defects and with increasing pH also attacks the partly organically covered top of the zinc

particles. The reduction of the oxide layer by the alkaline treatment seems to increase the number of nucleation sites resulting in the formation of smaller crystals.

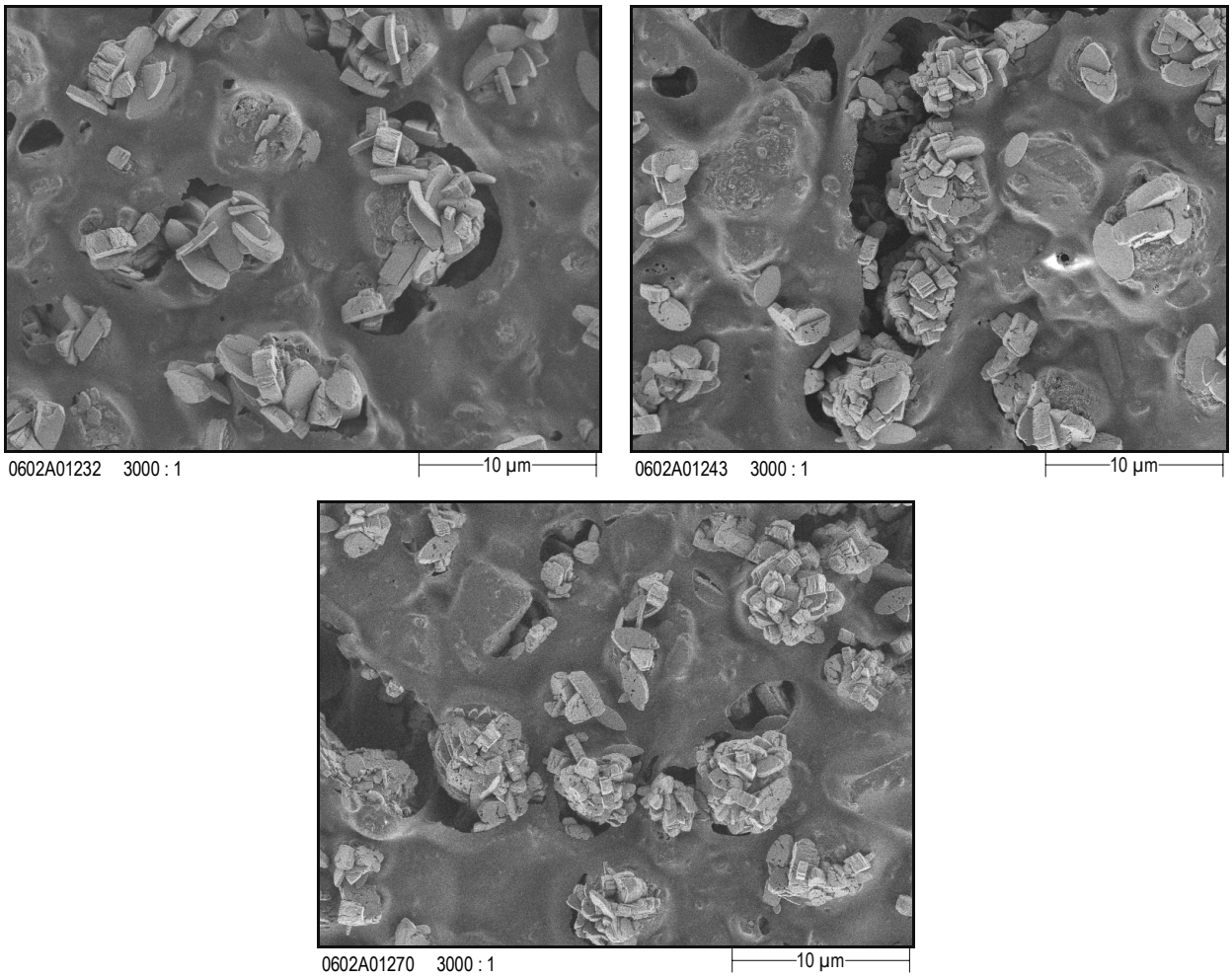

Fig. 45. SEM images of phosphate crystal nucleation on benzene (top left), mild alkaline (top right) and strong alkaline (bottom) cleaned coil coated samples. Slight differences in the crystal formation for the benzene and alkaline cleaned sample re visible

In the FE-SEM cross section the formation of phosphate crystals on free zinc surfaces is visible. The forming induced defects that occur along the pigment / binder interface lead to additional uncovered zinc areas and thereby to the formation of phosphate crystals not only on top but also on the side of the pigments (Fig. 46).

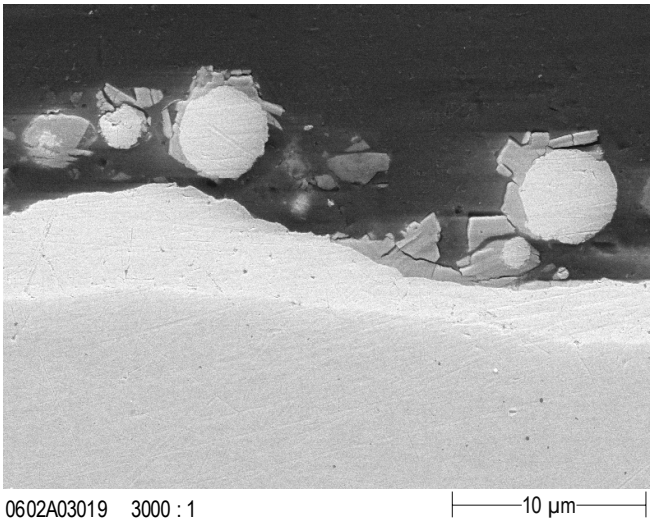

Fig. 46. FE-SEM cross section of a formed and phosphatised corrosion protection primer indicates that the defect formation goes down to the zinc layer and leads to the precipitation of phosphate crystals

Some large defects form conductive pathways through the coating to the zinc layer on top of the steel and enable the crystal growth at the bottom of the defect. The crystal formation leads to a partial sealing of the forming induced defects.

5.2.8 Open Circuit Potential during Phosphating

Unformed and ex-situ stretched samples were phosphated in accordance with a standard automotive process and the open circuit potential (OCP) was measured simultaneously. Fig. 47 displays the development of the OCP during the phosphating step. The coated samples initially show a drop of the OCP to a minimum value between -964 mV and -970 mV (vs. Ag/AgCl) followed by a sharp increase with a maximum value between -905 mV and -892 mV. Finally, the potentials undergo a slight negative shift until they reach a plateau at -920 mV after about 250 s. For more highly strained samples, the slope after the first minimum value rises and the peak OCP is reached in shorter time. In comparison with the coated samples, the uncoated electrogalvanised steel sheet shows a more negative starting potential of -990 mV, followed by a sharp rise with a maximum of -450 mV. The maximum value and the plateau potential of -575 mV are achieved in even shorter times.

The increase of the OCP during phosphating is an indicator of the increasing surface coverage of the metal surface with blocking phosphate crystals similar to the CV experiments conducted by Losch et. al. [158].

When comparing the slope and the peak potential of the uncoated and coated samples, it is important to remember that the phosphating rate depends on the free zinc area. During the

phosphating the zinc surface is etched which leads to a dissolution of zinc ions and a pH-shift in front of the surface. Due to the increase of the zinc concentration and the change in the pH-value the solubility product of the phosphate crystals is quickly achieved and the precipitation starts.

The change in the slope and the peak potential shift for the formed coated samples indicate that the phosphating speed increases at higher elongations due to the quicker achievement of the maximum solubility of the zinc phosphate. As the increase is related to the uncoated zinc surface formed by the uncovered zinc particles in the coating and the free sample surface, an acceleration of precipitation can be correlated with an increase of the free zinc surface by the formation of defects. The differences in the plateau potential arise from an unclosed phosphate crystal layer on top of the coated samples. No dense packing of phosphate crystals occurs within the defect because in most cases only one crystal fits into a defect and it does not completely cover the defect area. The remaining zinc surface is still reactive, which leads to the more negative potential in comparison with the phosphated zinc coated steel substrate.

The acceleration of the phosphating process with increasing strain and therefore increasing defect size is a synergistic effect. The increased amount of reactive zinc surface and the improved adsorption of the activated Ti-phosphates due to the zinc oxide removal by the alkaline cleaning lead to a faster nucleation of crystals.

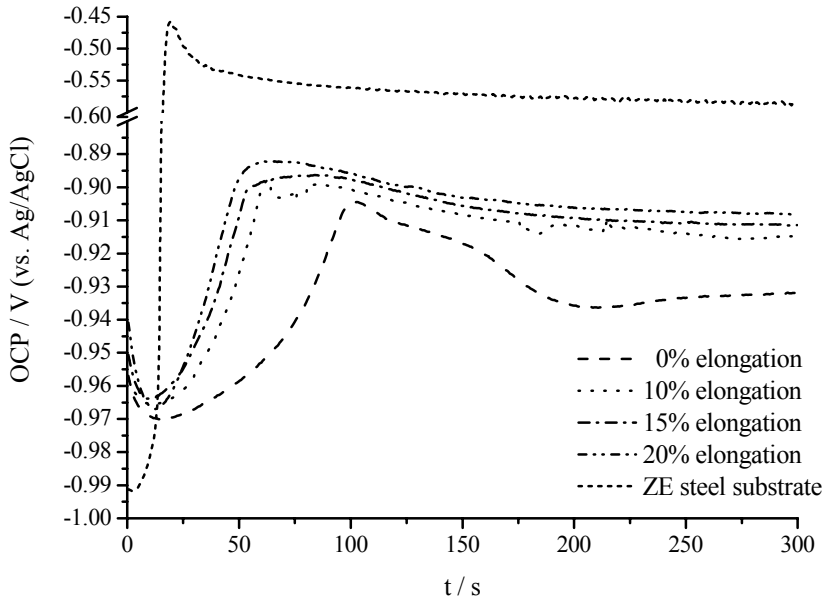

Fig. 47. Open circuit potential of Zn particle containing organically coated and uncoated electrogalvanised steel at different forming degrees during tri-cation phosphating. With increasing strain the phosphating kinetic is accelerated and the final potential is shifted to more positive values

The uniaxially formed and phosphated sample shows phosphate crystal growth only on free zinc surfaces (Fig. 48).

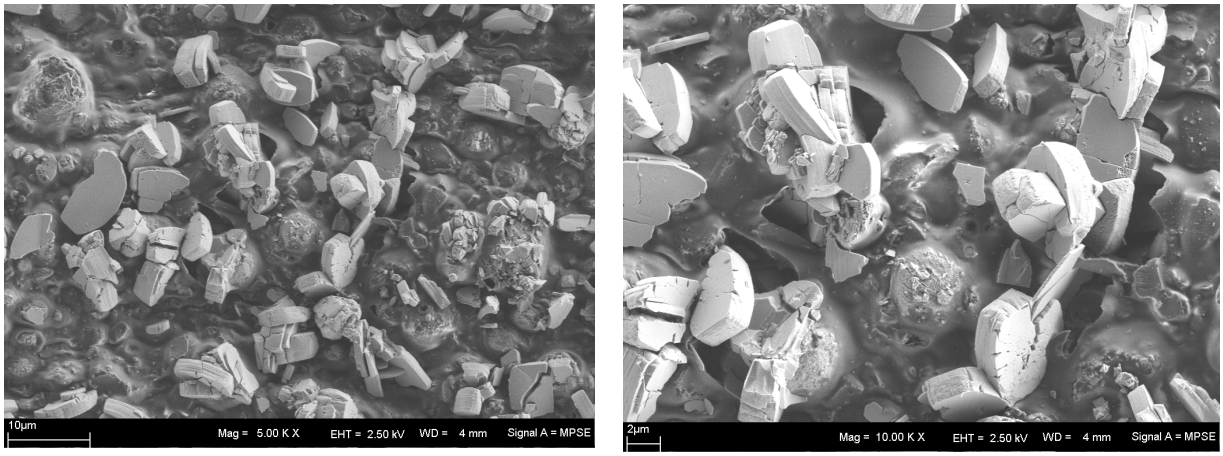

Fig. 48. Overview (right) and detailed top view (left) of a 20 % elongated, organically coated electro-galvanised steel sample after phosphating. The phosphate crystals grow on the free zinc area of the particles (on top and inside the defects)

These surfaces are formed on top of large zinc particles that protrude from the coating and by the formation of cracks at the pigment / binder interface. The SEM pictures clearly support the OCP transient evaluation by illustrating that the remaining defect-free areas range around the formed 3 to 5 µm phosphate crystals.

5.2.9 ED-paint application on corrosion protection primers

The application of corrosion protection primers may allow the reduction of ED-paint thickness while achieving the same corrosion resistance. For the application on outer body parts it is essential that the appearance of the ED-paint is smooth and without defects.

Biaxially formed CPPs (φ_v = 0.25) with reduced ED-paint thickness (11 and 6 µm) were investigated concerning their surface morphology and the defect formation (Fig. 49). The top view shows for both thicknesses a rippled surface. The sample with a thicker ED-paint layer shows a much smoother surface but the structure of the CPP is still visible while the thinner coated sample clearly badges the roughness of the zinc particles.

The uncovered zinc surfaces lead to a local increase of the current density during ED-paint application which increases the deposition rate in these areas. The phosphate crystals on the other hand act as an isolator and hinder the paint deposition. Both effects induce an inhomogeneous thickness distribution of the ED-paint (see cross section Fig. 49).

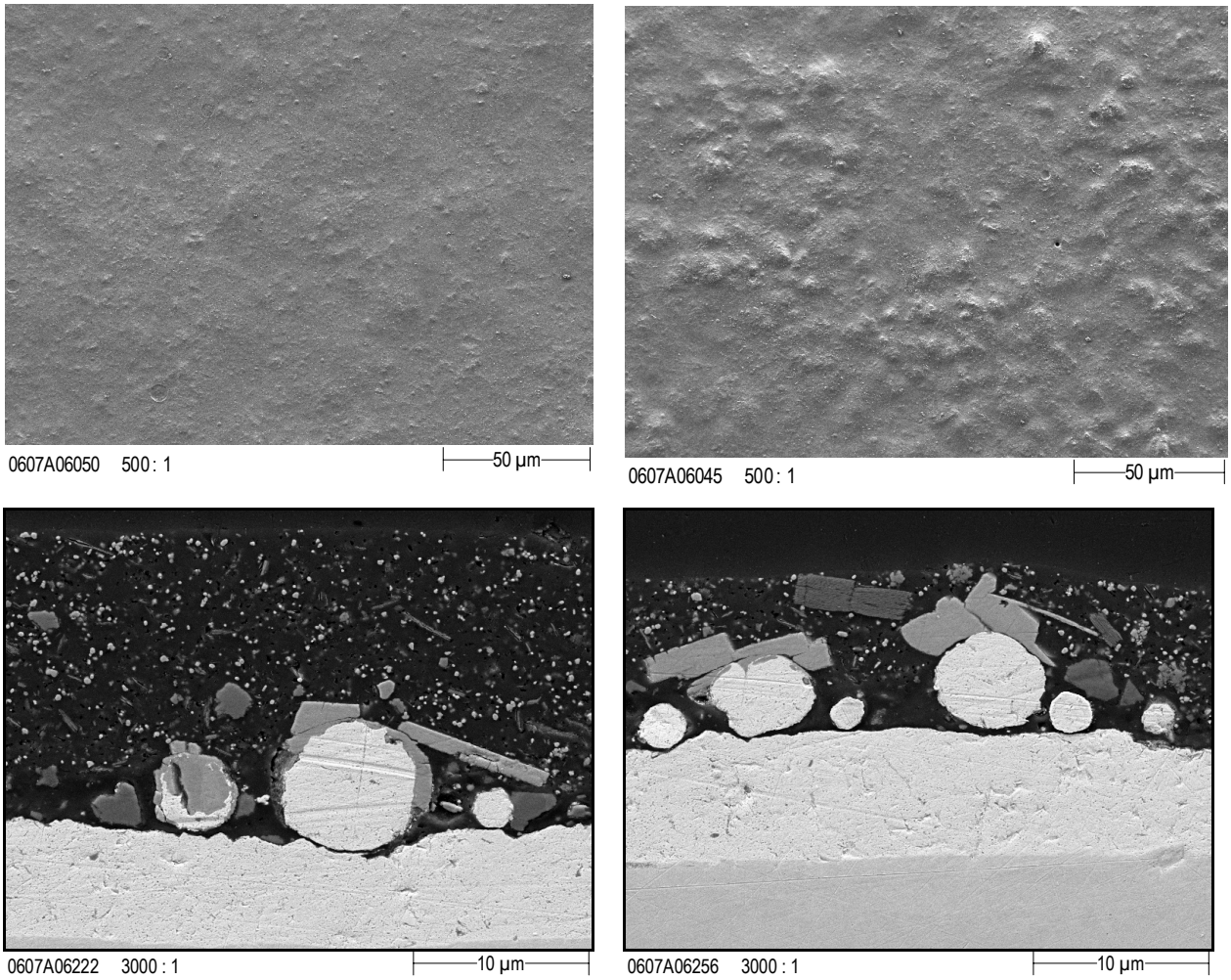

Fig. 49. FE-SEM top views and cross sections of a 12 µm (left) and a 6 µm (right) thick ED-painted primer showing a flattening of the rough surface structure and an inhomogeneous paint thickness

The cross sections show that the inhomogeneous ED-paint thicknesses flatten the surface of the CPP and heal the forming induced defects. But both ED-paint thicknesses still show a very structured surface which might affect the appearance of the following processes.

5.3 Corrosion of corrosion protection primers

5.3.1 Corrosion of formed and unformed primers during standard corrosion testing

The influence of cleaning and forming the corrosion resistance of CPPs was investigated by standard corrosion testing according to the VDA 621-415. The biaxially formed samples were benzene, mild alkaline or strong alkaline cleaned and compared with an unformed mild alkaline cleaned sample. Photos of the sample after different cycles in the corrosion chamber are shown in Fig. 50. The quantitative analysis of the red rust formation is given in Fig. 51. The optical investigation shows no differences between the differently cleaned, formed samples concerning the white rust formation after one cycle and the red rust formation after 5 and 9 cycles. In contrast to the formed samples the unformed sample shows less formation of white rust after 1 cycle and less red rust after 5 cycles of VDA 621-415 testing. After 9 weeks in the testing chamber the corrosive load was so high that the differences between the formed and the unformed sample are no more visible.

Cycle	Benzene cleaned $\varphi_v = 0.25$	Mild alkaline cleaned $\varphi_v = 0.25$	Strong alkaline cleaned $\varphi_v = 0.25$	Mild alkaline cleaned unformed
1	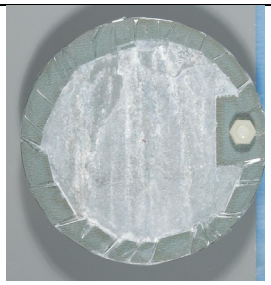	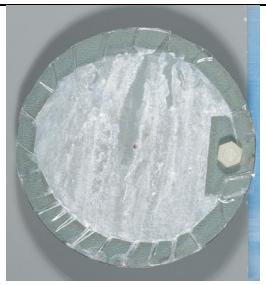	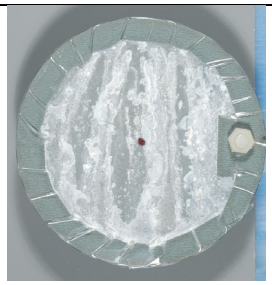	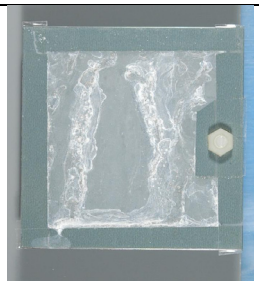
5				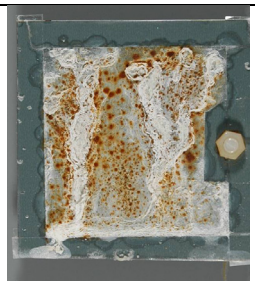
9				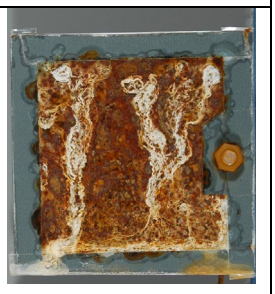

Fig. 50. Biaxially formed and unformed corrosion protection primers after VDA 621-415 testing. The different cleaning procedures show no differences in the formation of white and red rust. The forming of the CPP shows an acceleration of corrosion in comparison to the unformed sample

The quantitative analysis of the red rust formation of the corroding samples confirms the first impressions from the visual interpretation (Fig. 51). The red rust formation is not influenced by the cleaning procedure of the formed samples and already starts after 3 VDA 621-415 cycles. After 5 cycles the maximum of the red rust formation is achieved which means that nearly the complete zinc layer on top of the steel is dissolved. For the unformed sample the first appearance of red rust is also after 3 weeks, but the amount is much less than for the formed samples. Over the whole examination time the amount is clearly less than for the formed sample and only reaches similar values after 8 weeks.

The forming induced defects allow an easier penetration of the corrosive electrolyte and lead to a reduction of the protective properties of the CPP by 3 weeks in the VDA 621-415 test.

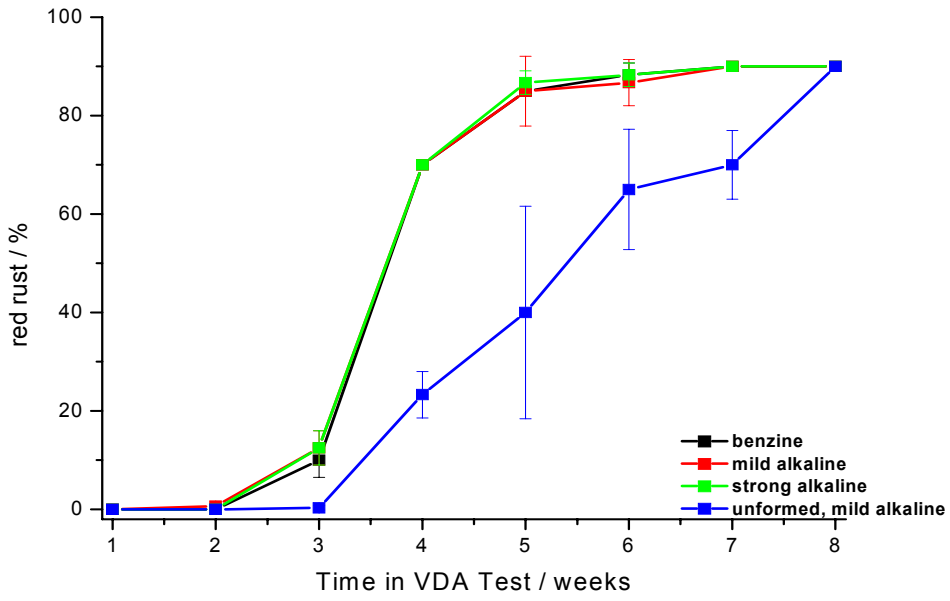

Fig. 51. Amount of red rust formed on a formed corrosion protection primer sample in VDA Test. The unformed sample shows a later and slower formation of red rust, while the different cleaning procedures show no influence

For the use of CPPs with reduced ED-paint thickness especially on the outer body parts it is of great interest when the first blistering appears. Biaxially formed samples were benzene, mild or strong alkaline cleaned and reference samples consisted of unformed mild alkaline cleaned CPP samples and of unformed electro galvanised steel samples. All samples were coated with different ED-paint thicknesses (4, 12, 17 and 22 µm for the CPP samples and 4, 10, 15 and 20 µm for the steel samples). For very low ED-paint thicknesses of 4 µm the unformed CPP and the electrogalvanised sample show in contrast to the formed samples a slightly better resistance with two weeks VDA testing before blistering (Fig. 52).

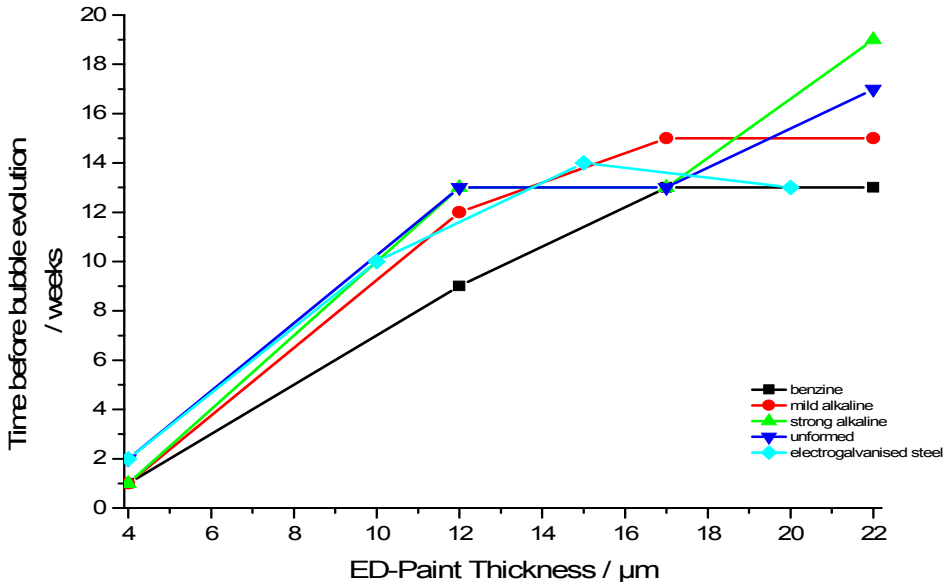

Fig. 52. Blistering of ED-paint applied on corrosion protection primers in dependence on the thickness

At higher thicknesses the results are no more consistent and a strong scattering is visible. This may be caused by the thin CPP layer (3 - 4 µm) in relation to the ED-paint layer (10 – 22 µm) which is thus no more the time limiting step of the blistering. This leads to a strong dependence of the barrier properties on the ED-paint thickness and the homogeneous application.

5.3.2 Salt spray testing of formed primers

For a fast investigation of the corrosion mechanism of formed corrosion protection primers, coated electrogalvanised steel salt spray tests according to DIN 50021 were performed. Due to the high corrosion load the samples were only stored for 24h inside the salt spray chamber.
In Fig. 53 the FE-SEM top view of a uniaxially formed (20% elongation, φ_v = 0,18) and phosphatised CPP is shown. Already after 24 h the surface is covered with thin corrosion products (white rust). These precipitations don't form a compact film on top and show a porous structure at the island edges. The corrosion products mainly appear at areas where defects were formed at the particle / binder interface. Furthermore, the phosphate crystals covering the defects and the top of the zinc particles show a corrosive attack. The smooth, roundly shaped particles undergo an etching attack which leads to a rough and porous surface.

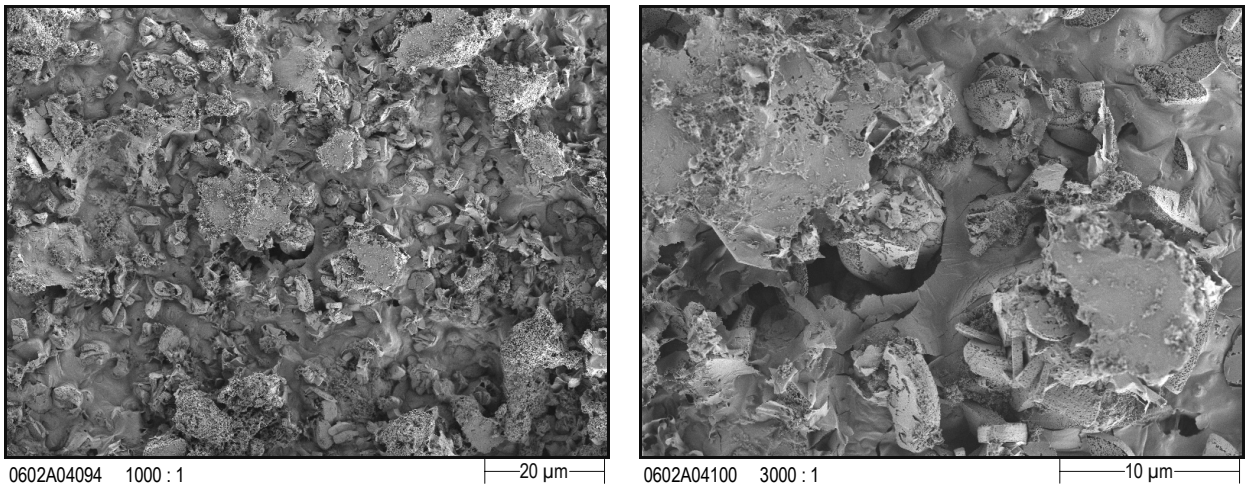

Fig. 53. FE-SEM images of uniaxially formed (20% elongation, $\varphi_v = 0.18$), phosphatised sample after 24h of salt spray testing. The sample is partly covered by corrosion products and the phosphate crystals undergo a corrosive attack

The cross section underlines the corrosion of the phosphate crystals and the formation of corrosion products on top of the CPP (Fig. 54 left). At certain local areas the corrosive attack after 24 h of salt spray testing lead to a completely dissolved zinc layer (Fig. 54 right). For macroscopic investigations the average loss of a blank electrogalvanised sample is about 1 µm zinc / 10 h [159]. In both areas the zinc particles within the coating are mainly intact while the steel zinc layer is strongly corroded. As the particles float within the coating they have no conductive connection to the substrate underneath and can thereby not support the cathodic protection properties of the zinc layer. The local formation of defects and therefore conductive pathways through the coating seems to simplify the corrosive attack and leads to a local increase of the corrosion rate by the creation of sheltered corrosion sites. These corrosion sites can galvanically couple and act either as anode or cathode. The one acting as cathode locally reduces oxygen to hydroxide and significantly increases the pH-value inside the defect. With high pH-values the formation of stable zinc corrosion products is not possible which could passivate the zinc layer and reduce the corrosion rate [160].

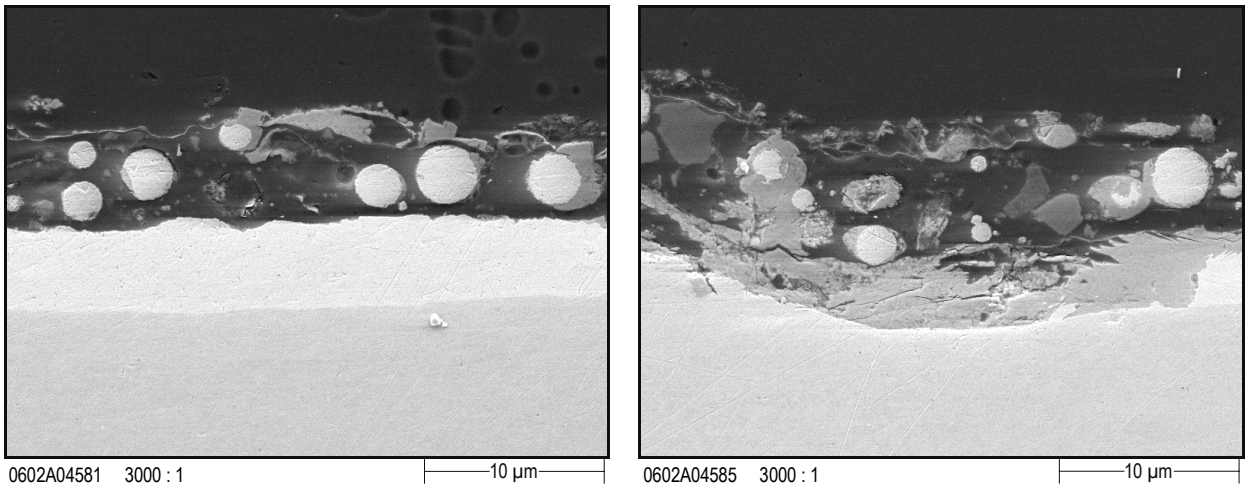

Fig. 54. Cross sections of uniaxially formed (20% elongation, $\varphi_v = 0.18$), phosphatised and 24h exposed in salt spray test corrosion protection primer. In both areas corrosion occurs while in some areas the strong corrosive attack leads to a degradation of the complete zinc layer,

The FIB cross section supports the impressions of the metallographic cross section (Fig. 55). Corrosion products are formed on top of the CPP, while the zinc particles are mainly intact.

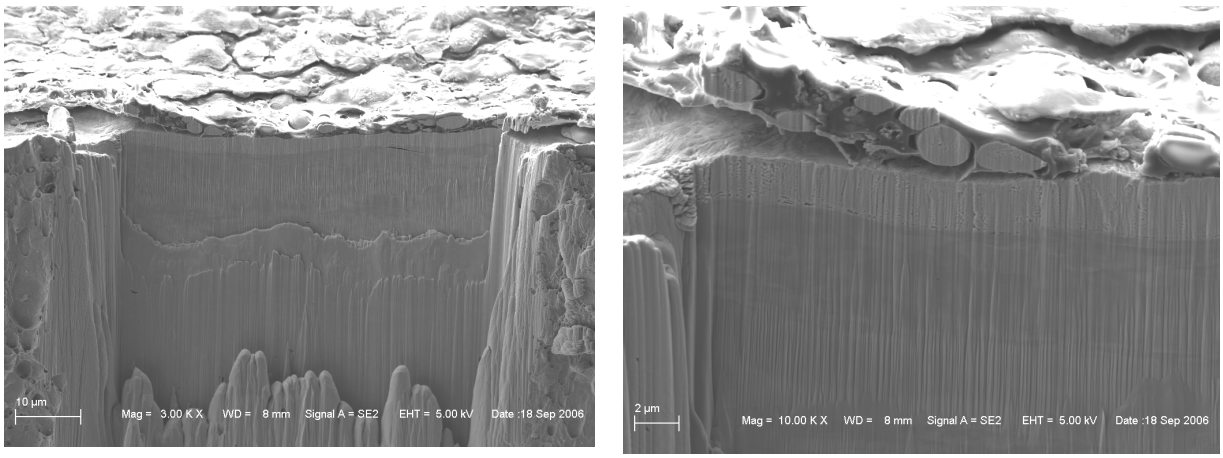

Fig. 55. FIB cross section of uniaxially formed (20% elongation, $\varphi_v = 0.18$) corrosion protection primer after 24h of exposition to a salt spray test. The images indicate the local detachment of the primer from the sample surface and the corrosion of the zinc layer. Most of the embedded zinc particles show no corrosive attack

The coating is detached from the steel substrate in large areas and forms caverns underneath the coating. In the area where large caverns are formed the degradation of the zinc layer is much faster (left side of the image) than in comparison to the smaller caverns (middle part of the image). The corrosive attack of the zinc layer after 24 h in the salt spray chamber leads to a complete removal of the typically tilted electrogalvanised zinc structure.

5.4 In-Situ Electrochemical Impedance Spectroscopy during stretch forming

5.4.1 Forming characteristics of miniature stretching samples

The evaluation of the uniaxially stretched miniature samples by means of optical grid measurements (GOM®) for 5 and 15 % elongation shows a homogeneous strain distribution in the area of analysis (Fig. 56). The major strain φ_1 induced by 15% elongation increases up to 0.16. Even at such high forming degrees, no necking in the middle of the sample becomes obvious. The resulting changes in the minor and equivalent strain can be calculated in accordance with equation 2 and 4 as -0.08 for φ_2 and 0.15 for φ_v.

Furthermore, the forming characteristics of the specimen used were analysed by means of the finite element simulation. For 5, 10, 15 and 20 % uniaxial elongation, the corresponding equivalent strain φ_v is plotted in Fig. 57. In addition to that φ_v also shows a uniform distribution here, especially in the middle of the sample where the working electrode of the electrochemical setup is positioned.

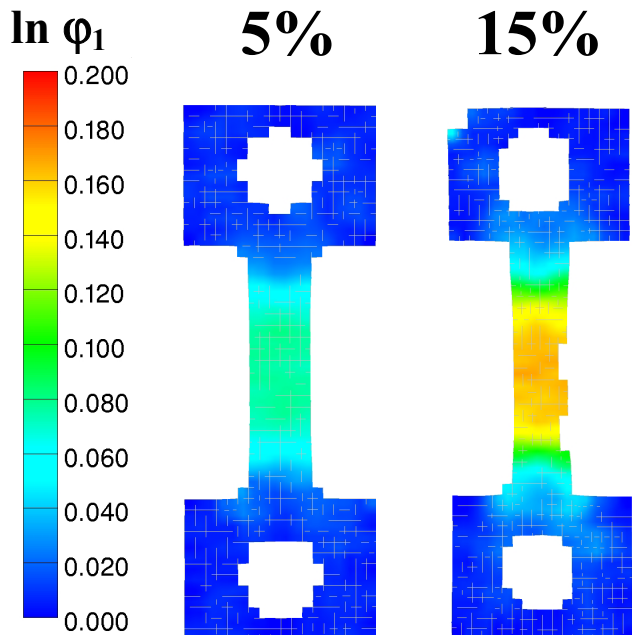

Fig. 56. Major strain distribution of miniature stretching samples measured by GOM® grid evaluation for 5% and 15 % elongation. The sample shows a homogeneous forming especially in the middle where the capillary will be placed

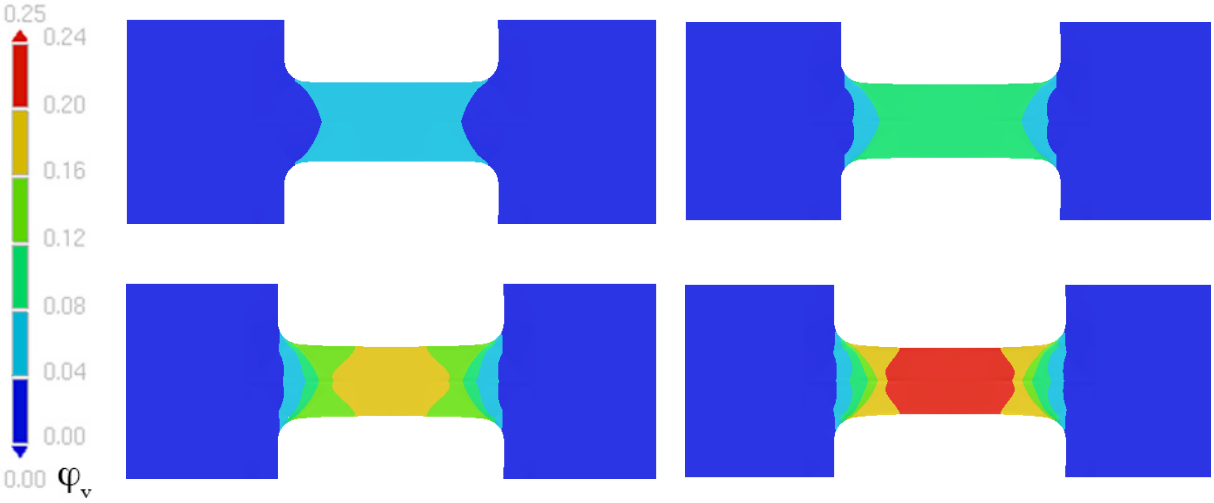

Fig. 57. Finite element simulation of equivalent strain distribution for 5% (top left), 10% (top right), 15% (bottom left) and 20% (bottom right) elongation of miniature stretching sample. Also the simulation indicates a homogeneous forming in the middle of the sample

Both independent investigation methods indicate a uniform elongation with a homogeneous strain distribution for up to 20% stretching.

The comparison of the strain values at 5% strain and 15% elongation shows that the FE simulation and the GOM® grid evaluation concur. For 5% elongation, a φ_v of 0.07 was found for the GOM® evaluation whereas 0.06 was determined for the FE simulation. At high forming degrees, the equivalent strain was calculated to be 0.15 for the GOM® evaluation and 0.16 for the FE simulation.

5.4.2 In-Situ Electrochemical Impedance Analysis during tensile testing

Prior to the in-situ forming experiment, the electrochemical impedance spectra of the uncoated and organically coated substrate in the non-stretched state were measured by means of the capillary cell (Fig. 58).

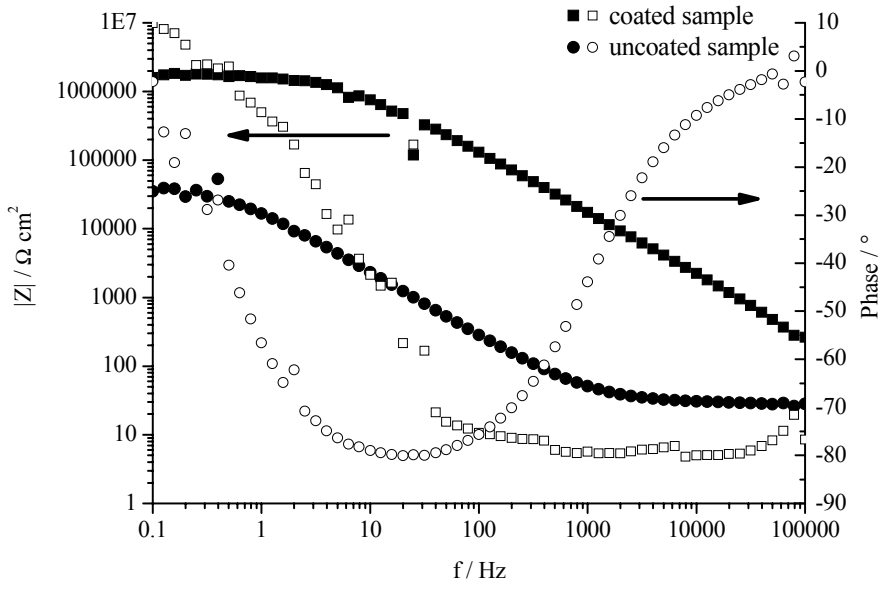

Fig. 58. Uncoated and primer-coated electrogalvanised steel sample in the unformed state, measured by the in-situ EIS setup

The impedance spectrum of the corrosion protection primer sample could be analysed using the equivalent circuit of a defect containing polymer coated metal (Fig. 59). The circuit reflects the properties of the coating by the coating capacitance C_C and the resistance of the coating R_C which is affected by nano and micropores. The double layer capacitance C_{DL} and the polarisation resistance R_P display the properties of the metal electrode underneath the coating that gets into contact with the electrolyte due to the penetration of the electrolyte through the coating defects. The coated galvanised steel showed a capacitive behaviour in the high frequency range between 100 KHz and 100 Hz dominated by the coating capacitance C_C. In the unformed state the delaminated coating area which is responsible for the double layer capacitance is small. This leads to capacitance in the range of the weldable primer (some nF/cm^2). Furthermore, the metal electrode within the equivalent circuit is in series with the high pore resistance of the coating which becomes only dominant at low frequencies due to the parallel connection to the coating capacitance. It is thus not possible for this system to separate the capacitance of the coating (C_C) from that of the double layer capacitance (C_{DL}). At low frequencies the resistance of the coated sample becomes nearly 100 times larger compared to the uncoated sample. In this range the two capacitive terms show extremely large impedance values resulting in the dominating influence of the resistive terms. This leads to a series connection of the coating resistance (R_C), the polarisation resistance (R_P) and the uncompensated electrolyte resistance (R_U) with the dominating influence of R_C as the delaminated area is small.

During the measurement of the high absolute impedance values of the coated sample (up to 250 MΩ for a 1 mm in diameter capillary) the potentiostat showed some scattering when switching the amplifier ranges. Furthermore, the potentiostat showed a phase shift in the low frequency range of about 10° due to the high impedance. The uncoated galvanised steel was used as reference indicating the typical behaviour of a metal in contact with an electrolyte represented by an equivalent circuit without the coating elements represented by C_C and R_C [96]. The measurement indicated that the capillary cell setup is suitable for both the uncoated and even the high impedance of the coated metal substrate.

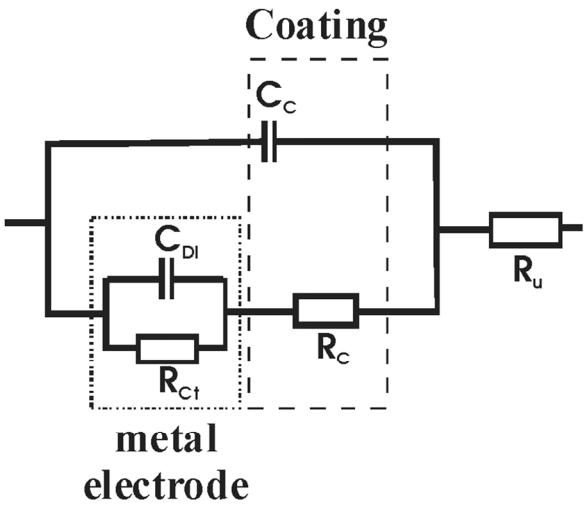

Fig. 59 Equivalent circuit of an organically coated metallic sample

The in-situ EIS evaluation during the stretching of the primer-coated substrate in borate buffer is shown in Fig. 60. In the unformed state and for small forming degrees (≤5 % elongation), the coating shows good barrier properties with an almost capacitive behaviour above 100 Hz and a phase angle of 70 to 80°. In the low frequency range the coating shows resistive behaviour by the combination of R_U, R_C and R_P. At these small forming degrees the delaminated area is still small and the system is dominated by the coating capacitance and the high coating / pore resistance. With increasing strain, the barrier properties of the coating decrease due to the formation of cracks and new electrolyte pathways. Furthermore, the delaminated area at the coating substrate interface increases. These effects lead to a decrease of the coating resistance (R_C) and due to a rise in the contact area of the metal electrode with the electrolyte to an increase of the polarisation resistance (R_P), the double layer capacitance (C_{DL}). These result in an increase of the phase shift at high frequencies reaching 0° for an equivalent strain of 0.22. At this forming degree the delamination and the defect formation of the coating lead to a nearly complete breakdown of the barrier properties. The measured

impedance and phase values thus become comparable to those of the bare zinc coated substrate elongated to 25%. For all elongation degrees, the low frequency resistance at 0.1 Hz shows a resistive behaviour by a combination of R_U, R_C and R_P which decreases by two orders of magnitude for high strain values. The small final impedance value indicates that the dominating influence of the coating resistance in the equivalent circuit decreases and the overall impedance is mainly dominated by the polarisation resistance.

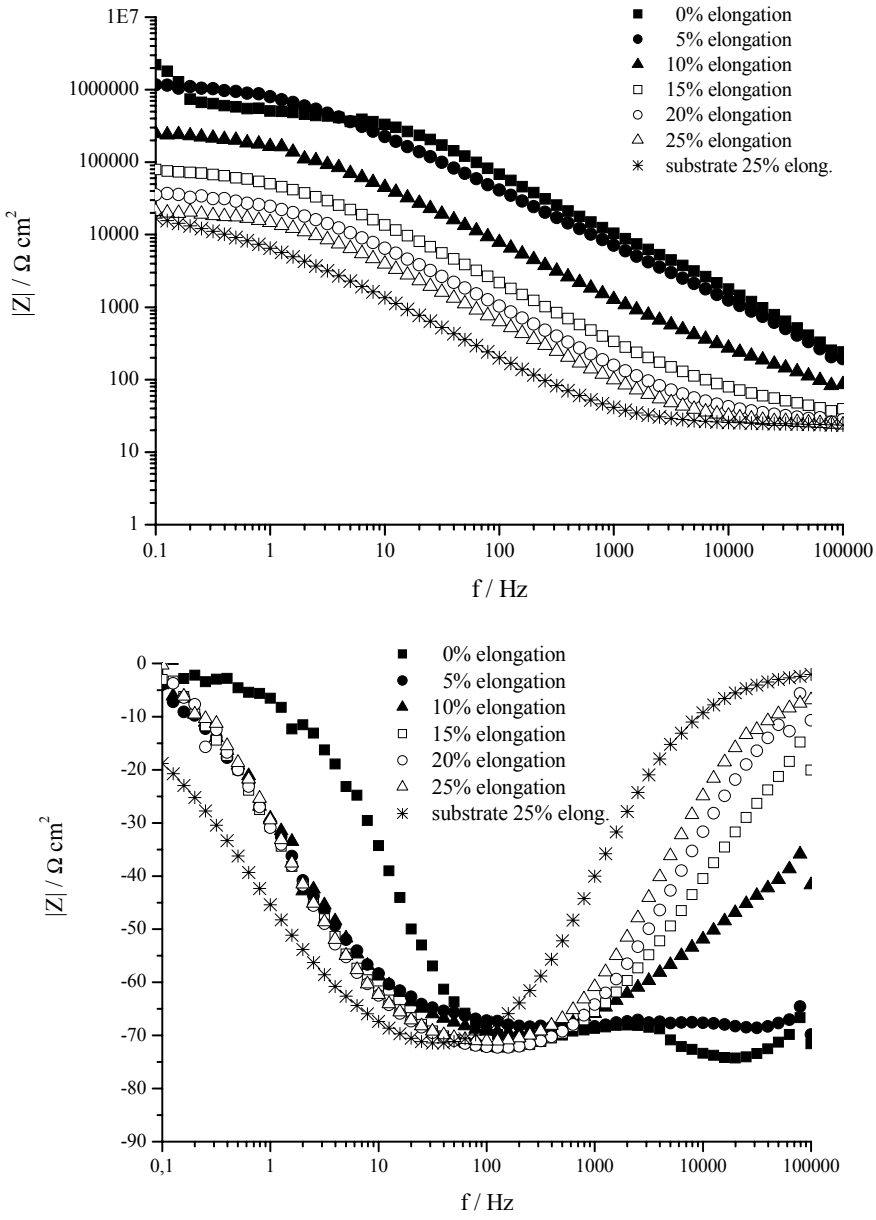

Fig. 60. In-situ EIS evaluation during stretch forming of a Zn particle containing coating in borate buffer (impedance (top) and phase shift (bottom))

The same in-situ experiment using 0.05 M NaCl as electrolyte shows similarly shaped impedance spectra for the unstrained sample (Fig. 61) which can be interpreted by the same

equivalent circuit as for the borate buffer experiment. Differences appear in the shift of the capacitive behaviour to higher frequencies between 100 kHz and 1000 Hz and by total impedance which is one order of magnitude smaller. These differences seem to arise as a result of the strong corrosive effect of the chloride ions causing a fast attack on the passive film on zinc and a faster delamination of the coating. Even at elongations of about 5-10 %, a significant decrease in the coating barrier properties becomes obvious with a drop in the low frequency resistance by one order of magnitude. At high forming degrees, the decay of impedance becomes slower until it reaches about 3000 Ω cm^2 at 1 Hz, which is again a value close to that for the bare galvanised substrate at this forming degree.

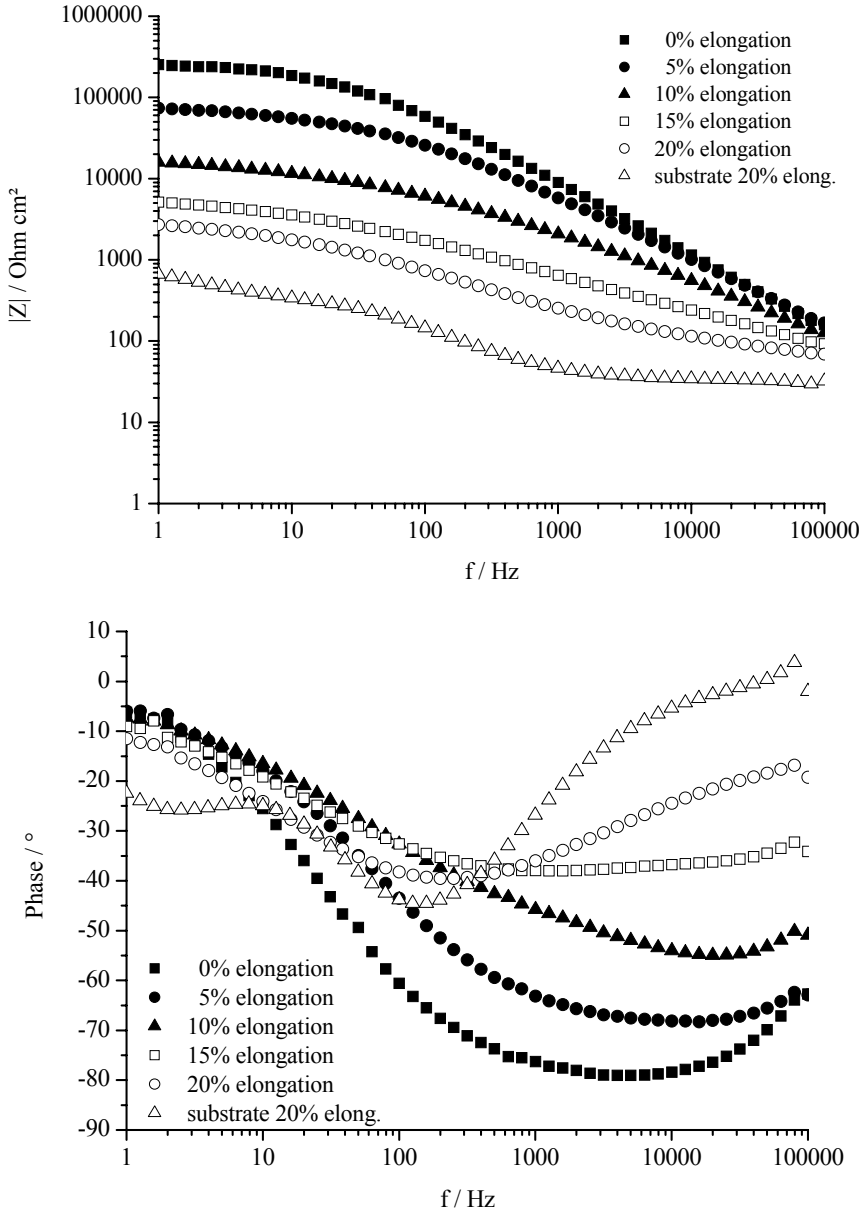

Fig. 61. In-situ EIS evaluation during stretch forming of a Zn particle containing coating in 0.05 M NaCl (impedance (top) and phase shift (bottom))

A complete evaluation cycle between 0 and 25 % elongation takes about 30 min during which the sample is stretched and the impedance spectra are analysed. During the whole measurement process the sample is in contact with the electrolyte and can undergo a corrosive attack even without forming. For this reason, the impedance spectra of an unformed, organically coated specimen were measured in borate buffer and 0.05 M NaCl over a period of 30 minutes to obtain a reference measurement.

The low frequency impedance at 1 Hz is characterised by the series of the uncompensated electrolyte, the coating resistance and the polarisation resistance. The electrolyte resistance can be regarded as constant. While the coating resistance decreases during the degradation of the coating and the polarisation resistance increases with the amount of delaminated area. The coating resistance is in the initial state about 2 orders of magnitude larger than the polarisation resistance. Thus, significant changes of the cumulated resistance should be mainly caused by a change of the coating resistance. Therefore the impedance at 1 Hz was plotted as a function of time and elongation (Fig. 62).

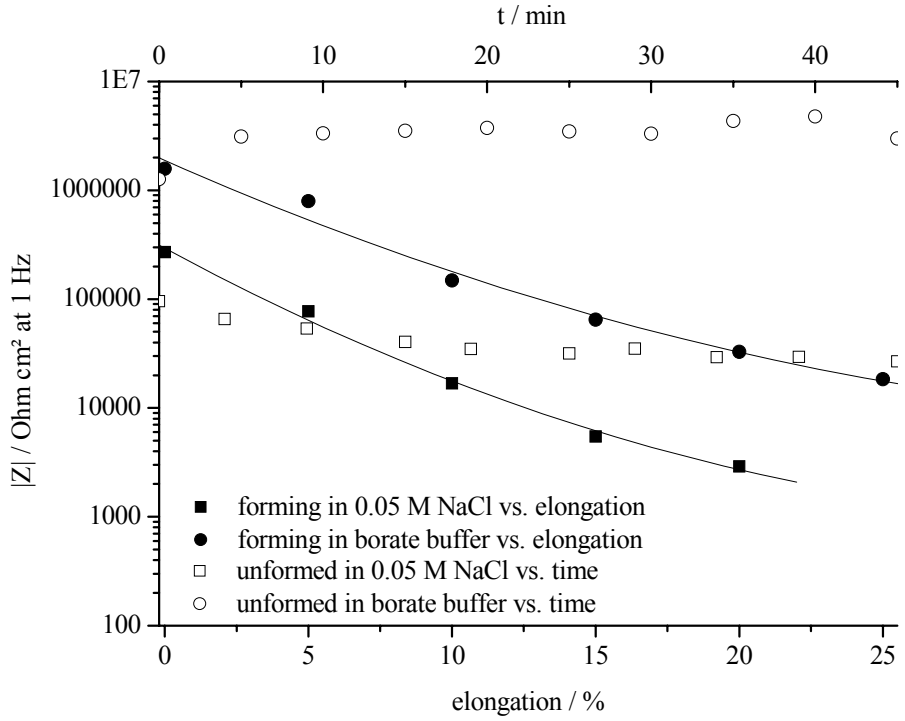

Fig. 62. Decrease of the resistance at 1 Hz for primer-coated samples in relation to the forming degree and for unformed samples in relation to the electrolyte contact time

Due to the corrosive properties and the delamination, the sample in contact with sodium chloride electrolyte showed a slight decrease in the combined resistance after 30 min of

immersion. The immersion in the chloride-free borate buffer leads to a nearly constant value of the low frequency resistance over time.

Furthermore, Fig. 62 shows the decrease of the coating resistance as a function of the induced strain. For both electrolytes, the forming induced changes of the impedance values are much more significant than the corrosive and delaminating attack of the sodium chloride over time. At high forming degrees, the coating loses almost completely its protective properties due to the formation of defects. In the case of the NaCl electrolyte, the contribution of the corrosive attack leads to a slightly increased degradation of the coating performance. Thus, the corrosion and delamination of the coating and the forming induced defects cannot be clearly separated, while the change in borate buffer is caused by the increase of the defect size and density. For the in-situ measurements of the forming-induced defect formation and growth the measurements should be carried out in chloride-free environments.

5.5 Scanning In-situ EIS / Raman investigations of formed corrosion protection primers

The simultaneous analysis of Raman and impedance spectra generates information about the barrier properties and the formation and change of corrosion products. The combination of an electrochemical capillary cell with a confocal Raman spectrometer allows the switching between the two investigation methods on the same sample spot.

5.5.1 Scanning In-Situ EIS / Raman investigation of corrosion products on plane strain formed primers

The new setup was used to investigate the barrier properties and the corrosion formation of a plane strain formed (φ_v = 0.25) corrosion protection primer. The Raman spectra were taken before and after 150 min of impedance analysis (electrolyte 0.5 M NaCl) with a HeNe Laser (Fig. 63).

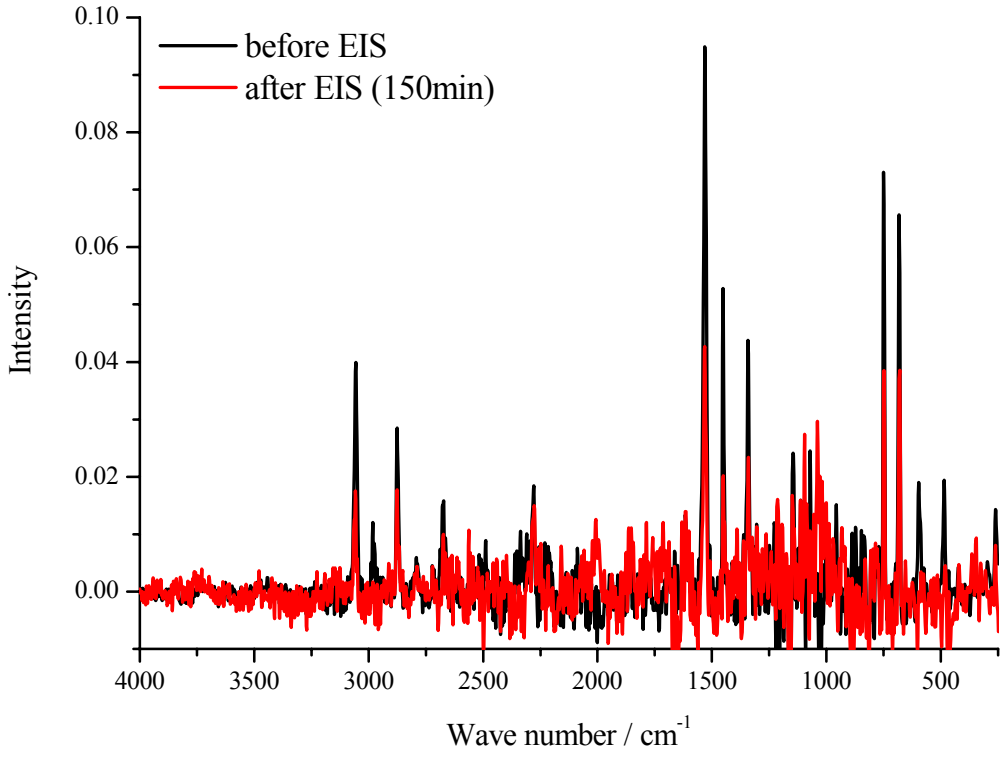

Fig. 63. Raman spectra of a plane strain formed (φ_v = 0.25) corrosion protection primer before and after impedance measurements in 0.5 M NaCl

The CPP shows strong fluorescence in the complete range from 4000 to 250 cm^{-1} with two maxima at about 2400 and 1100 cm^{-1} and were baseline corrected for further investigation.

However, peaks of the organic binder matrix and zinc are still visible and are assigned in Tab. 4. The implemented zinc particles and / or the electrogalvanised zinc layer underneath the coating which might be visible through the forming-induced defects already show the formation of corrosion products before electrolyte contact. For both spectra (before and after impedance measurement) the same signals appear indicating no significant change in the formed corrosion products. The signal intensity on the other hand shows a small decrease in intensity after the impedance measurement which might occur due to the dissolution and formation of soluble corrosion products by the chloride containing electrolyte. For the formation and precipitation of significant amounts of corrosion products the corroding time of 2.5 hours seems to be too short.

Tab. 4. Assignment of signals gained by Raman spectroscopy of a plane strain formed (φ_v = 0.25) corrosion protection primer before and after impedance measurements in 0.5 M NaCl

Wave number / cm^{-1}	Assignment
3055	C-H
2875	CH_2
2280	N=C=O
1529	
1452	C-C
1341	N-H
1145	Zn-O
750	
681	O-H
595	Zn-O
485	Zn-O

In contrast to the Raman spectra the impedance measurement shows dramatic changes over the investigation time (Fig. 64). Starting with an already low frequency impedance of 2000 Ω cm^2 due to the forming induced defects the value drops by nearly one order of magnitude during the measurement. In the range from 100000 to 200 Hz the coating shows especially at the beginning a strong capacitive behaviour with a phase shift of -65 ° decreasing down to -20 ° over time. The double layer capacitance visible with its phase minimum at 60 Hz is overlaid by the coating capacitance at the beginning and later on shows only a phase shift of -20 ° due to the corrosive attack of the zinc layer.

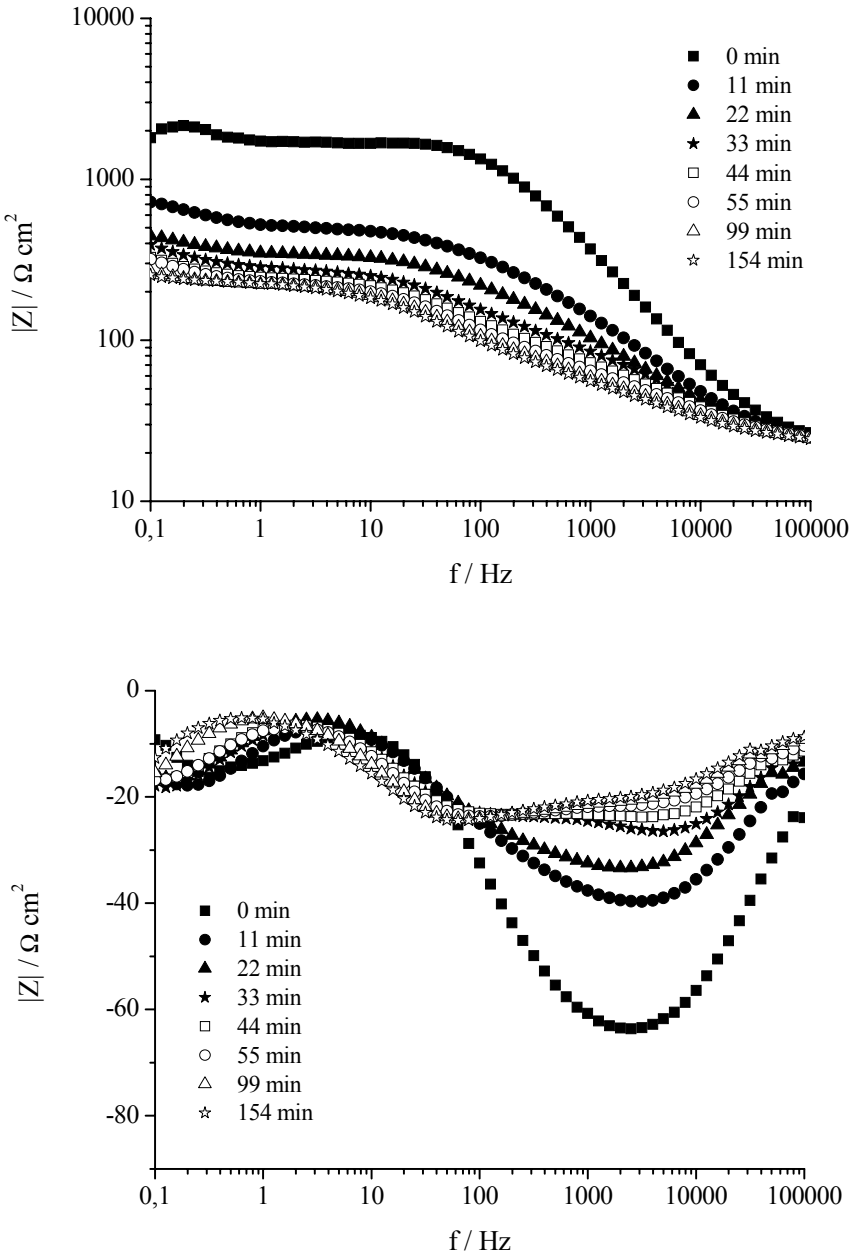

Fig. 64. Combined Electrochemical Impedance / Raman spectroscopy of plane strain formed (φ_v = 0.25) corrosion protection primer showing a fast decrease of the impedance with time

The strong loss of barrier properties of the corrosion protection primer can only be explained by the penetration of the electrolyte into the coating and consequently the corrosive deadhesion along the binder / zinc particle interface which leads to the formation of new electrolyte pathways. Such a deadhesion is a very fast process which can reach a speed of up to 100 µm / h [161] and is thereby visible in the time scale of the experiment.

Combined Raman / EIS measurements provide complementary information about the barrier and corrosion properties of coatings and enable a comprehensive view of the system.

5.6 Modification of corrosion protection primers

5.6.1 Organo silane surface modification of zinc particles implemented in corrosion protection primers

The impedance spectra and SEM images of formed corrosion protection primers indicate the formation of defects within the forming process. These defects occur mainly at the binder / zinc particle interface. One way to reduce the amount and size of defects is to increase the adhesion force of the particle / binder interface. A surface modification of the zinc pigments with a bi-functional organo silane should increase the stability of the interface. The organo silane bonds on one side with the silane function to the oxide covered metal surface and with the organic group to the binder.

Before modification, the particles were investigated concerning their surface morphology. The FE-SEM images (Fig. 65) show a homogeneous size distribution between 2 and 6 µm. In the detailed view the pigments show differences in the surface structure. Some show a very smooth surface while others are covered by a rough, amorphous layer. This structure can lead to either a better bonding of the binder to the metal surface or to a preferred defect area if the amorphous layer breaks.

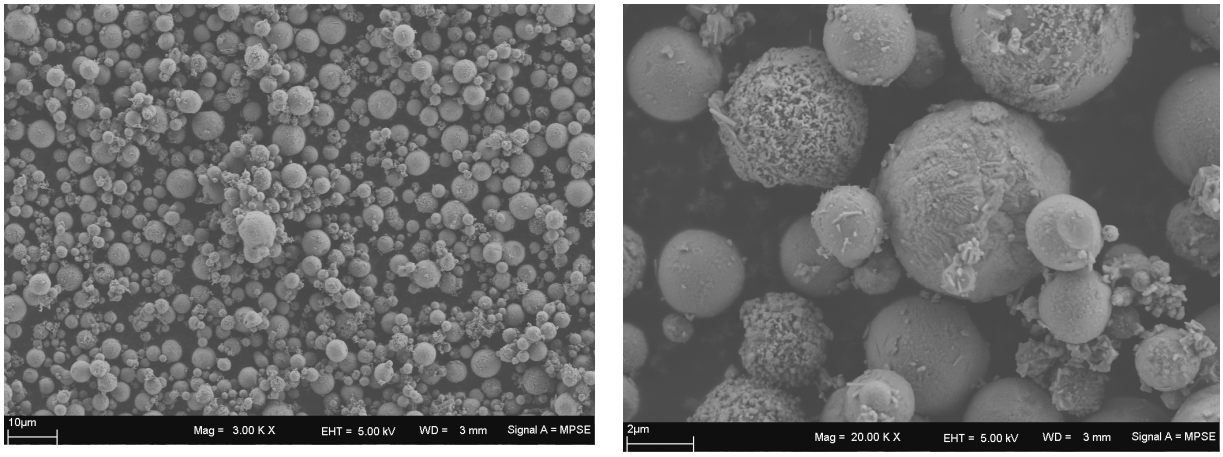

Fig. 65. FE-SEM image of zinc particles implemented into corrosion protection primers, showing a rough and amorphous layer on top

In order to reduce the influence of the porous layer the particles were cleaned for one minute with a strong alkaline cleaner before the surface modification for the reduction of the oxide scale and for the preparation of a homogeneous, fresh surface (Fig. 66).

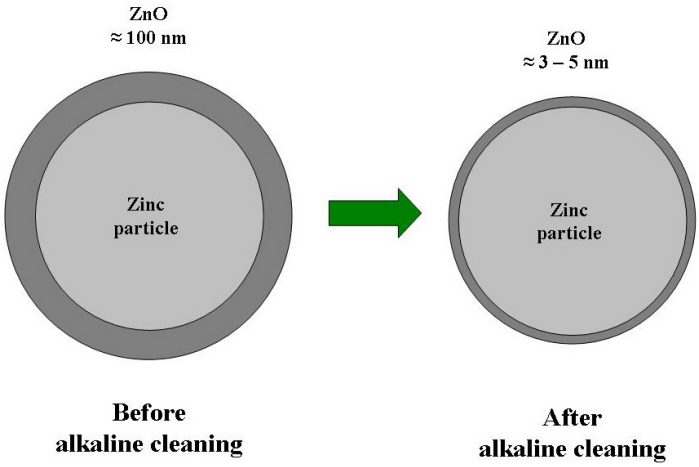

Fig. 66. Schematic drawing of the zinc oxide scale on implemented particles before and after alkaline cleaning

The FE-SEM images of the cleaned particles (Fig. 67) mainly show a much smoother surface which shows only a nano rough structure. As the alkaline solution mainly removes the zinc oxide the roughness of the particles seems to reflect the thickness of the zinc oxide layer on top.

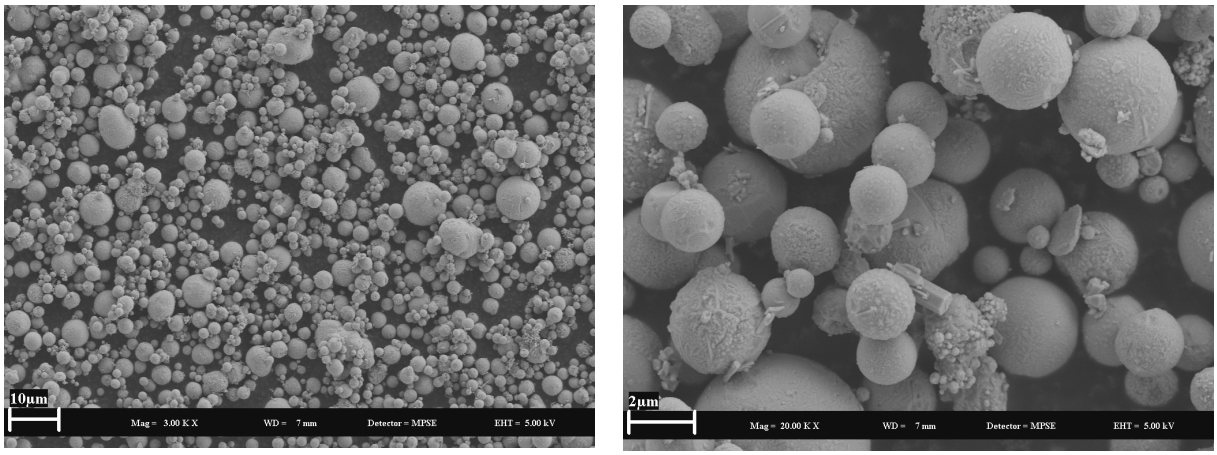

Fig. 67. Alkaline cleaned and organo silane modified zinc particles for implementation in corrosion protection primers. Most of the rough oxide film on top of the particles is removed

The particles were modified with 3-Glycidyloxypropyltrimethoxysilane (Glymo) a bi-functional organo silane. The silane part allows the bonding to a metal oxide surface [162-164] while the epoxy function can bond to the organic binder system. The Si-O function furthermore leads to the formation of a network covering the oxide surface (Fig. 68).
The pigments were immersed in a 1 % Glymo solution for 1h, afterwards rinsed with ethanol and dried at room temperature or 60 °C for 1h.

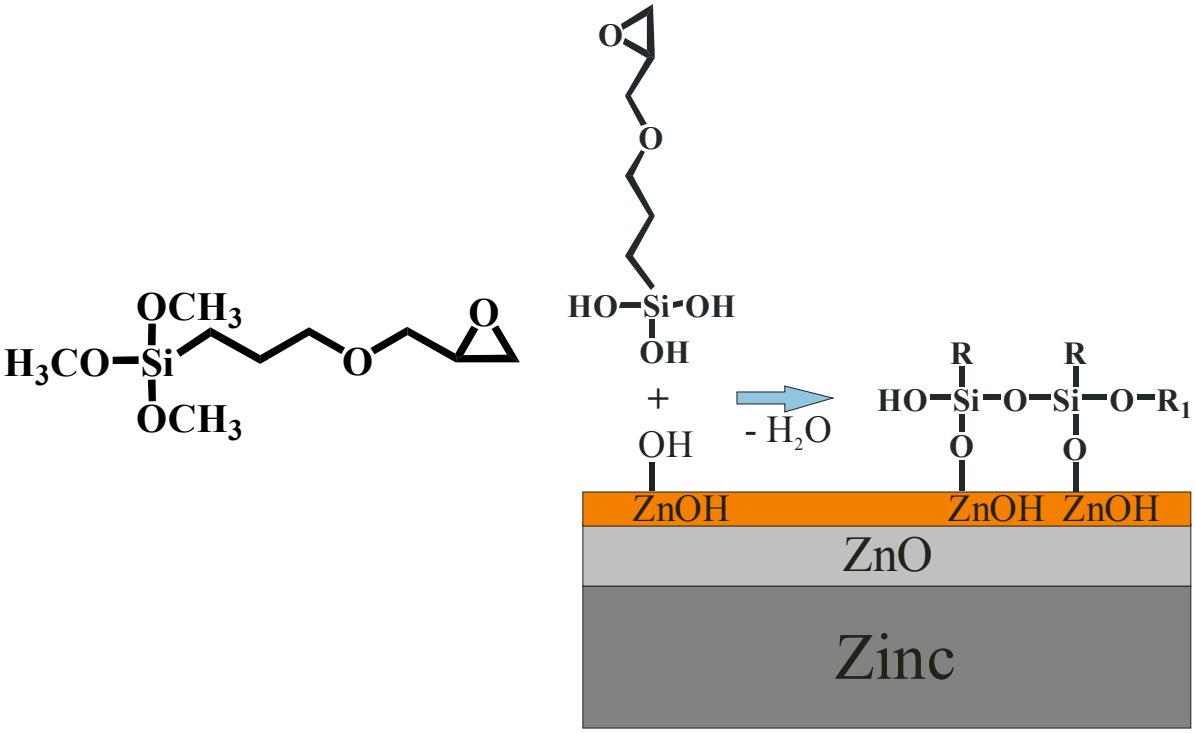

Fig. 68. Structure and network formation of 3-Glycidyloxypropyltrimethoxysilane (Glymo) on a zinc surface

The layer formation was analysed on the dried powder using DRIFT (Diffuse Reflectance Infrared Fourier Transform spectroscopy). The spectra of the modified particles dried at room temperature and 60 °C are shown in Fig. 69.

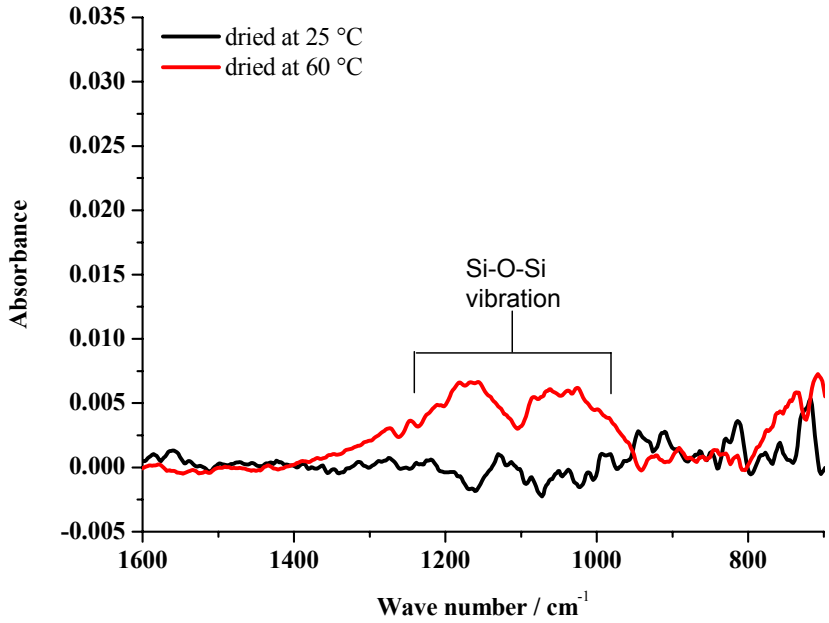

Fig. 69. FT-IR DRIFT spectra of 3-Glycidyloxypropyltrimethoxysilane (Glymo) modified zinc particles used in corrosion protection primers dried at room temperature and 60 °C. Only at 60 °C the formation of Si-O-Si bond becomes visible while the epoxy ring seems already to be opened

The RT dried layer only shows a signal of the epoxy ring at 910 cm^{-1} while the 60 °C dried layer shows the formation of Si-O-Si bond with two broad peaks at 1050 and 1200 cm^{-1}. The IR spectra reveal that the formation of a Si-O-Si network needs a curing temperature of 60 °C while at this temperature the epoxy ring already seems to open. Due to the different curing temperatures needed to get either the network formation or an intact epoxy ring the bi-functionality of Glymo is limited. Anyhow the modified particles were implemented as substitution for the unmodified zinc particles in a CPP.

5.6.2 In-Situ Electrochemical Impedance Analysis during tensile testing of a modified primer

The Glymo modified particles were used as substitute for the ordinary zinc particles in the corrosion protection primer. After application of the coating the formability was tested by means of in-situ EIS during tensile testing.

In the unformed state and for small forming degrees (≤10 % elongation), the coating with the particles dried at room temperature shows capacitively dominated behaviour above 100 Hz with a phase angle of -70 to -80° (Fig. 70). With increasing strain, the barrier properties of the

coating decrease due to the formation of cracks as indicated by the phase shift at high frequencies, reaching 0° for an equivalent strain of 0.18. At this forming degree, the measured impedance and phase values reach those of the bare zinc coated steel elongated to 25% (φ_v = 0,22). For all elongation degrees, the low frequency resistance at 0.1 Hz shows ohmic behaviour and decreases by two orders of magnitude for high strain values. The forming behaviour shows no significant differences to the unmodified coating.

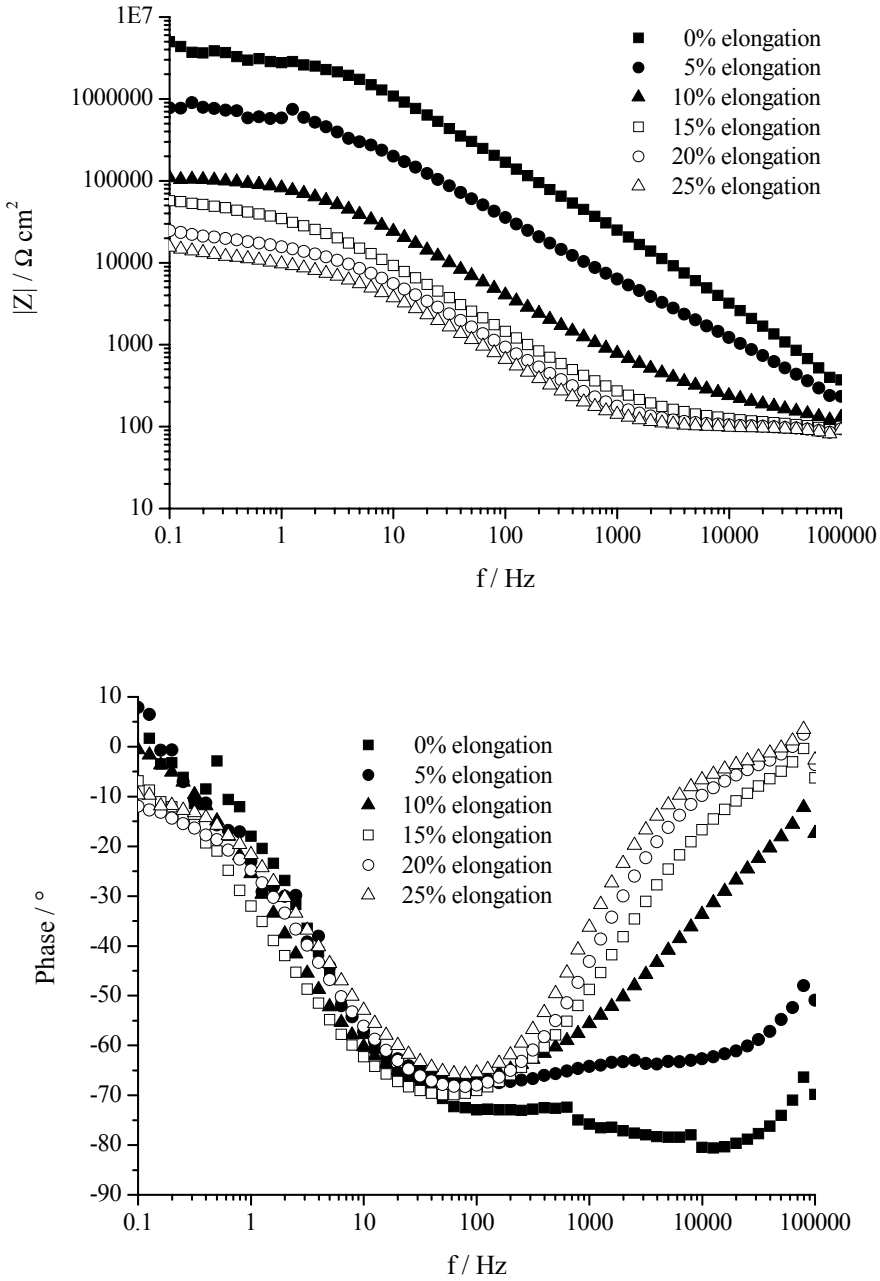

Fig. 70. In-Situ impedance spectra during forming of 3-Glycidyloxypropyltrimethoxysilane (Glymo) (dried at room temperature) modified corrosion protections primers, showing a fast reduction of the barrier properties with increasing strain

The coating with particles dried at 60 °C shows a similar behaviour as with the particles dried at room temperature (Fig. 71). In the forming state between 0 and 10% the impedance above 100 Hz is capacitively dominated by a phase shift of -70 to -80°. With increasing strain the coating shows crack formation indicated by the decrease of the phase angle shift to 0° in the high frequency range and a strong drop of the ohmic resistance at low frequencies. Again at high forming degrees the impedance spectrum of the blank steel substrate is measured and the coating shows nearly no more protective properties.

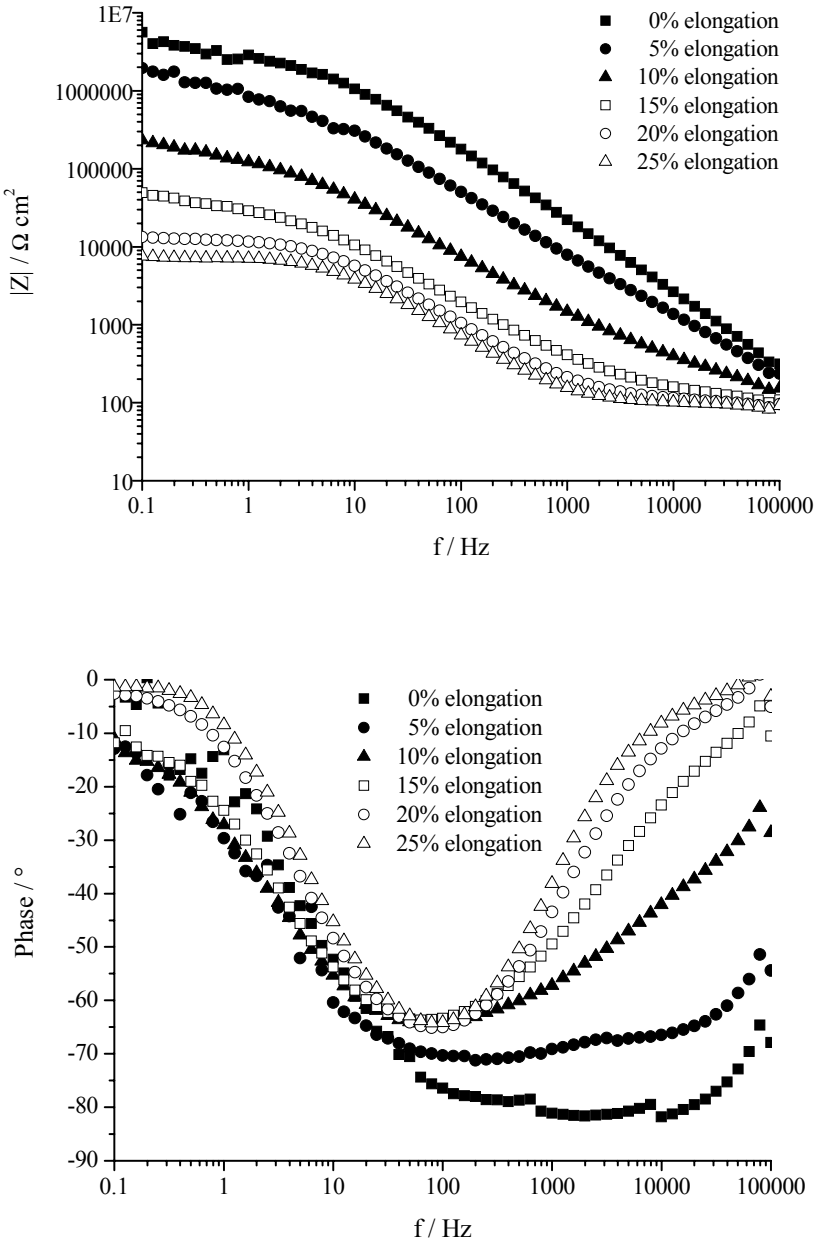

Fig. 71. In-Situ impedance spectra during forming of 3-Glycidyloxypropyltrimethoxysilane (Glymo) (dried at 60°C / 1h) modified corrosion protections primers, showing similar behaviour to the one with particle dried at RT a fast reduction of the barrier properties with increasing strain

The formed samples were further investigated by means of FE-SEM to follow the crack formation at different elongation steps. The images (Fig. 72) show the formation of initial small cracks in the range of some nm already at 5 % stretching. With increasing strain the crack size and amount rise with cracks of up to 5 µm. The defects mainly occur at the interface zinc particle / binder similar to the unmodified coating. The interface is obviously still the weakest part of the system and cannot withstand the force applied to the coating by the uniaxial forming procedure.

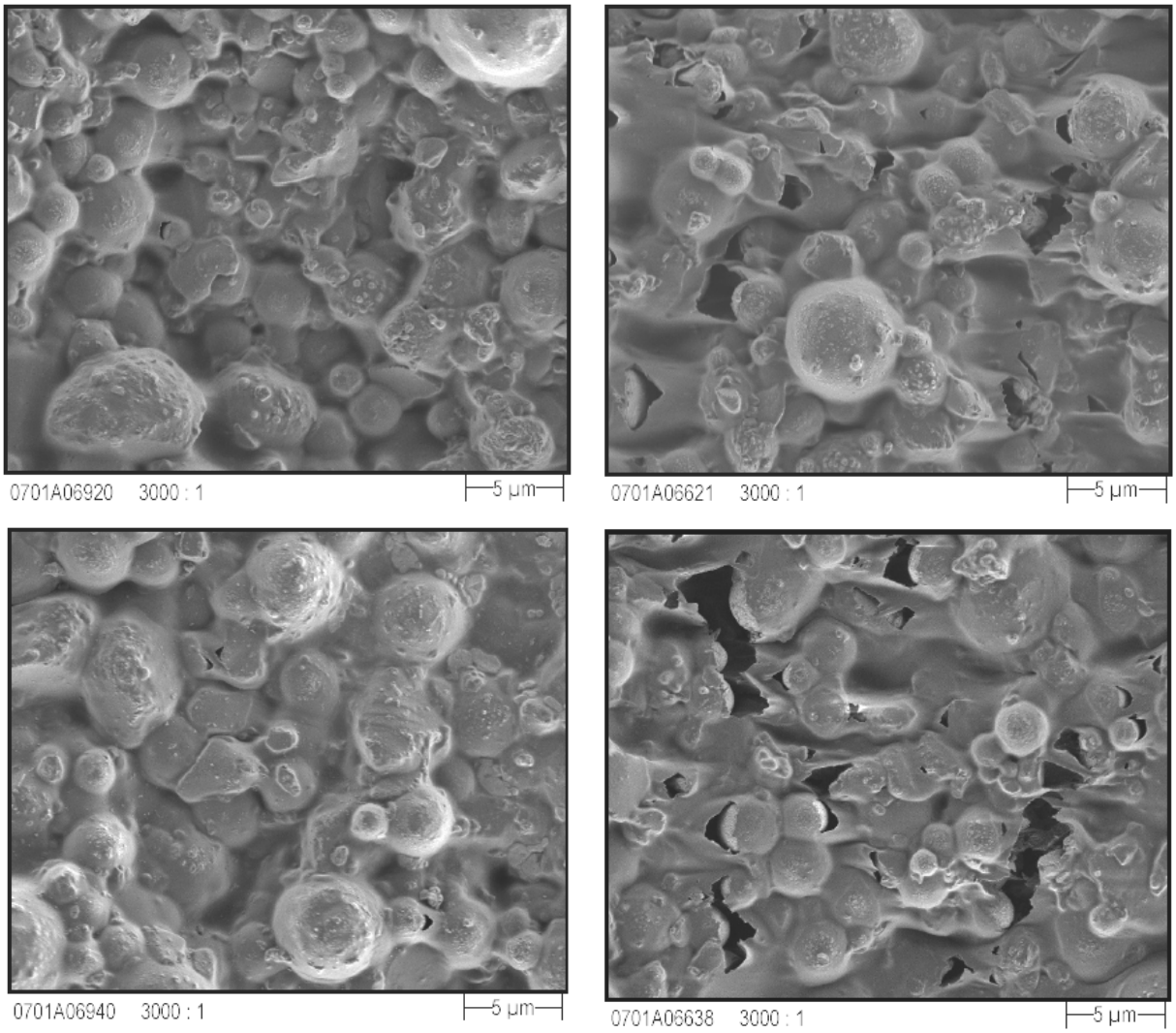

Fig. 72. SEM images of formed corrosion protection primers with 3-Glycidyloxypropyltrimethoxysilane (Glymo) modified particles (organo silane dried at room temperature on top and at 60°C for 1h on the bottom, 5% elongation left and 20% elongation right). A similar crack formation for both modified particles is visible

For a better comparison between the coatings and in order to avoid mistakes from the scattering of measurement points the impedance spectra for each elongation step were fitted by a polynomial curve. Afterwards the low frequency (ohmic) resistance was calculated from the fit and is plotted in Tab. 5.

Tab. 5. Resistance at 0.1 Hz taken from non-linear impedance fit

	CCP in borate buffer / Ω cm²	**CCP in NaCl / Ω cm²**	**Modified CPP (Particles dried at RT) in borate buffer / Ω cm²**	**Modified CPP (Particles dried at 60 °C) in borate buffer / Ω cm²**
0 % elongation	2211210	100168	4096909	4102455
5 % elongation	1169940	18568	826994	1653030
10 % elongation	247783	5032	104900	206309
15 % elongation	75052	859	53916	44212
20 % elongation	34793	447	22611	12801
25 % elongation	20096	273	14095	7261

The resistances calculated for the different forming steps are plotted in Fig. 73 versus the different elongation steps. The direct comparison of the modified and unmodified coatings show a slight increase of the barrier properties for the modified coatings at small elongations due to the higher coating thickness (5µm instead of 3.5µm).

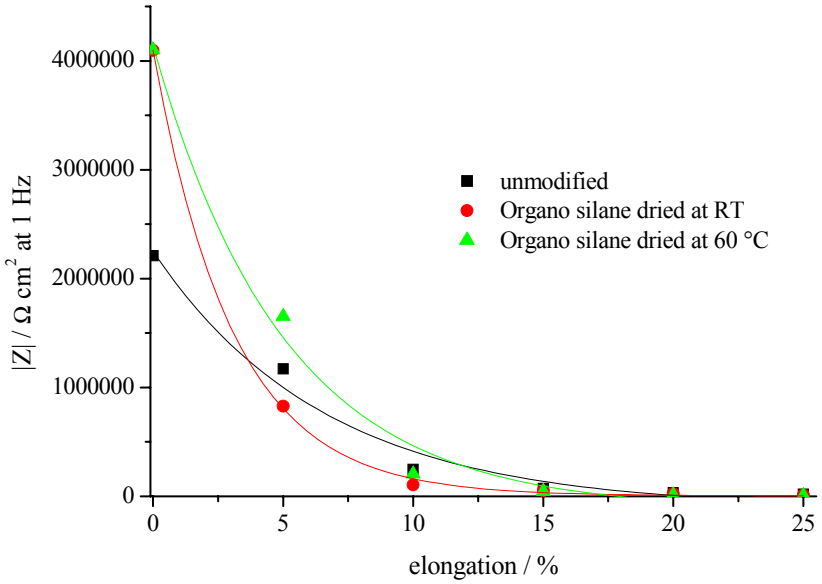

Fig. 73. Comparison of corrosion protection primers with organo silane modified and unmodified zinc pigments

The primer shows with particles dried at 60 °C a slightly better performance as the one dried at room temperature. The differences between the modified coatings indicate that the formation of a Si-O-Si network is of great importance for the performance of the organo silane at the particle / binder interface while the reaction of the epoxy ring shows no visible influence on the impedance spectra. The performance loss between the unmodified and the modified CPP at elongations ≥5 % can be traced back to the fact that the cleaning procedure leads to a much smoother surface of the particles and thereby to a worse connection between the particle and the binder. Even the interface stabilisation by the particle modification can not equalise this disadvantage.

5.7 Corrosion model of formed and unformed corrosion protection primers

The impedance spectra of formed and unformed CPP in NaCl electrolyte show a fast degradation of the coating barrier properties. This can be caused by the corrosive deadhesion along the particle / binder interface which is a very fast process [161]. These new pathways allow the electrolyte to penetrate the coating and thereby reduce the resistance and the corrosion protection properties.

In the case of formed CPP the major loss of the corrosion protection results from forming-induced defects that open new penetration ways for the electrolyte. Further on the coating detaches from the electrogalvanised steel substrate underneath, which leads to the formation of small caverns. These caverns act as initial sites for corrosive deadhesion along the binder / zinc layer interface and lead thereby due to the oxygen reduction to a local, alkaline pH shift (Fig. 74). Furthermore the coupling of defects leads to separated defects that act as anode and cathode and can thereby also reduce the local pH value.

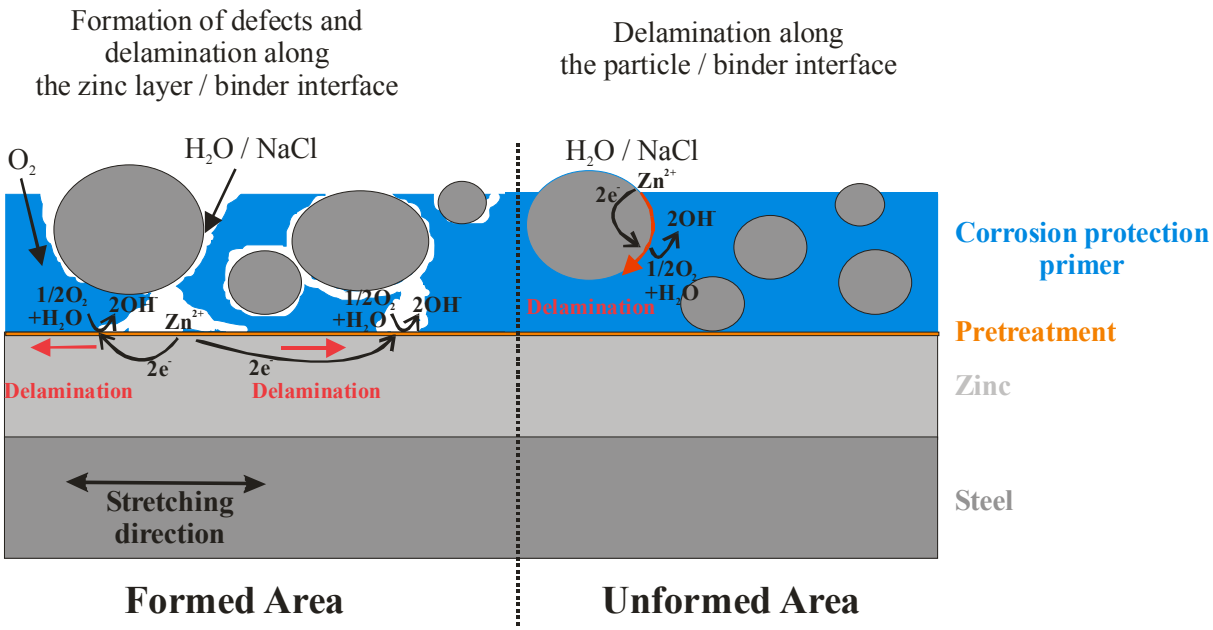

Fig. 74. Model of the corrosion process occurring at formed and unformed corrosion protection primers. In formed areas the defects act as initial corrosion sites and lead to a fast delamination and corrosion at the binder / zinc interface. In the unformed state a fast delamination along the particle / binder interface occurs which leads to new conductive pathways through the coating

This is also visible by the strong etching attack of the phosphate crystals which are not stable in alkaline and acidic solutions. The shift in the pH accelerates local corrosion of the zinc layer as the formation of protective precipitation layers is not possible [159, 160]. The

Pourbaix diagram shows that at high pH-values (> pH 11) the formation of soluble zincate or bizincate becomes possible while at low pH-values the formation of Zn^{2+} occurs (Fig. 75).

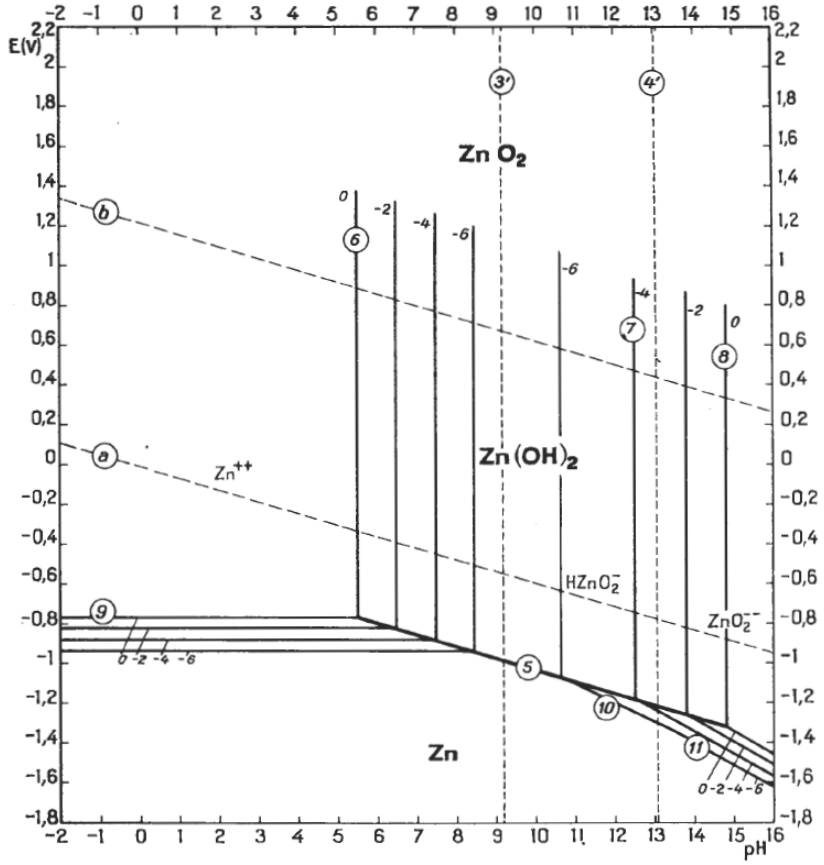

Fig. 75. Theoretical conditions of corrosion, immunity and passivation of zinc (taken from [160])

In chloride containing electrolytes as used for the salt spray testing the formation of insoluble Simonekolleite ($Zn_5Cl_2(OH)_8 \cdot H_2O$) is possible at intermediate pH and high Cl^- concentrations according to eq. 43 [165, 166]. These would form a passivating precipitation layer which reduces the corrosive attack.

$$5\ Zn^{2+} + H_2O + 8\ OH^- + 2\ Cl^- \rightarrow Zn_5Cl_2(OH)_8 \cdot H_2O \qquad \textbf{(eq. 43)}$$

At high or low pH or at low Cl^- concentrations the $Zn_5Cl_2(OH)_8 \cdot H_2O$ becomes unstable and dissolves under the release of chloride (Fig. 76). In case of the caverns that act as cathode the high pH due to oxygen reduction and the reduced OH^- diffusion leads to the formation of ZnO or zincate. In the caverns acting as anodic sites the diffusion of chloride into them is hindered and thereby falls below the critical concentration necessary for the formation of Simonkolleite. In both cases the formation of passivating layers is not possible.

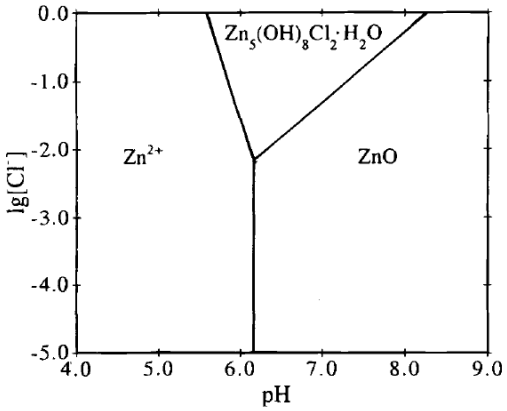

Fig. 76 Stability diagram of simonkolleite in aerated solutions with varying pH and Zn^{2+} concentration of 0.1 M at 25 °C (taken from [165])

The high corrosion rate is visualised by the strong local corrosion found already after 24 hours of salt spray testing in the FE-SEM cross section. Furthermore, the FIB cross sections show a fast dissolution of the zinc layer and precipitation layers of corrosion products only on top of the CPP where the OH^- concentration is lowered by the exchange of the electrolyte.

5.8 In-situ QCM / Raman investigations of the inhibitor adsorption on metals

Organic and inorganic inhibitors are widely used to improve the protective properties of organic coatings. Inhibitors can act either by the formation of barrier layers on top of the surface or by precipitation of low soluble products. In both cases the detection of corrosion and precipitation products, the kinetic of the inhibiting effect and the concentration dependence are of great interest. The newly developed in-situ QCM / Raman cell allows the simultaneous detection of the frequency change of a sample which is caused by a dissolving or precipitation reaction and the measurement of the Surface Enhanced Raman Spectrum of the sample (see 4.3). In this case the adsorption of the inhibitor Mercaptobenzothiazol (MBT) onto a silver and a gold sample was studied as a model system but the method can be expanded to all SERS active substrates.

5.8.1 Ex-situ SERS analysis of Mercaptobenzothiazol (MBT) adsorption

Prior to the in-situ experiments the spectral properties of Mercaptobenzothiazol (MBT) were investigated ex-situ. First tests on a flat non-SERS active silver substrate immersed in an MBT / ethanol solution showed no measurable peaks. In Fig. 77 the powder spectrum and the spectrum of a SERS active silver sample after immersion into a 10^{-3} M MBT / ethanol solution are shown. Nearly all peaks that are found in the powder spectrum are also present in the SERS spectrum, mainly with slight changes in the peak position and intensity. The most significant peak at 1254 cm^{-1} in the spectrum b) strongly decreases in intensity in the SERS spectrum while the one at 1395 cm^{-1} shows a strong increase. Further differences are the peaks of the benzene ring at 397 cm^{-1}, 1076 cm^{-1} and 3070 cm^{-1} which show much higher intensities in the powder spectrum than in the SERS spectrum. This might be a consequence of the preferred orientation of the MBT molecule during the adsorption. Known from literature is that the non-cyclic sulphur atom bond to the sample which leads to a perpendicular orientation of the molecule to the surface and can thereby lead to a reduction of the Raman absorption of the benzene bonds. In contrast to that the powder displays a random distribution of molecule orientations.

In Tab. 6 the peak positions and assignment of the powder and SERS spectrum are given.

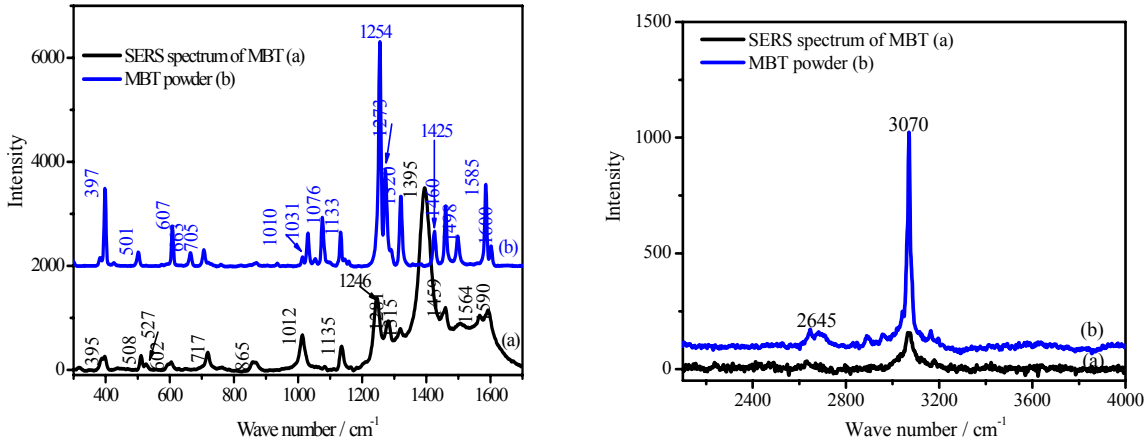

Fig. 77 Ex-situ SERS spectrum of (a) MBT adsorbed on the quartz crystal-based SERS-active substrates and (b) normal Raman spectrum of MBT powder, showing the amplification of the spectrum by the change of the substrate structure

Tab. 6. Assignments of the Raman peaks of MBT powder and MBT adsorbed on quartz crystal-based SERS-active substrates

Peak position /cm^{-1}		Assignment
Powder	**SERS**	
3070	3070	CH stretching in Bz ring
2645		SH stretching
1600	1590	Bz ring stretching
1585	1564	Bz ring in plane stretching
1498		N-C=S stretching
1460	1459	C-C stretching
1425	1395	NCS ring stretching
1320	1315	NH bending
1273	1281	CH in-plane bending
1254	1246	CH bending or CN stretching
1133	1135	CH in-plane bending
1076		Bz ring or SCS antisymmetric stretching
1031		CH in-plane deformation
1011	1013	C-C-C bending
	867	CH out-of-plane bending
705	717	C-S stretching
663		NH deformation
607	602	CS stretching in heterocyclic ring system
	527	Bz ring deformation
501	508	Bz ring deformation
397	396	Bz ring deformation

5.8.2 Combined in-situ Raman / QCM measurement of the adsorption of MBT on silver

The in-situ MBT adsorption study started with a reference measurement of pure ethanol running through the setup (first spectrum in Fig. 78). After the system reached the equilibrium the injection of MBT happened and spectra were taken every 10s in the initial state. The pumping and tube system lead to a delay of nearly 40s before the first MBT reaches the sample and forms a peak at 1395 cm^{-1} (Fig. 78). With an increasing measurement period the intensity of the peak rises and new peaks at 396, 717, 1315, 1564 and 1593 cm^{-1} appeared.

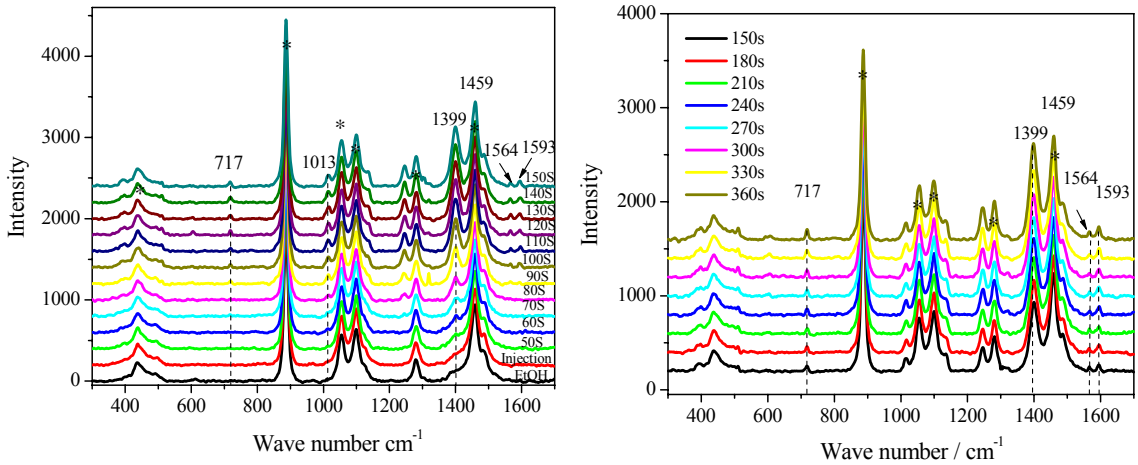

(a) 0-100 seconds (b) 100-240 seconds

Fig. 78. In-situ SERS spectra of adsorbed MBT as a function of adsorption time: (a) from the beginning to 100 s with an interval of 10 s; (b) from 100 to 240 s with an interval of 30 s. The spectra show an increase of absorbed MBT with time

The intensity of a Raman peak is proportional to the number of molecules illuminated by the laser and thereby reflects the amount of molecules adsorbed to the SERS substrate. Hence the peak at 1395 cm^{-1} was chosen for the MBT adsorption and the ethanol peak at 887 cm^{-1} as reference for controlling the focus of the system.

The intensity shows after the initial delay of about 1 min a strong increase which takes nearly 2 min until it passes over to a plateau value for longer times (Fig. 79). The ethanol peak stays nearly constant over the whole experiment, indicating a focused sample and a uniform laser power.

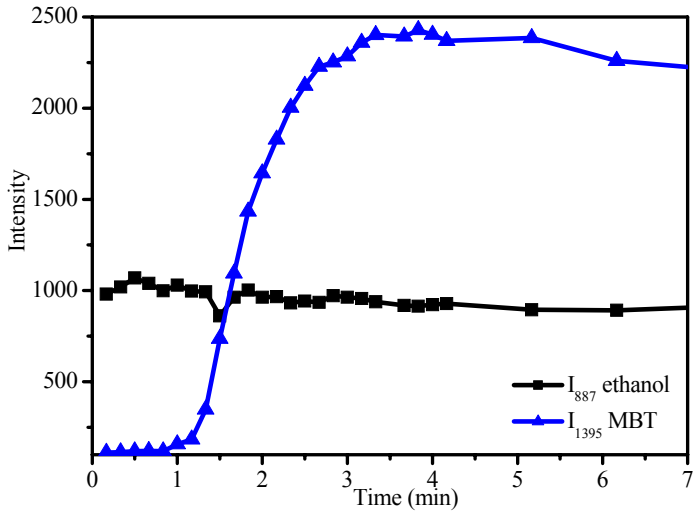

Fig. 79. Evolution of Raman intensity of ethanol and MBT adsorbed on SERS-active silver as a function of time, indicating a constant signal for the ethanol while the MBT signal rises for some minutes until it reaches a plateau value

The combined plotting of the Raman and QCM data (Fig. 80) shows a similar delay before the MBT adsorption starts. In the beginning both show a steep slope with a change after about one minute. In the case of the Raman measurement the turning point indicates the change for reaching the final plateau while for the QCM measurement the linear decrease just gets a different slope and further decreases linearly.

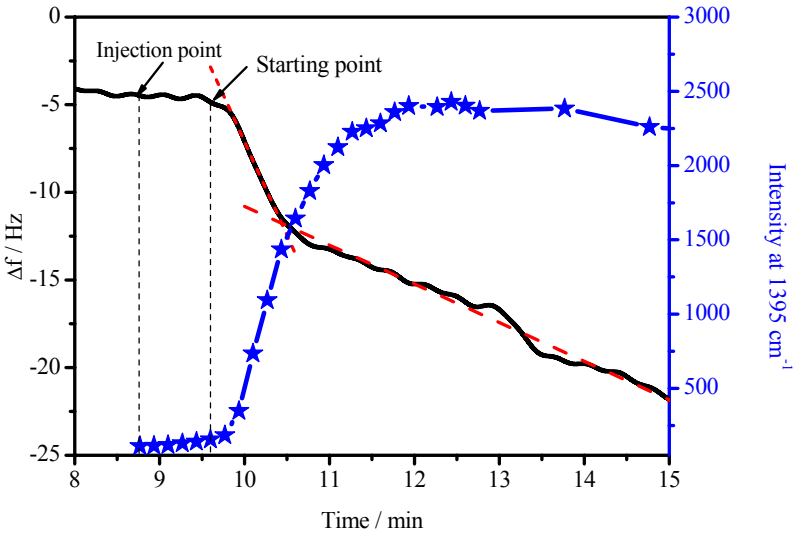

Fig. 80. In-situ QCM / Raman measurement of MBT adsorption on SERS-active silver. The Raman signal reaches a plateau value after a few minutes while the QCM signal decreases further due to the ageing effects of the silver substrate

As the frequency shift in the QCM measurement continued even after the Raman intensity became constant the data acquisition was continued until a plateau value was also observed (Fig. 81). The frequency shift became constant after nearly 48 hours with a final value of -200 Hz.

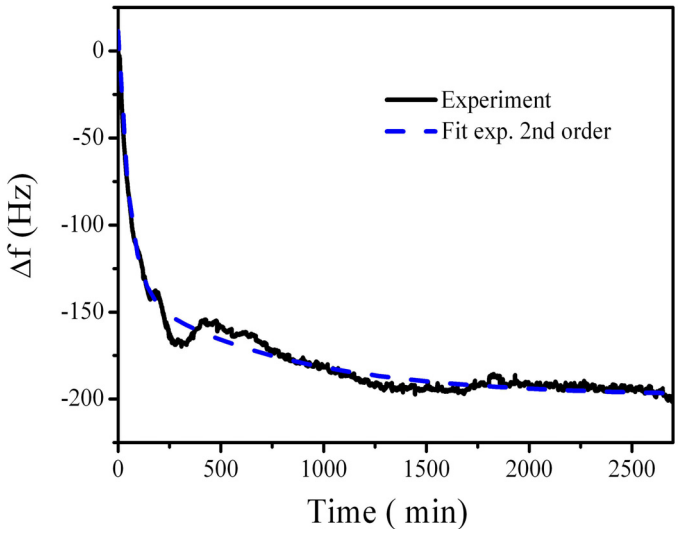

Fig. 81. Long time QCM experiment of the MBT absorption on SERS-active silver to investigate the maximum frequency shift. After about 24 hours the systems become stable with a frequency shift of about 200 Hz

The long adsorption time indicated by the QCM experiment is contrasts with the Raman data and the calculation for the frequency shift of a monolayer of MBT (see 5.8.4). The strong decrease might occur by some ageing effects that occur on the silver surface in the ethanol / MBT solution.

5.8.3 Combined in-situ Raman / QCM measurement of the adsorption of MBT on gold

The adsorption of MBT on a silver layer shows discrepancies between the Raman and the QCM data which might arise from aeging effects of the silver surface. These effects could be avoided by using gold as SERS substrate. Therefore gold SERS active samples were prepared in the same manner as the silver ones.

The SERS spectra of MBT on a silver and gold based sample are compared in Fig. 82. Both spectra show similar peak formations of the adsorbed MBT which allows to analyse the gold spectrum in a similar way as already undertaken with the silver based one.

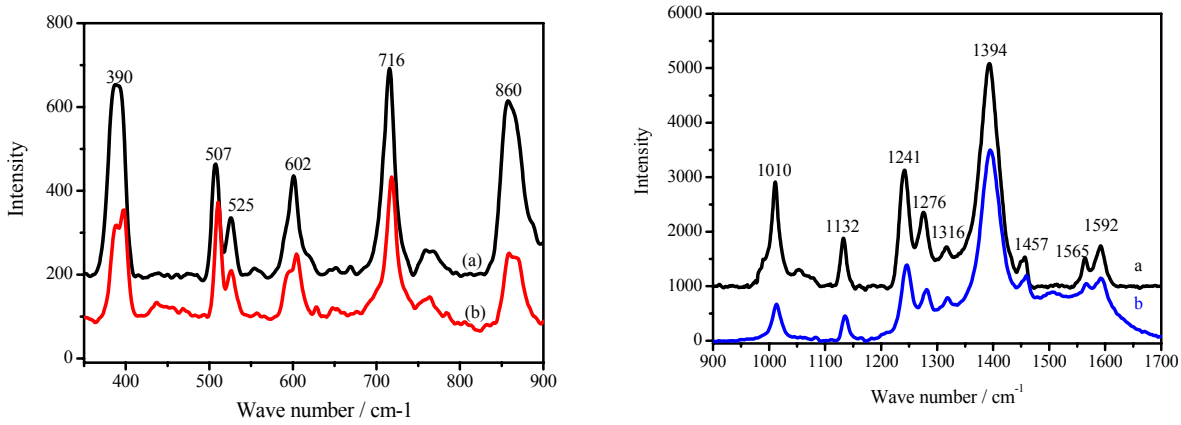

Fig. 82. Spectra of MBT adsorbed on SERS-active gold (a) and on silver (b). Both substrates show a strong amplification of the characteristic peaks

During the in-situ experiment the Raman signal at 1395 cm^{-1} (MBT) again showed a delay of a few seconds before the MBT solution reached the cell (Fig. 83). Then a strong increase of the peak intensity for about 6 minutes took place. Finally the intensity reached a constant plateau value. Also in this experiment the ethanol reference value stayed constant over the complete measurement time. The adsorption kinetic is in the case of gold three times slower as on silver where the plateau value is reached after 2 minutes.

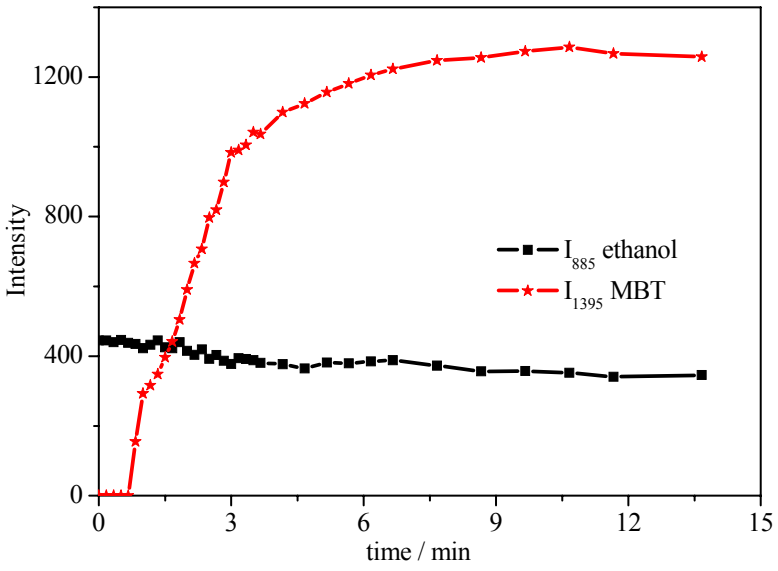

Fig. 83. Evolution of Raman intensity of ethanol and MBT adsorbed on SERS-active gold as a function of time, indicating a constant signal for the ethanol while the MBT concentration grows for some minutes until it reaches a plateau value

The combined QCM and Raman data show in the case of gold a consistent behaviour with an inverted slope of the two curves, indicating that both analytical tools enable the correct identification of the kinetic of the adsorption process (Fig. 84). In contrast to the silver experiment also the QCM data show a plateau after 6 minutes at about -10 Hz indicating that no further reactions on the gold surface take place. As already mentioned the gold based experiment shows a three times slower rate of the MBT adsorption than for silver which might be due to a different adsorption mechanism on gold surfaces which was already discussed in the literature [167].

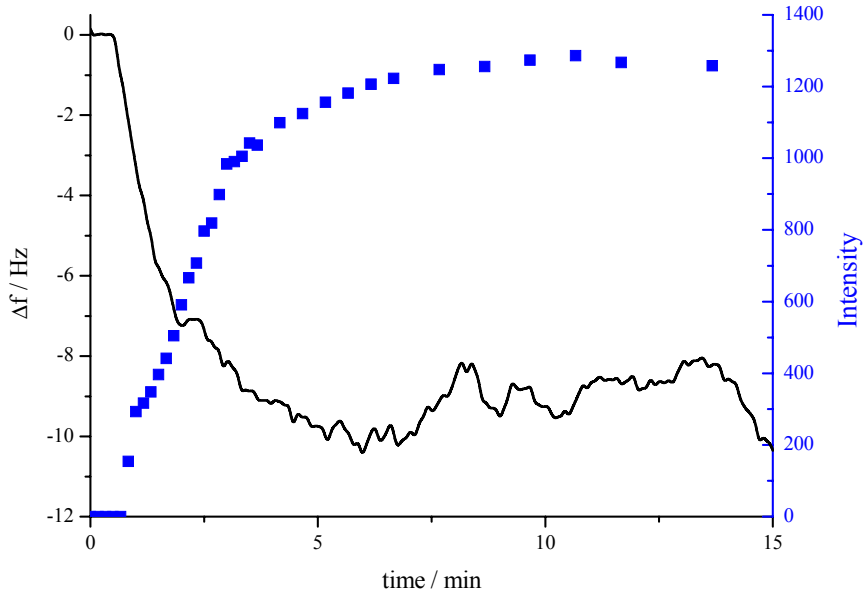

Fig. 84. In-situ QCM / Raman measurement of MBT adsorption on SERS-active gold. Both signals reach a plateau value after a few minutes and show a consistent curve progression

A comparison of the gold and silver based SERS active surfaces shows for the adsorption kinetics measured by Raman spectroscopy comparable results, while the QCM data completely differ. The QCM measurement gives integral information for the mass change of the surface while the selected Raman peak is sensitive to the adsorption of the MBT. It seems that the contact of the silver surface with the MBT solution leads to further changes of the SERS substrate which are not detected by the Raman measurement. Therefore the optimal substrate for an in-situ investigation is a gold coated quartz.

5.8.4 Theoretical calculation of the frequency shift by a monolayer

It is known from literature that Mercaptobenzothiazol forms a monolayer during the adsorption process on the substrate. The frequency shift of a monolayer can be calculated theoretically and compared to the experimental data of the adsorption on silver and gold.

For the calculation of the frequency shift the amount of molecules that adsorb per cm^2 is necessary which can be calculated from the three dimensions of the MBT molecule. The ideal molecule structure was simulated with Gaussian [168] and is shown in Fig. 85 indicating a completely flat structure.

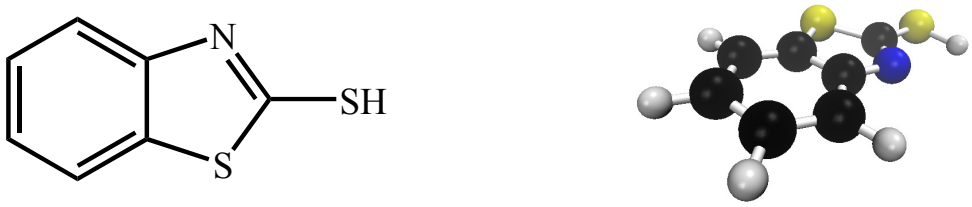

Fig. 85. Chemical and 3D structures (simulated with Gaussian) of Mercaptobenzothiazol indicating MBT as a planar molecule

The length, width and height of the molecule were calculated to be l = 7.6 Å, w = 5.0 Å and h = 2.0 Å. These dimensions can be used to describe the MBT molecule as a brick which can either adsorb with the front face (A_1), the long side (A_2) or planar (A_3) on the sample surface (Fig. 86). The different orientations of the adsorbed molecule lead to a different mass load on the surface and thereby to differences in the frequency shift.

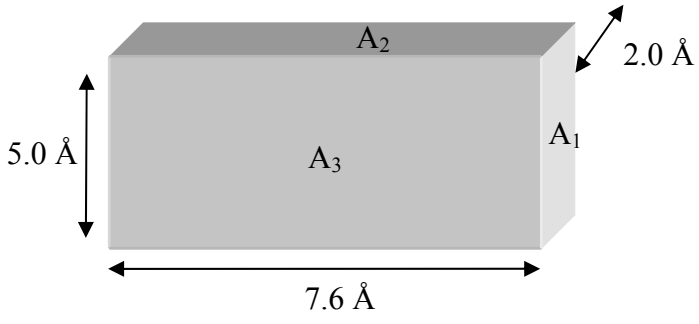

Fig. 86. Schematic drawing of the MBT adsorption planes taken from the 3D simulation

The covered surface areas for the different absorption orientations were calculated to be:

$$A_1 = w \cdot h = 5 \cdot 10^{-10}\, m \cdot 2 \cdot 10^{-10}\, m = 10 \cdot 10^{-20}\, m^2 = 1 \cdot 10^{-15}\, cm^2 \qquad \textbf{(eq. 44)}$$

$$A_2 = l \cdot h = 1.52 \cdot 10^{-15}\, cm^2 \quad \textbf{(eq. 45)}$$

$$A_3 = w \cdot l = 3.8 \cdot 10^{-15}\, cm^2 \quad \textbf{(eq. 46)}$$

With the assumption that the molecules adsorb in a closed package without any free volume the number of molecules and with the Avogadro constant ($6.022 \cdot 10^{23}$ molecules / mol) and the molar mass of MBT (167.24 g / mol) the mass for a monolayer per cm^2 can be calculated (done here exemplarily for orientation A_1) :

Number of molecules per cm²:

$$N_1 = \frac{1}{A_1} = 1 \cdot 10^{15}\, \frac{molecules}{cm^2} \quad \textbf{(eq. 47)}$$

Mol per cm²:

$$n_1 = \frac{N_1}{6.022 \cdot 10^{23}\, \frac{molecules}{mol}} = 1.66 \cdot 10^{-9}\, \frac{mol}{cm^2} \quad \textbf{(eq. 48)}$$

Mass per cm²:

$$m_1 = n_1 \cdot M_{MBT} = 1.66 \cdot 10^{-9}\, \frac{mol}{cm^2} \cdot 167.24 \frac{g}{mol} = 277 \frac{ng}{cm^2} \quad \textbf{(eq. 49)}$$

Sauerbrey [121] shows that the frequency change of the QCM is proportional to the mass load change of the quartz crystal. Using this equation with the known mass change for a monolayer MBT and the proportional factor c_f for the used quartz crystal allows the calculation of the theoretical frequency change for the different orientations (A_1, A_2 and A_3).

$$\Delta f = -c_f \cdot \Delta m \quad \textbf{(eq. 29)}$$

$$c_f = -0{,}056 \frac{Hz \cdot cm^2}{ng} \quad \textbf{(eq. 50)}$$

$$\Delta f_{A_1} = -0.056 \frac{Hz \cdot cm^2}{ng} \cdot 277 \frac{ng}{cm^2} = -15{,}5 Hz \quad \textbf{(eq. 51)}$$

$$\Delta f_{A_2} = -10.3 Hz \quad \textbf{(eq. 52)}$$

$$\Delta f_{A_3} = -4.04 Hz \quad \textbf{(eq. 53)}$$

This calculation shows that the frequency change of a monolayer MBT is found for the gold substrate in the range of the experimental data. The orientation A_2 already discussed in literature [167] as the preferred adsorption orientation comes close to the measured value. The results show that the frequency shift found for the adsorption on silver with about 200 Hz has to be influenced by parallel processes which were already indicated by the slope change observed after a few seconds.

5.9 Forming and water uptake of polyelectrolyte layers

5.9.1 Molecular composition of polyelectrolytes

Polyelectrolytes are polymers with ionisable groups that can dissociate in a polar solvent to be either positively or negatively charged. Due to the mixture of oppositely charged polymers the formation of networks connected by coulomb forces between the dissociated groups is possible. This allows a layer by layer formation of polymers which can attach to a charged sample surface. Due to the non-covalent bonding between the groups highly flexible layer systems are formed. In the case of e.g. carboxylic and amino groups they can be transferred by heating into covalent bonded systems [36, 169]. The layer formation of oppositely charged polyelectrolytes with carbonyl and amine functions before heating is schematically given in Fig. 87.

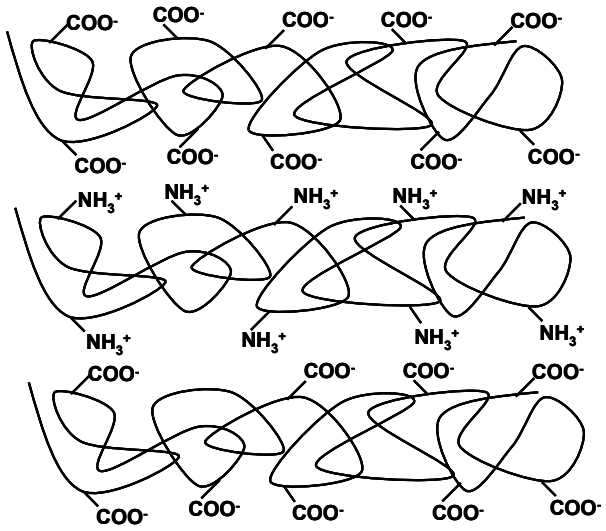

Fig. 87. Schematic drawing or the layer formation of oppositely charged polyelectrolytes by coulomb forces

Equation 54 shows the amidation reaction of the carboxylate and ammonium function.

$$R\text{-}NH_3^+ + R\text{-}COO^- \rightarrow R\text{-}NH\text{-}CO\text{-}R + H_2O \qquad \textbf{(eq. 54)}$$

For the further forming investigations especially by Wolfgang Bremser and Oliver Seewald (University of Paderborn) synthesised polyelectrolytes were used. They consisted of the functional groups already mentioned above. The schematic composition of the molecules is

given in Fig. 88. In contrast to the commonly used layer by layer formation the two components were already mixed during application.

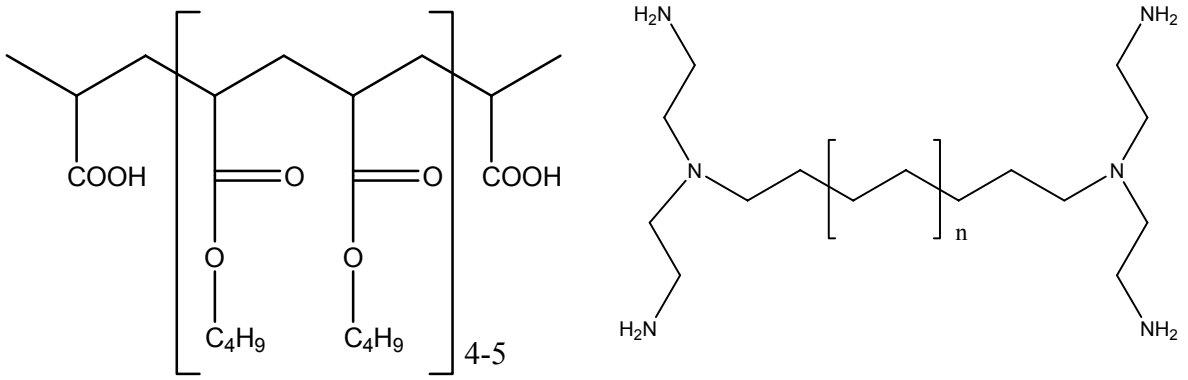

Fig. 88. Schematic drawing of the polyelectrolytes (polyanion left and polycation right) used for forming experiments

The amount of polycation groups (amine functions) was thus chosen twice as high as the number of polyanion groups (carboxylic functions), Butlyglycol and Methylisobutylketon were used as solvent. The layers were applied on electrogalvanised steel by dip-coating and afterwards dried at room temperature, 130 °C and 230°C for 2h using standard or nitrogen (N_2 stream) atmosphere.

5.9.2 FT-IR analysis of the curing state of polyelectrolyte layers

The influence of different temperatures and the storing of the coated samples on the curing state were monitored by Infrared Attenuated Total Reflection spectroscopy (ATR). Furthermore, the effect of modified atmospheres on the coating properties was studied. First of all, a freshly prepared PET sample which was dried for 24h at room temperature was compared to the solvent spectra (Fig. 89). The spectra indicate that already after 24h hours of drying most of the solvent is evaporated which is furthermore indicated by a coating, that is no longer sticky. The PET system shows characteristic peaks at 830 (C-O), 1037 (C-O), 1180 (C-O), 1246 (-O-H), 1458 (C-H), 1508 ($-NH_3^+$), 1730 (C=O), from 2872 – 2958 (CH_2 and CH_3) and from 3080 – 3900 cm^{-1} (-OH).

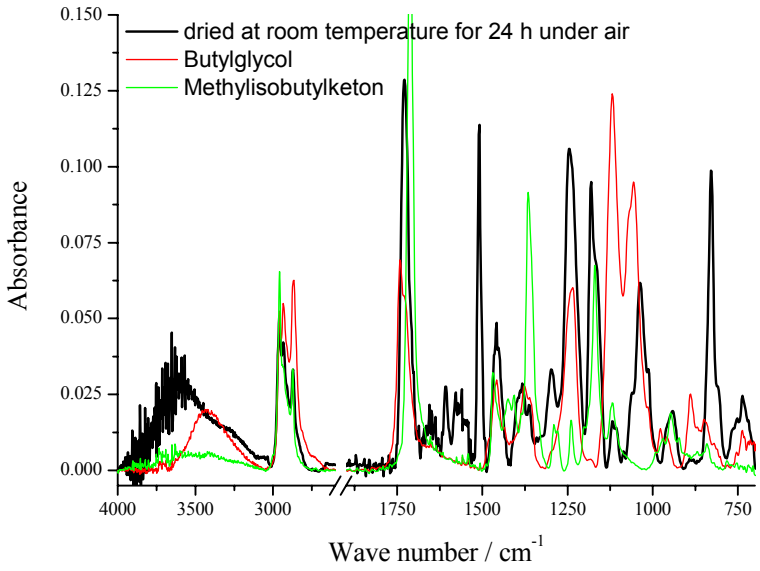

Fig. 89. Comparison of freshly prepared PET complex dried at room temperature for 24 hours vs. the used solvents (Butylglycol and Methylisobutylketon). The spectra show the nearly complete removal of the solvents after 24 hours

The spectra of PET films dried at room temperature for 24 hours and 30 days were compared with respect to their curing states. Both coatings showed the characteristic peaks already mentioned before. Furthermore, the coatings which were dried for 30 days showed the formation of new peaks at 1419 (N-H stretching), 1577 and 1604 cm^{-1} (amide peaks) (Fig. 90). This indicates that the cross linking reaction between the anionic and cathodic groups took already place after the evaporation of the solvent and doesn't necessarily need a thermal step.

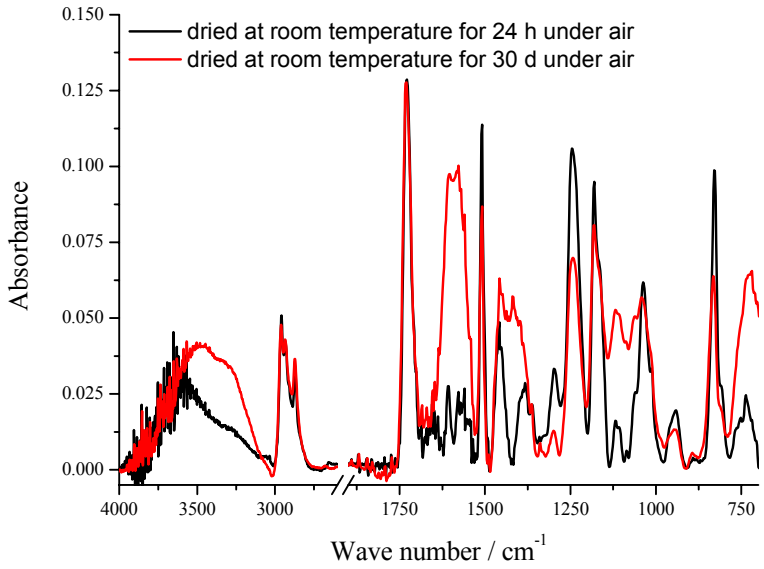

Fig. 90. Comparison of PET films dried at room temperature for 24 hours and for 30 days. The spectra show the formation of amide bonds after 20 days of storage

The coatings dried at room temperature, 130 °C and 230 °C show all the characteristic peaks of the PET complex (Fig. 91). Additional peaks appear for the two coatings cured at higher temperatures which show the formation of amide bonds. With increasing temperature also this peak intensity increases indicating a higher cross linking of the applied film. It seems that at high temperatures of 230 °C the coatings degrade by a saponification according to eq. 54 and leads to more reactive groups.

$$R_1\text{-}COOR_2 + H_2O \rightarrow R_1\text{-}COOH + R_2\text{-}OH \qquad \textbf{(eq. 55)}$$

This is visible by the further increase of the amide peak which needs more carboxylate groups to form amid bond. The necessary water for the reaction can be provided either from humidity or from the water formed by the amide formation.

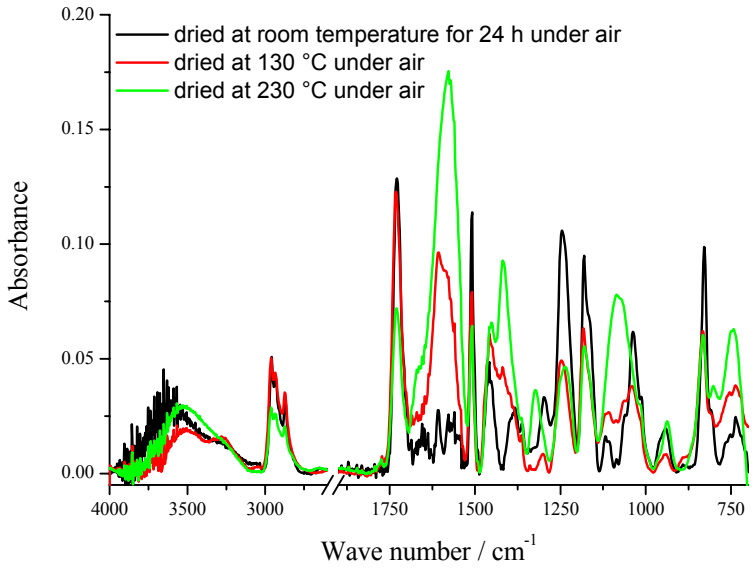

Fig. 91. Comparison of polyelectrolyte coated samples dried at different temperatures. Rising curing temperature leads to an increase in the number of amide bonds

For the film preparation it is of great interest if the curing under standard atmosphere leads to a degradation of the applied coating. Fig. 92 and Fig. 93 show the comparison of films cured at 130 °C and 230 °C under air or nitrogen atmosphere. For the medium temperature the coatings show no difference in peak formation and thereby no influence of the curing state or higher decomposition in one of the atmospheres. In contrast to that the high temperature cured systems show differences for the one cured under air atmosphere as already mentioned before. The amide peak (1604 and 1577 cm^{-1}) for the air cured system is much higher than for the one under nitrogen. This is a result of the decomposition of the ester functions within the coating by the formed water. In case of the N_2 system a continuous nitrogen stream flowed over the samples and immediately removed the developed water. Thus the decomposition reaction cannot proceed. The complete list of the peaks appearing for the different curing conditions is given in Tab7.

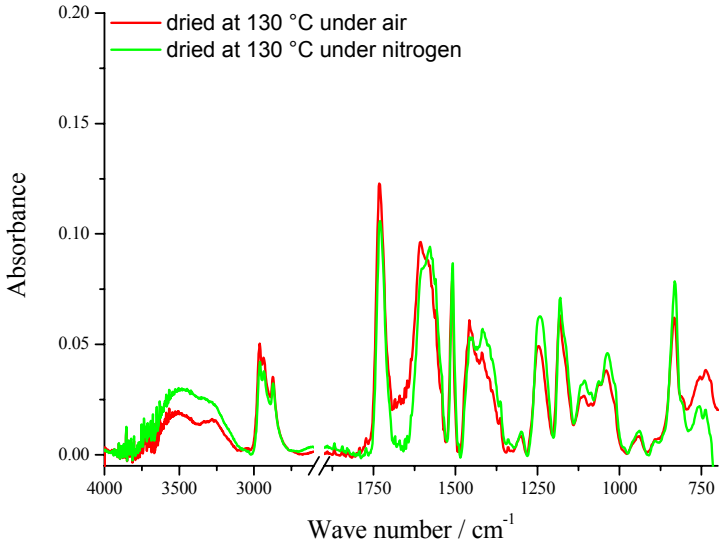

Fig. 92. Comparison of polyelectrolyte coated samples dried at 130 °C (under air and N_2) and room temperature. The curing conditions do not lead to changes in the polyelectrolyte film

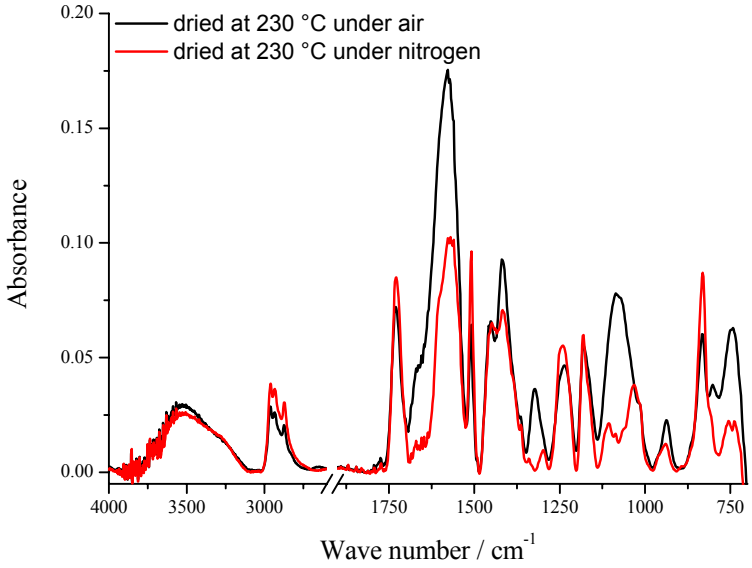

Fig. 93. Comparison of polyelectrolyte coated samples dried at 230 °C (under air and N_2) and room temperature. The curing under air increases the amount of formed amide bonds

Tab. 7. Assignment of the absorption peaks of the PET complexes dried at different temperatures

PET dried at RT (24h) /cm^{-1}	PET dried at RT (30d) /cm^{-1}	PET dried at 130 °C /cm^{-1}	PET dried at 230 °C (under air) /cm^{-1}	PET dried at 230 °C (under nitrogen) /cm^{-1}	Vibration
3080 - 3900	3080 - 3900	3080 - 3900	3080 - 3900	3080 - 3900	O-H
2872 - 2958	2872 - 2958	2872 - 2958	2872 - 2958	2872 - 2958	CH_2 and CH_3
1730	1730	1730	1730	1730	C=O
	1604	1606		1600	Amide
	1577	1577	1577	1570	Amide
1509	1509	1509	1509	1509	$-NH_3^+$
1457	1457	1457	1450	1448	C-H
	1419	1419	1419	1419	N-H
1246	1246	1246	1236	1239	-O-H
1182	1182	1182	1180	1181	C-O
1043	1037	1043	1083	1037	C-O
833	833	833	832	832	C-O

5.9.3 Hardness of polyelectrolyte layers

From the FT-IR measurements it is already visible that variations in curing temperature lead to differences in the forming of amide bonds and thereby to cross linking of the polymer film. Changes in the number of cross links should influence the hardness of the coating. The coating hardness was studied at curing temperatures of 130, 180 and 240 °C under air atmosphere (Fig. 94).

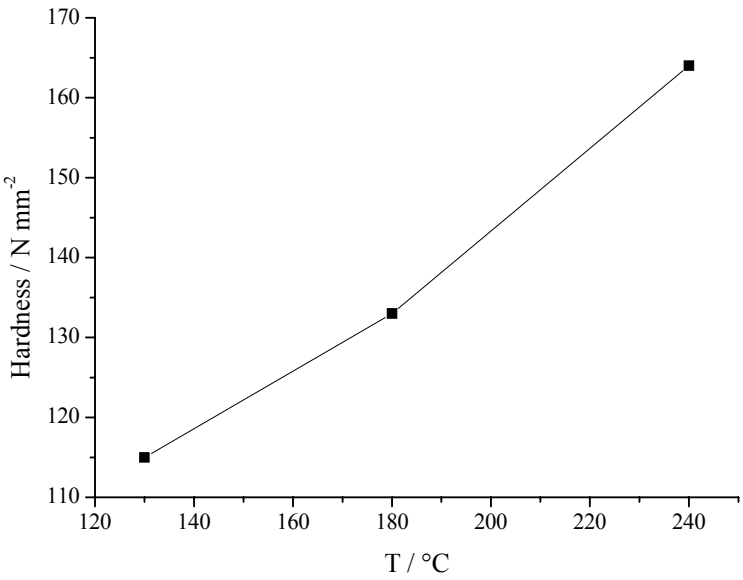

Fig. 94. Hardness of polyelectrolyte layers cured at different temperatures [taken from I. Klueppel, O. Seewald, R.Regenspurger, W. Bremser, G. Grundmeier, to be submitted]

With increasing curing temperature the coating hardness rises from 115 N/mm^2 at 130 °C to 165 N/mm^2 at 240 °C. The temperature dependence of the hardness underlines the FT-IR measurements and indicates the differences in the amount of amide bonds formed during the curing process. This should also influence further physical properties of the coating like formability and water uptake.

Further on the time dependent FT-IR measurements for room temperature cured polyelectrolyte layers show an increase of amide bonds even without heating. The ability of post curing of polyelectrolyte layers was also studied by hardness measurements over time at a layer cured at 130 °C (Fig. 95).

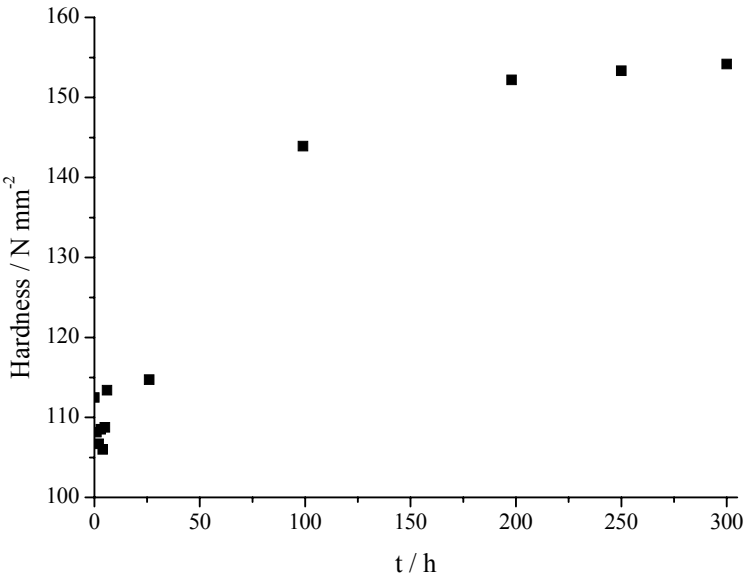

Fig. 95. Post curing of polyelectrolyte layer cured at 130 °C [taken from I. Klueppel, O. Seewald, R.Regenspurger, W. Bremser, G. Grundmeier, to be submitted]

The already cross linked system shows a further increase of hardness from about 107 N/mm^2 to about 155 N/mm^2 after 300 hours. The final hardness correlates with a coating cured at 220 °C (compare Fig. 94). The increase shows that the curing at 130 °C still leaves some reactive groups which can lead to a further cross linking with time.

5.9.4 Water uptake of polyelectrolyte layers dried at different temperatures

The protective properties of organic coatings against corrosion are based mainly on barrier properties blocking the transport of corrosive media. These barrier properties depend on the organic structure of the polymer and also on the cross linking state of the macro molecules within the coating. With increased cross linking the water uptake decreases and the barrier properties increase. Electrochemical Impedance Spectroscopy allows to follow the water uptake of organic coatings based on the Brasher-Kingsbury equation (eq. 56) using the coating capacitance as a function of immersion time in an electrolyte [28, 97, 98, 101, 170].

$$\varphi = \frac{\log C_t - \log C_0}{\log \varepsilon_{H_2O}} \cdot 100 \qquad \textbf{(eq. 56)}$$

With φ the water uptake in percent, C_t the coating capacitance at time t, C_0 the initial coating capacitance and ε_{H_2O} (78.5) the dielectric constant of water.

The impedance spectra of PET complex coated samples dried at different temperatures and under different atmospheres were recorded for some hours and afterwards used for the water uptake calculation.

The impedance spectrum of a PET coated sample dried at room temperature shows in the high frequency range from 100 kHz to 100 Hz a capacitive behaviour while at low frequencies the ohmic resistance of the coating is predominant (Fig. 96). After 20 hours of immersion in a borate buffer solution a change in barrier properties became visible by an increase of the resistance by nearly one order of magnitude in the low frequency range. Furthermore, the capacitively dominated range extended down to 10 Hz while the impedance in this range is significantly lower than in the initial state.

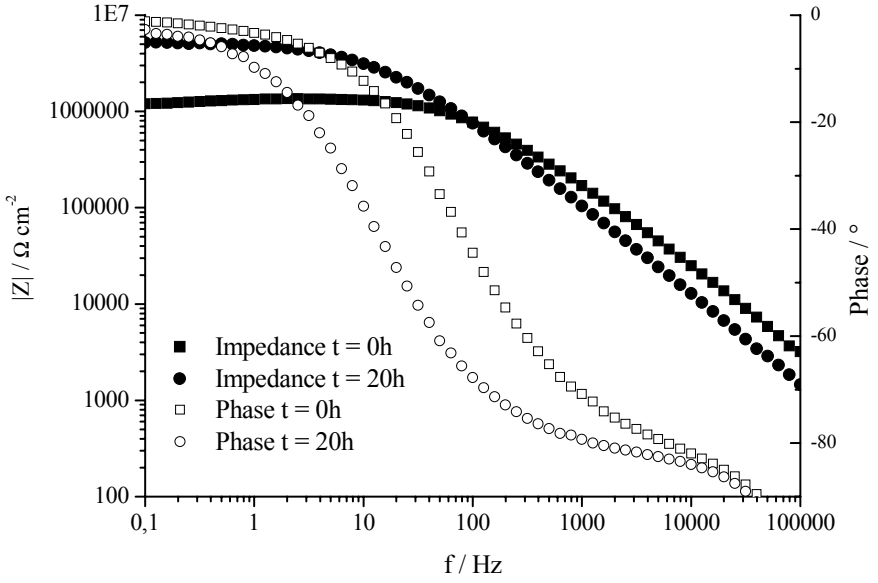

Fig. 96. Impedance spectra of PET complex dried at room temperature and immersed in borate buffer for different times, indicating a strong change in barrier properties over time

The PET coating dried at 130 °C shows a capacitive behaviour down to 10 to 1 Hz (Fig. 97). Only at very low frequencies a change in the ideal coating behaviour becomes visible. Over the immersion time the coating resistance only slightly increases indicating a well cross linked coating.

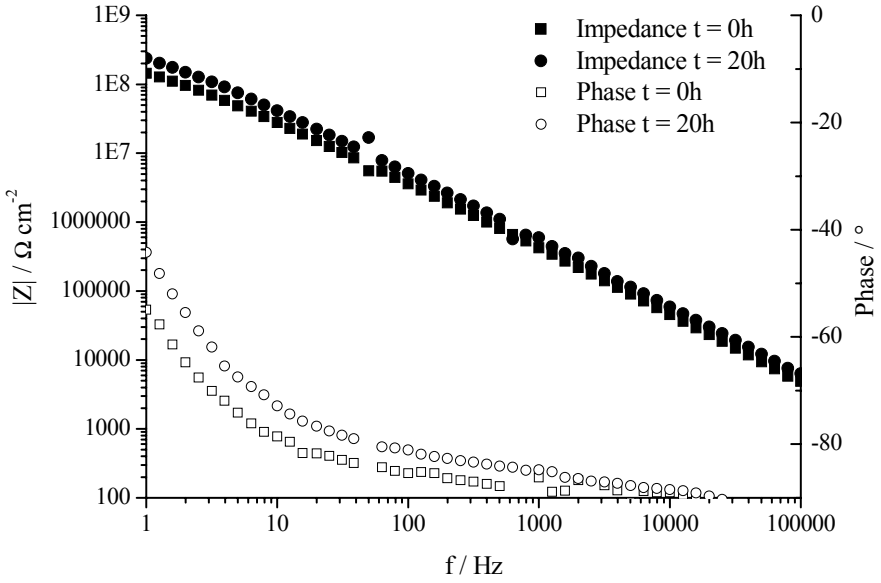

Fig. 97. Impedance spectra of PET complex dried 130 °C under standard atmosphere and immersed into borate buffer for different times, indicating only slight changes of the barrier properties over time

The coating dried at 230 °C shows an ideal behaviour over the complete frequency range with a phase shift of 90 ° (Fig. 98). The immersion for 9 hours leads to no significant changes in the coating properties indicating a highly cross linked polymer.

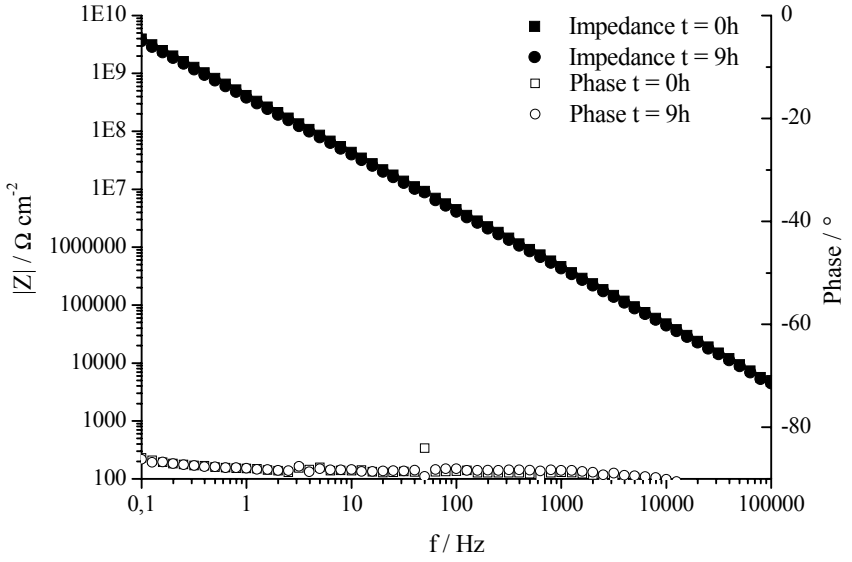

Fig. 98. Impedance spectra of PET complex dried at 230°C under standard atmosphere and immersed into borate buffer for different times, indicating nearly no change of the barrier properties over time

The coating dried at 230 °C under nitrogen atmosphere shows differences in the low frequency resistance in comparison to the one dried under air atmosphere. At frequencies

below 10 Hz the coating changes from a purely capacitive behaviour to one with a clearly ohmic behaviour. Long time immersion leads to only slight changes in the phase shift ranging to higher frequencies and a less dominant ohmic behaviour. The barrier property indicated by the low frequency resistance seems not to be affected.

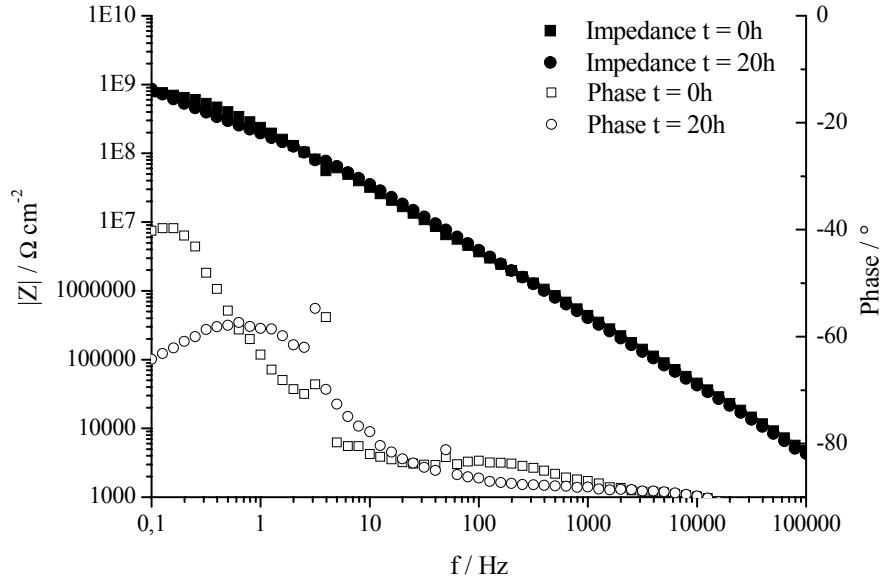

Fig. 99. Impedance spectra of PET complex dried at 230°C under nitrogen and immersed into borate buffer for different times, indicating nearly no change of the barrier properties over time

The water uptake calculated from the time dependent impedance spectra taken for the differently cured coatings shows significant differences (Fig. 100). The coating dried at room temperature shows a high water uptake of about 19.5 % indicating just a low cross linking with only weak barrier properties. With increasing curing temperature a clear change in the coating properties becomes visible. At 130 °C the water uptake strongly decreases to 5.5 % and the initial slope increases very strongly leading to a quicker achievement of the plateau. The further increase of temperature to 230 °C leads to even less water uptake in the range of 1.5 % with a similar slope like the one dried at 130 °C.

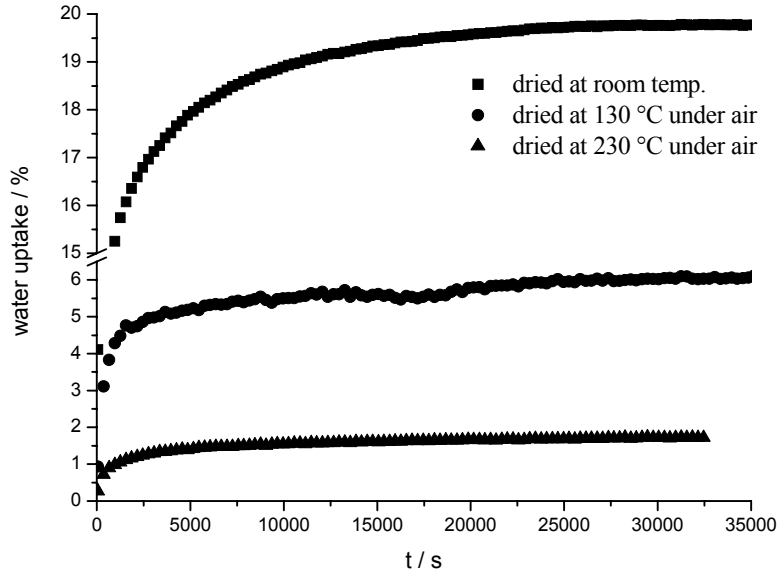

Fig. 100. Water uptake of a polyelectrolyte film dried at room temperature, 130°C and 230°C under air. The water uptake decreases with increasing curing temperature and cross linking of the system

The comparison of the two coatings dried at 230 °C but under different atmospheres (air and nitrogen) shows nearly no differences in the slope and total amount of water uptake (Fig. 101).

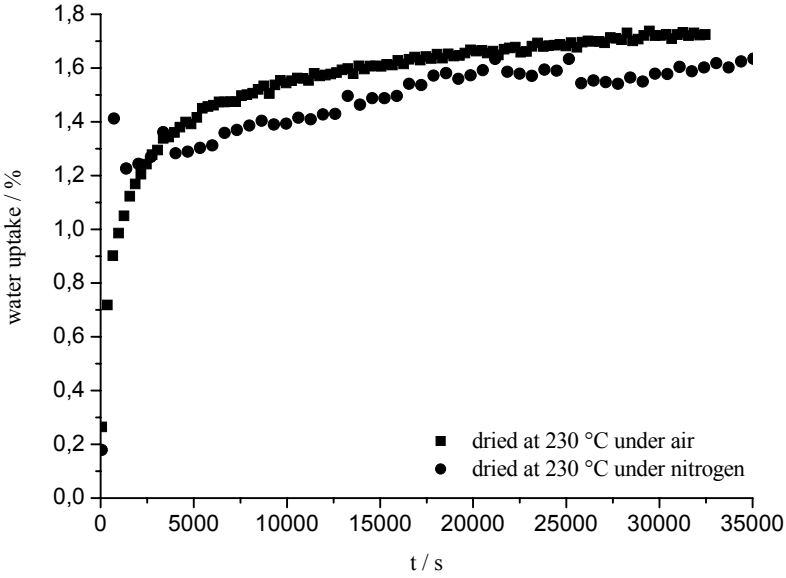

Fig. 101. Water uptake of a polyelectrolyte film dried at 230°C under air and nitrogen. The different atmospheres show no influence on the water uptake of the system

The water uptake for the systems cured under air atmosphere was plotted versus curing temperature and is given in Fig. 102.

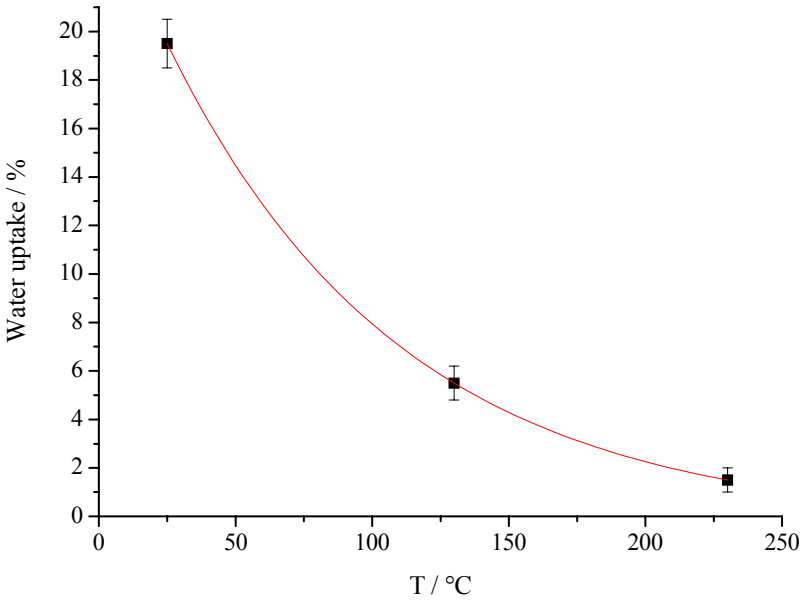

Fig. 102. Water uptake versus curing temperature for PET system cured under standard atmosphere. The water uptake follows an exponential decay with increasing curing temperatures

The reduction of the water uptake with increasing temperature follows a 1st order exponential decay indicating a strong cross linking during drying even for medium temperatures.

5.9.5 FE-SEM investigation of formed polyelectrolyte layers

The formed and unformed polyelectrolyte coated samples were analysed by FE-SEM to identify the formation of defects. The images of the unformed samples show a formation of compact films that follow the surface roughness of the electrogalvanised substrate (Fig. 103). The sample dried at room temperature (24h) shows certain pores within the coating while the two other films are free of defects. The defect formation might occur due to the brittle properties of the coating if the solvent is evaporated while no bond formation between the polymer chains happens.

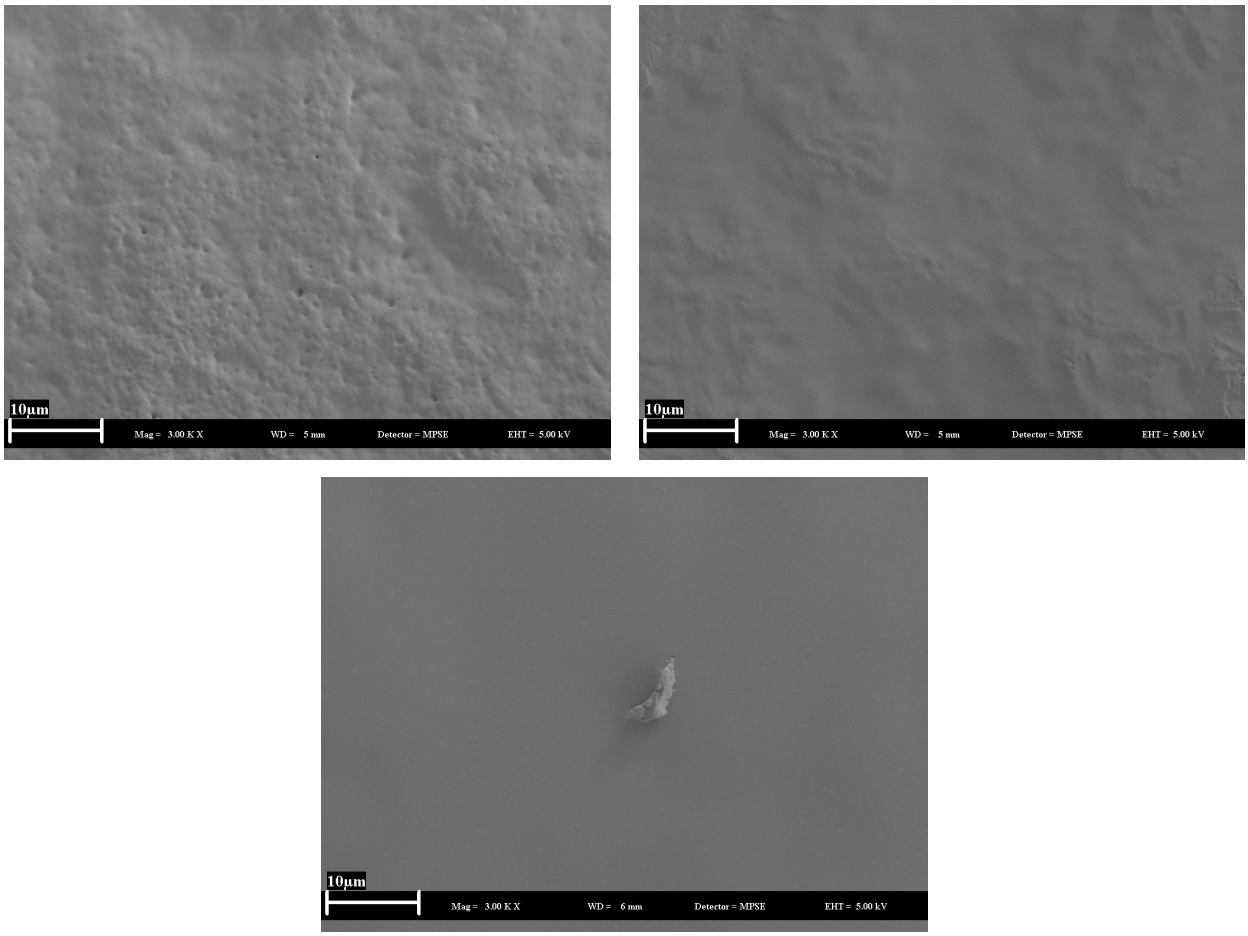

Fig. 103. SEM image of unformed polyelectrolyte coated samples dried under standard atmosphere at room temperature (top left), at 130 °C (top right) and 230 °C (bottom). At room temperature the formation of certain pores is visible while at higher temperatures smooth films are formed

The elongated samples show formation of defects perpendicular to the direction of the major strain (Fig. 104). There were no favourite defect sites as in the pigmented coatings and the defects are statistically distributed over the complete sample.

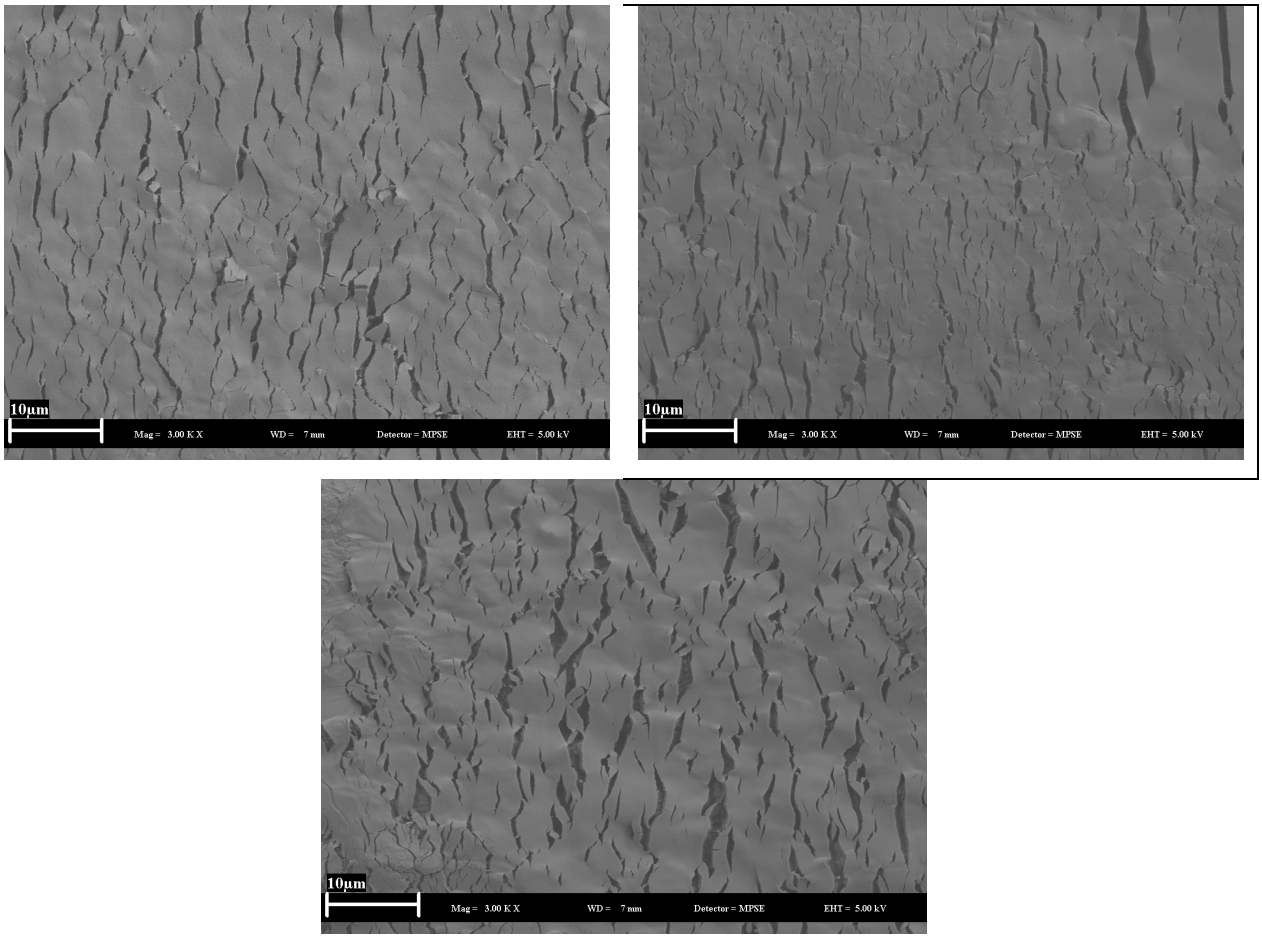

Fig. 104. SEM image of 20 % elongated polyelectrolyte coated samples dried under standard atmosphere at room temperature (top left), at 130 °C (top right) and 230 °C (bottom). For all curing temperatures the forming leads to defects within the coating

The defects size allows a ranking of the different curing conditions with 130 °C on top showing on average the smallest defects, the RT dried sample with larger defects and finally the sample cured at 230 °C. The last one shows a homogeneous distribution of large defects that would dramatically reduce the barrier properties of the coating.

5.9.6 In-situ Electrochemical Impedance Spectroscopy during stretch forming of polyelectrolyte layers

The in-situ Electrochemical Impedance Spectroscopy during the stretch forming of the polyelectrolyte coated samples were performed with similar miniature stretching samples as already described for the testing of corrosion protection primers. The samples were cut out by a laser, three step solvent cleaned and afterwards alkaline cleaned by a coil coating cleaner. The coating was applied by dip coating with a home-built dip coater (dipping speed 2 mm/s).

The samples were dried / cured at different temperatures (RT 24 h drying, 130 °C and 230 °C) and under standard or nitrogen atmosphere.

5.9.6.1 Formability of a polyelectrolyte layer dried at room temperature

The room temperature dried polyelectrolyte coating shows in the unformed state a broad capacitive behaviour from 100000 Hz down to 10 Hz (Fig. 105). The low frequency resistance reaches 1 MΩ / cm^2 indicating high barrier properties. At an elongation of 5% the separation into two time constants becomes visible. In the high frequency range the capacitive characteristic ranges from 100000 Hz down to 1000 Hz. The low frequency part has a capacitive part from 10 to 0.1 Hz. The first range has its minimum at 10000 Hz while the second one shows a minimum between 2 and 3 Hz. With increasing elongation the distribution into the two time constants becomes more and more dominant. In the high frequency area the minimum in the phase shift changes from -75° to -40° while the low frequency minimum increases from -30° to -50°. The low frequency resistance decreases by one order of magnitude due to an elongation to 20%.

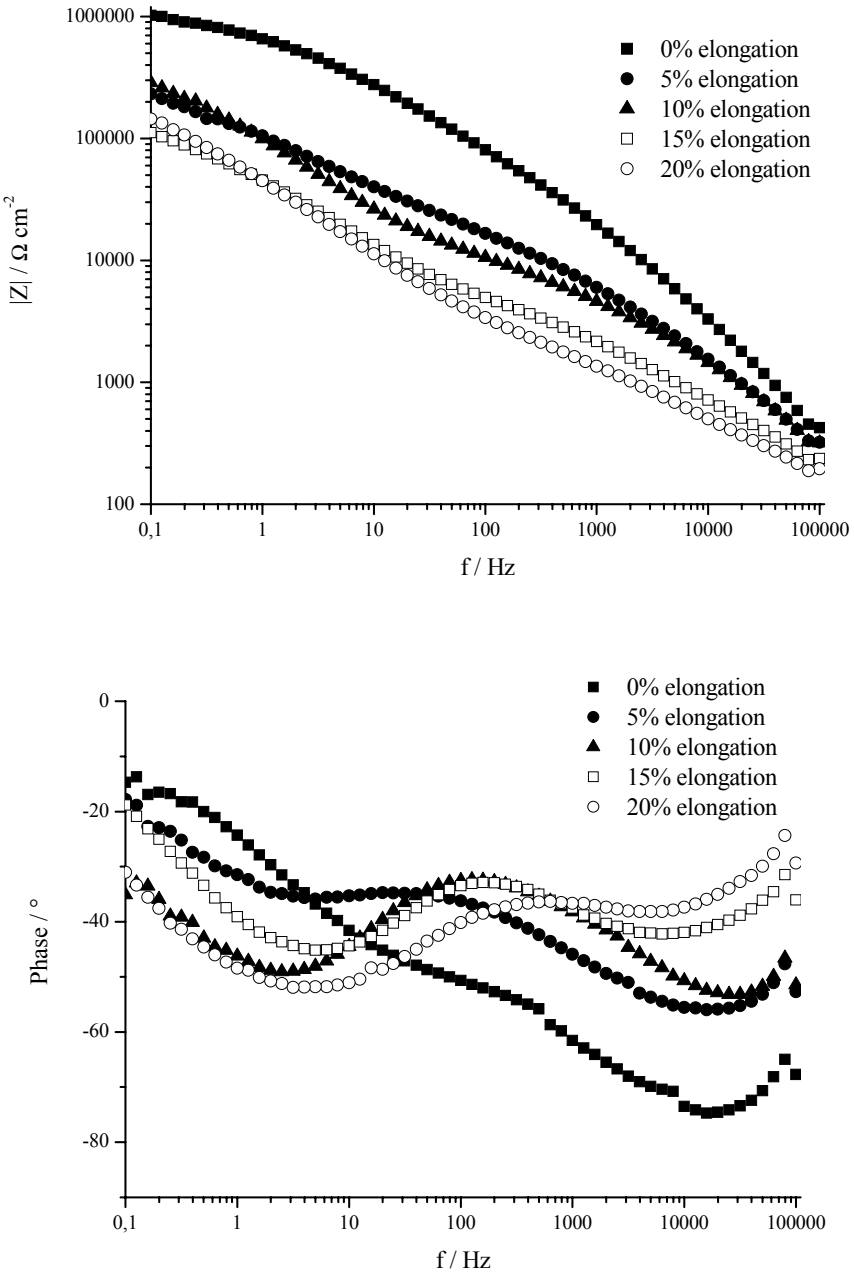

Fig. 105. In-situ EIS during the forming of PET layer on electrogalvanised steel dried at room temperature for 24 h. The forming leads to a decrease in the barrier properties of the coating by the formation of defects

The thickness reduction of the coating seems to lead to a separation of the two time constants (organic coating and double layer). The increase of the low frequency minimum can be caused by the easier diffusion of water molecules through the coating and the formation of a more significant double layer.

5.9.6.2 Formability of a polyelectrolyte layer dried at 130°C

The polyelectrolyte layer shows capacitive behaviour in the range of 10000 to 10 Hz in the unformed state with a minimum for the phase shift of -75° at 1000 Hz (Fig. 106). The low frequency resistance shows good barrier properties with a value of about 1 MΩ / cm^2. The increase of the forming degree leads to a shift of the capacitive range to 1000 and 1 Hz and also to a shift of the phase minimum to 50 Hz at 20% elongation. At higher elongations the minimum of the phase shift drifts from -75° to -65° and shows a lesser broad structure. The loss in low frequency resistance is less significant than for the room temperature dried sample with just half an order of magnitude.

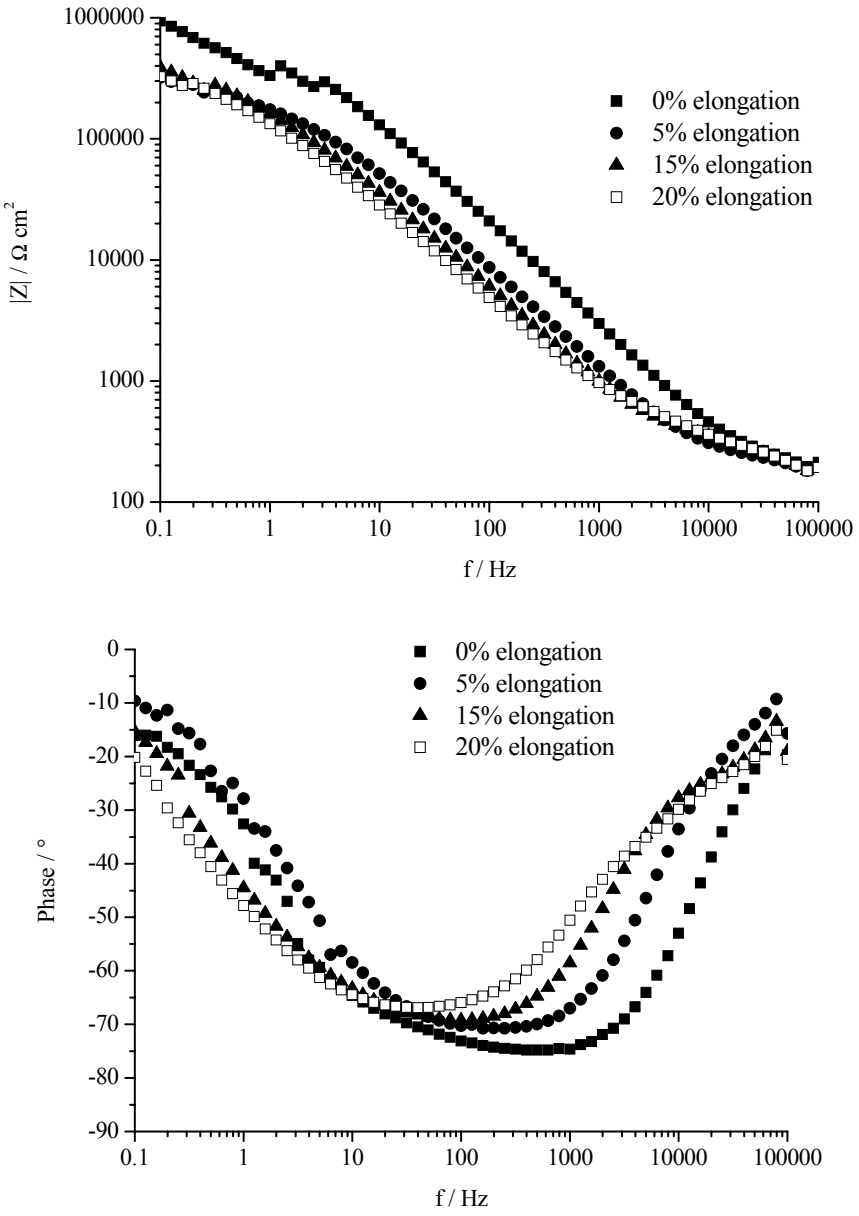

Fig. 106. In-situ EIS during forming of PET layer on electrogalvanised steel dried at 130 °C. The forming leads to a decrease in the barrier properties of the coating by the formation of defects

The slight change in the low frequency resistance even at high forming degrees indicates a good formability of the coating with excellent barrier properties. The shift of the capacitive range and the absolute minimum is caused by the thickness reduction of the coating during the forming process.

5.9.6.3 Formability of a polyelectrolyte layer dried at 230°C

The system dried under standard conditions shows capacitive properties in the range from 1000 Hz down to 0.1 Hz with a low frequency resistance of 400000 Ω / cm^2 for the unformed state (Fig. 107). The phase shift shows a broad distribution with a minimum of -80°at 10 Hz. Elongation of only 5% leads to a dramatic loss of the barrier properties by nearly two orders of magnitude. The capacitive area decreases to the range of 400 to 3 Hz with a sharp minimum of -65° at 40 Hz. With further elongation the minimum shifts to -50° at 50 Hz, simultaneously the low frequency resistance decreases further to 2000 Ω / cm^2.

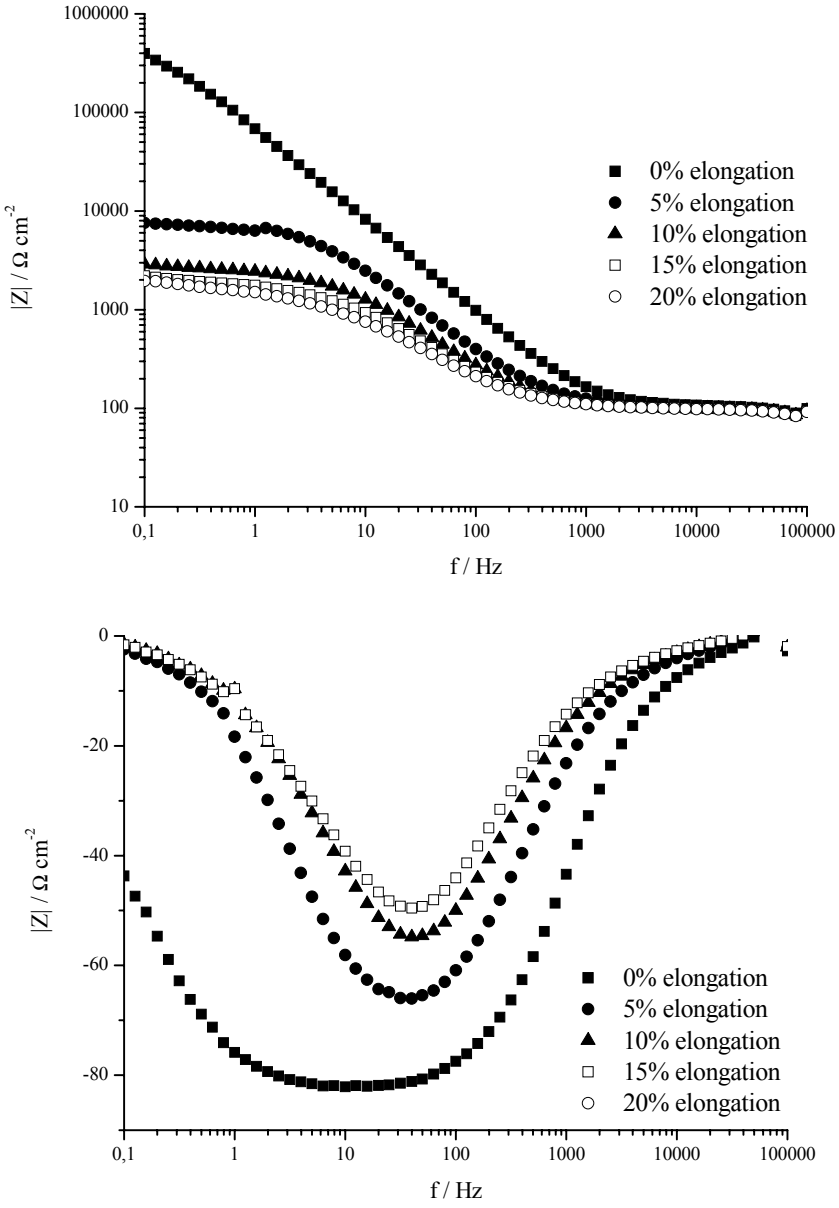

Fig. 107. In-situ EIS during forming of PET layer on electrogalvanised steel dried at 230 °C under air. The forming leads to a decrease in the barrier properties of the coating by the formation of defects

The impedance spectra of the high temperature cured coating (standard atmosphere) show high barrier properties in the unformed state. But the first forming step leads to a dramatic loss of these properties with a final spectrum similar to the one of an uncoated electrogalvanised steel sample. The high temperature seems to lead to a highly dried and hardened system with a brittle structure. Such a system completely loses its formability and cannot withstand the applied forces during forming.

The impedance spectra were non linearly fitted to calculate reproducible values for the low frequency resistance at 0.1 Hz (Tab. 8). This procedure avoids errors from scattered measurement point due to noise uptake by the potentiostat. The data were normalised to the initial value at an elongation of 0% and plotted in Fig. 108. The initial values for the polymer layer dried at room temperature and at 130 °C show a significant higher resistance resulting in much better barrier properties. The high temperature cured coatings, especially the one dried under nitrogen, show much lower resistances and significant lower final values.

Tab. 8. Resistance of PET complex layer at 0.1 Hz taken from non-linear impedance fit

	PET dried at RT / Ω cm²	**PET dried at 130 °C / Ω cm²**	**PET dried at 230 °C (standard atmosphere) / Ω cm²**
0 % elongation	961575	771375	319020
5 % elongation	202337	291096	7171
10 % elongation	249472	-	2734
15 % elongation	99016	340988	2053
20 % elongation	123676	299192	1848

The comparison of the PET layers dried at room temperature, 130 °C and 230° under standard atmosphere shows a clear ranking with regard to formability (Fig. 108). The coating dried at 130 °C shows only a loss of about 50 % of its initial barrier property even at high forming degrees. The room temperature dried one loses about 80 % of its initial value while the one dried at 230 °C loses nearly its complete corrosion protection properties. In all cases the final loss of the protective properties occurs in the first forming step and stabilises at higher forming degrees.

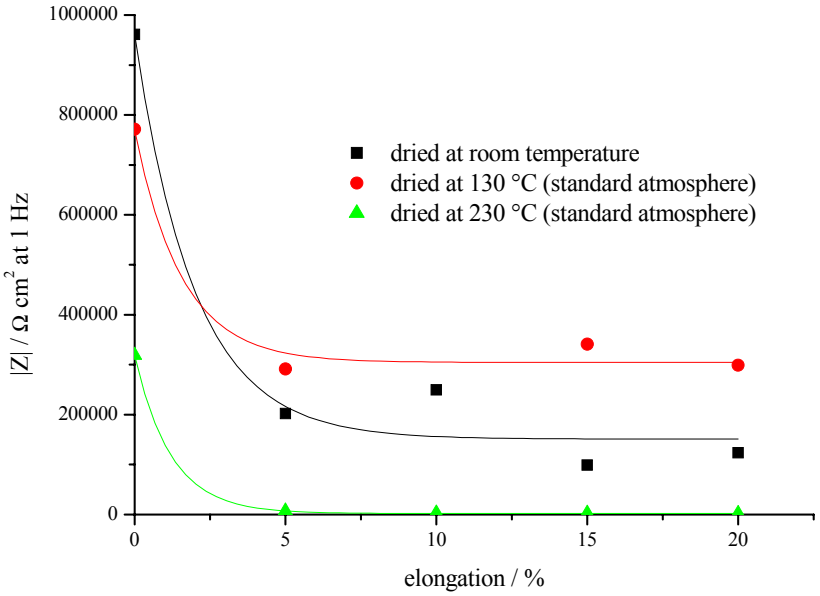

Fig. 108. Comparison of the formability of PET complexes cured at different temperatures. The system dried at 130 °C shows the best forming performance with a decrease of the barrier properties to 40 %.

The information about the optimal curing conditions is of great interest as the formability and thereby the barrier properties directly correspond with them. Too low temperatures would not lead to the necessary cross linking while a too high temperature may lead to degradation of the coating. It becomes clear that the optimal formability is reached at a medium temperature of 130 °C for the investigated PET system.

6 Overall conclusions

The scope of this thesis was the development of new analytical tools to investigate the formability, corrosion and barrier properties of organic coatings applied on electrogalvanised steel. Thus the work focused on innovative, combined in-situ methods which generate detailed information about the system under investigation. A new electrochemical capillary cell setup was built, combining impedance spectroscopy with simultaneous forming of a sample. Detailed information about the loss of the barrier properties during stretch forming by the formation of defects and the corrosive attack of the electrolyte are gained by this setup. Further results of the local loss of barrier properties and the corrosion product formation can be obtained from the combination of a confocal Raman spectrometer with an electrochemical capillary cell. Finally the new in-situ Raman / QCM flow cell allows the measurement of adsorption kinetics and dissolution processes of e.g. inhibitors and further on allows the identification of the products involved.

The lab coated pretreatment and corrosion protection primer show homogeneous distribution and layer formation. The zinc particles embedded in the coating sizes from 2 – 7 µm are covered with a rough oxide layer and form no direct, conducting contact between the coating surface and the steel substrate. All uniaxial, biaxial, plane strain formed and also the miniature stretching samples show a uniform strain distribution over the complete area under investigation. The forming of the corrosion protection primer leads to the formation of defects at the zinc particle / binder interface growing with increasing strain while the underneath zinc structure shows no defects. Furthermore, the formed coating detaches from the substrate and generates small sheltered caverns.

The cleaning procedure of the formed CPPs shows no visible influence on the surface structure of the implemented zinc particles while the tendency to the formation of small phosphate crystals rises with increasing pH of the cleaning solution. The precipitation of the phosphate crystals appears on the free zinc area on top of the pigments and in the defects induced by the forming procedure. Thus the existence and size of defects influences the kinetic of the phosphating process which is accelerated by the amount of the free zinc surface.

The cleaning procedure shows no influence on the corrosion performance of the CPP in the VDA climate test while the forming leads to a loss of the protective properties due to the defect formation. The blistering of ED-paint applied on CPP additionally is just dependant on pre-forming for very thin thicknesses of about 4 µm. With common thicknesses of about 15 –

20 µm the barrier properties of the ED-paint are the corrosion rate limiting step and no distinction between formed and unformed samples can be observed.
FE-SEM and FIB analysis of formed (20 % elongated) CPP after 24 h salt spray test indicate a strong local corrosion in the area of the forming induced caverns. The corrosion rate in these caverns is significantly higher than on flat samples corresponding to a complete degradation of the zinc layer after almost 24 h on local sites.
The in-situ Impedance Spectroscopy during stretch forming shows the formation of initial defects already at small forming degrees. Further elongation leads to a significant loss of the barrier properties while at high forming degrees (25 % elongation) the protection of the coating is nearly completely destroyed which is indicated by the impedance value as of the pure substrate.
Combined Raman / Impedance spectra indicate only a increase of in the formation of corrosion products within two hours. While the barrier property degradation of the formed CPP is a very fast process showing a significant change in the impedance.
The surface modification of the zinc particles to strengthen the bonding between the particles and the binder matrix showed no reduction of the forming induced defects due to the high strain inside the system.
The overall results indicate that a fast corrosive deadhesion along the particle/ binder interface appears almost in the unformed state. After forming the induced defects and caverns allow an easy penetration of the electrolyte and act as initial sites for a corrosive attack of the substrate and the delamination of the coating.

The in-situ Raman / QCM measurements show a comprehensive view of the MBT inhibitor adsorption on SERS active gold. The formation of a monolayer was completed after 6 minutes and could be correlated with the theoretically calculated frequency shift.

The investigated polyelectrolyte layers show the formation of covalent bonds after the drying for several days at room temperature or after curing at temperatures of 130 or 230 °C. The water uptake is reduced due to curing from 19.5 % for the room temperature dried coating to 5.5 % at 130 °C to finally 1.5 % for the one dried at 230 °C. Forming leads to the formation of defects perpendicular to the elongation direction. The best formability is found for the coatings cured at 130 °C while the dried at RT and 230 °C shows a significantly worse formability.

7 Outlook

In future studies the embedded zinc particles might be exchanged by other metal or alloy pigments that guarantee the electrical conduction for spot welding and further on have a better adhesion to the binder matrix and provide passivating properties. E.g. the formation of voluminous, inhibiting corrosion products would allow a complete closure of the forming induced defects at the particle / binder interface.

Other aspects to be considered are the passivation of the zinc particles by e.g. similar solutions already used as pretreatment for the galvanised steel substrate. This could lead to a reduction of corrosive delamination along the particle / binder interface resulting in a fast decrease of the coating barrier properties.

The design of binder systems with low glass transition temperatures that allow closure of forming induced defects at temperatures of about 180 °C, as they appear during curing of the ED-paint, could probably significantly increase the barrier properties of the coating.

For polyelectrolyte coatings the kinetic of the cross linking should be further investigated as this is of great importance for further technical applications concerning the formability after the storage of the coated coils. For these systems also the double curing after application and after ED-paint application might be suitable for improving the barrier properties. Further on the electrical conductivity needed for spot welding might be increased by the implementation of conductive polymers.

The setups developed within this thesis can be used to support the coating design by the fast testing of new products concerning the formability and influence of implemented inhibitors. But they are not only limited to coatings due to the high local resolution, they can also be used to indentify and analyse the properties of e.g. inhomogeneous particles embedded in metals or other technical products.

8 Publications

[1] C. Stromberg, P. Thissen, I. Klueppel, N. Fink and G. Grundmeier, *"Synthesis and characterisation of surface gradient thin conversion films on zinc coated steel"*, *Electrochimica Acta*, **52**, 804 (2006)

[2] R. Vlasak, I. Klueppel and G. Grundmeier, *"Combined EIS and FTIR–ATR study of water uptake and diffusion in polymer films on semiconducting electrodes"*, *Electrochimica Acta*, **52**, 8075 (2007)

[3] I. Klueppel, B. Schinkinger, G. Grundmeier, "*In-Situ Electrochemical Studies of the Formability of Organic Coatings on Metals"*, submitted to *Electrochimica Acta*

[4] I. Klueppel, G. G. Sun, G. Grundmeier, "*In-situ investigation of the kinetic adsorption process of 2-mercaptobenzothiazole by combining surface-enhanced Raman spectroscopy and quartz crystal microbalance"*, in preparation

[5] I. Klueppel, O. Seewald, R. Regenspurger, W. Bremser, G. Grundmeier, in preparation

9 Literature

[1] B. F. Chen, J. Hwang, I. F. Chen, G. P. Yu and J. H. Huang, *Surf. Coat. Technol.*, **126**, 91 (2000)

[2] B. Baumert, M. Stratmann and M. Rohwerder, *Z. Metallk.*, **95**, 447 (2004)

[3] A. C. Bastos and A. M. P. Simoes, *Progress in Organic Coatings*, **46**, 220 (2003)

[4] L. Fedrizzi, A. Bergo and M. Fanicchia, *Electrochimica Acta*, **51**, 1864 (2006)

[5] B. S. Skerry and C. H. Simpson, *Corrosion*, **49**, 663 (1993)

[6] M. Delucchi, A. Barbucci and G. Cerisola, *Electrochimica Acta*, **44**, 4297 (1999)

[7] E. P. M. van Westing, G. M. Ferrari and J. H. W. de Wit, *Corrosion Sci.*, **36**, 979 (1994)

[8] F. Mansfield and M. W. Kending, *Werkstoffe und Korrosion*, **36**, 473 (1985)

[9] F. Mansfeld and C. H. Tsai, *Corrosion*, **47**, 958 (1991)

[10] U. Rammelt and G. Reinhardt, *Progress in organic coatings*, **21**, 205 (1992)

[11] E. Cavalcanti and O. Ferraz, *Progress in organic coatings*, **23**, 185 (1993)

[12] H.-R. Prause, Anwendbarkeit der Impedanzspektroskopie zur Beurteilung des Korrosionsschutzes durch organische Beschichtungen, in *Chemie*, Stuttgart (1994)

[13] F. Mansfeld, *J. Appl. Electrochem.*, **25**, 187 (1995)

[14] P. L. Bonora, F. Deflorian and L. Fedrizzi, *Electrochimica Acta*, **41**, 1073 (1996)

[15] D. H. van der Weijde, E. P. M. van Westing and J. H. W. de Wit, *Electrochimica Acta*, **41**, 1103 (1996)

[16] F. Mansfeld, H. Xiao;, L. T. Han and C. C. Lee, *Progress in organic coatings*, **30**, 89 (1997)

[17] N. Tang, W. J. v. Ooij and G. Górecki, *Progress in organic coatings*, **30**, 255 (1997)

[18] A. Miszczyk and K. Darowicki, *Corrosion Sci.*, **40**, 663 (1998)

[19] F. Deflorian, L. Fedrizzi, S. Rossi and P. L. Bonora, *Electrochimica Acta*, **44**, 4243 (1999)

[20] A. S. L. Castela, A. M. Simoes and M. G. S. Ferreira, *Progress in organic coatings*, **38**, 1 (2000)

[21] R. M. Souto, V. Fox, M. M. Laz and S. González, *J. Adhes. Sci. Technol.*, **14**, 1321 (2000)

[22] J. Vogelsang and W. Strunz, *Materials and Corrosion*, **52**, 462 (2001)

[23] V. Lavaert, M. Moors and E. Wettinck, *J. Appl. Electrochem.*, **32**, 853 (2002)

[24] G. Bierwagen, D. Tallman, J. P. Li, L. Y. He and C. Jeffcoate, *Progress in Organic Coatings*, **46**, 148 (2003)

[25] J. M. Hu, J. T. Zhang, J. Q. Zhang and C. N. Cao, *Journal of Materials Science*, **39**, 4475 (2004)

[26] V. Barranco and S. Feliu, *Corrosion Sci.*, **46**, 2203 (2004)

[27] V. Barranco and S. Feliu, *Corrosion Sci.*, **46**, 2221 (2004)

[28] D. Loveday, P. Peterson and B. Rodgers, *Jct Coatingstech*, **1**, 88 (2004)

[29] A. C. Bastos, C. Ostwald, L. Engl, G. Grundmeier and A. M. Simoes, *Electrochimica Acta*, **49**, 3947 (2004)

[30] K. Darowicki, J. Orlikowski and A. Arutunow, *Electrochimica Acta*, **48**, 4189 (2003)

[31] K. Darowicki and M. Szocinski, *J. Solid State Electrochem.*, **8**, 346 (2004)

[32] G. Decher, Y. Lvov and J. Schmitt, *Thin Solid Films*, **244**, 772 (1994)

[33] F. Caruso, K. Niikura, D. N. Furlong and Y. Okahata, *Langmuir*, **13**, 3422 (1997)

[34] J. B. Schlenoff, H. Ly and M. Li, *J. Am. Chem. Soc.*, **120**, 7626 (1998)

[35] D. Yoo, S. S. Shiratori and M. F. Rubner, *Macromolecules*, **31**, 4309 (1998)

[36] J. J. Harris, P. M. DeRose and M. L. Bruening, *J. Am. Chem. Soc.*, **121**, 1978 (1999)

[37] P. Bertrand, A. Jonas, A. Laschewsky and R. Legras, *Macromol. Rapid Commun.*, **21**, 319 (2000)

[38] J. H. Dai, A. W. Jensen, D. K. Mohanty, J. Erndt and M. L. Bruening, *Langmuir*, **17**, 931 (2001)

[39] B. Schoeler, G. Kumaraswamy and F. Caruso, *Macromolecules*, **35**, 889 (2002)

[40] T. R. Farhat and J. B. Schlenoff, *Electrochem. Solid State Lett.*, **5**, B13 (2002)

[41] G. Ibarz, L. Dahne, E. Donath and H. Mohwald, *Chem. Mat.*, **14**, 4059 (2002)

[42] B. Schoeler, E. Poptoschev and F. Caruso, *Macromolecules*, **36**, 5258 (2003)

[43] A. V. Dobrynin and M. Rubinstein, *Prog. Polym. Sci.*, **30**, 1049 (2005)

[44] M. D. Miller and M. L. Bruening, *Chem. Mat.*, **17**, 5375 (2005)

[45] G. Francius, J. Hemmerle, J. Ohayon, P. Schaaf, J. C. Voegel, C. Picart and B. Senger, *Microscopy Research and Technique*, **69**, 84 (2006)

[46] A. Schneider, G. Francius, R. Obeid, P. Schwinte, J. Hemmerle, B. Frisch, P. Schaaf, J. C. Voegel, B. Senger and C. Picart, *Langmuir*, **22**, 1193 (2006)

[47] K. Lange, *Umformtechnik*, Springer, Berlin (1984)

[48] E. Doege and B.-A. Behrens, *Handbuch Umformtechnik*, Springer, Berliner (2007)

[49] R. Parisot, S. Forest, A. F. Gourgues, A. Pineau and D. Mareuse, *Comput. Mater. Sci.*, **19**, 189 (2000)

[50] K. P. Imlau, K. D. Ehlers, S. M. Goklu, K. P. Mohr and D. Wolfhard, *Stahl Und Eisen*, **113**, 69 (1993)

[51] B. Tieke, *Makromolekulare Chemie*, Wiley-VCH, Weinheim (2005)

[52] *Stahl-Eisen-Prüfblatt 1160*, Stahlinstitut VDEh, Düsseldorf (2004)

[53] T. Narayanan, *Rev. Adv. Mater. Sci.*, **9**, 130 (2005)

[54] P. Puomi, H. M. Fagerholm, J. B. Rosenholm and K. Jyrkas, *Surf. Coat. Technol.*, **115**, 70 (1999)

[55] C. Stromberg, P. Thissen, I. Klueppel, N. Fink and G. Grundmeier, *Electrochimica Acta*, **52**, 804 (2006)

[56] B. Wilson, N. Fink and G. Grundmeier, *Electrochimica Acta*, **51**, 3066 (2006)

[57] N. Fink, B. Wilson and G. Grundmeier, *Electrochimica Acta*, **51**, 2956 (2006)

[58] G. Klimow, N. Fink and G. Grundmeier, *Electrochimica Acta*, **53**, 1290 (2007)

[59] U. A. Handge, I. M. Sokolov, A. Blumen, E. Kolb and E. Clement, *J. Macromol. Sci.-Phys.*, **B38**, 971 (1999)

[60] C. Lorenz-Haas, P. Muller-Buschbaum, T. Ittner, J. Kraus, B. Mahltig, S. Cunis, G. V. Krosigk, R. Gehrke, C. Creton and M. Stamm, *Phys. Chem. Chem. Phys.*, **5**, 1235 (2003)

[61] A. C. Moloney and H. H. Kausch, *J. Mater. Sci. Lett.*, **4**, 289 (1985)

[62] G. H. Michler, *J. Macromol. Sci.-Phys.*, **B38**, 787 (1999)

[63] R. P. Wool, *Soft Matter*, **4**, 400 (2008)

[64] S. R. White, N. R. Sottos, P. H. Geubelle, J. S. Moore, M. R. Kessler, S. R. Sriram, E. N. Brown and S. Viswanathan, *Nature*, **409**, 794 (2001)

[65] K. Aramaki, *Corrosion Sci.*, **44**, 1621 (2002)

[66] K. Aramaki, *Corrosion Sci.*, **44**, 1375 (2002)

[67] K. Aramaki, *Corrosion Sci.*, **45**, 2361 (2003)

[68] M. R. Kessler, N. R. Sottos and S. R. White, *Compos. Pt. A-Appl. Sci. Manuf.*, **34**, 743 (2003)

[69] A. N. Khramov, N. N. Voevodin, V. N. Balbyshev and M. S. Donley, *Thin Solid Films*, **447**, 549 (2004)

[70] K. Aramaki, *Corrosion Sci.*, **47**, 1285 (2005)

[71] G. Paliwoda-Porebska, M. Stratmann, M. Rohwerder, K. Potje-Kamloth, Y. Lu, A. Z. Pich and H. J. Adler, *Corrosion Sci.*, **47**, 3216 (2005)

[72] A. Kumar, L. D. Stephenson and J. N. Murray, *Progress in Organic Coatings*, **55**, 244 (2006)

[73] M. L. Zheludkevich, K. A. Yasakau, A. C. Bastos, O. Karavai and M. G. S. Ferreira, *Electrochem. Commun.*, **9**, 2622 (2007)

[74] W. Feng, S. H. Patel, M. Y. Young, J. L. Zunino and M. Xanthos, *Adv. Polym. Technol.*, **26**, 1 (2007)

[75] D. Y. Wu, S. Meure and D. Solomon, *Prog. Polym. Sci.*, **33**, 479 (2008)

[76] N. G. Hoogeveen, M. A. C. Stuart and G. J. Fleer, *Langmuir*, **12**, 3675 (1996)

[77] D. G. Shchukin, M. Zheludkevich, K. Yasakau, S. Lamaka, M. G. S. Ferreira and H. Mohwald, *Adv. Mater.*, **18**, 1672 (2006)

[78] D. G. Shchukin and H. Mohwald, *Small*, **3**, 926 (2007)

[79] F. Micciche, H. Fischer, R. Varley and S. van der Zwaag, *Surf. Coat. Technol.*, **202**, 3346 (2008)

[80] D. G. Shchukin and H. Mohwald, *Adv. Funct. Mater.*, **17**, 1451 (2007)

[81] C. Gabrielle and M. Keddam, *Corrosion*, **48**, 794 (1992)

[82] M. M. Lohrengel, *Materials Science & Engineering R-Reports*, **11**, 243 (1993)

[83] J. Colreavy and J. D. Scantlebury, *Journal of Materials Processing Technology*, **55**, 206 (1994)

[84] M. Itagaki, A. Matsuzaki and K. Watanabe, *Corrosion Sci.*, **37**, 1867 (1995)

[85] P. Schmuki, H. Bohni and J. A. Bardwell, **142**, 1705 (1995)

[86] W. P. Gomes and D. Vanmaekelbergh, *Electrochimica Acta*, **41**, 967 (1996)

[87] A. Nishikata, Y. Ichihara and T. Tsuru, *Electrochimica Acta*, **41**, 1057 (1996)

[88] J. H. W. de Wit and H. J. W. Lenderink, *Electrochimica Acta*, **41**, 1111 (1996)

[89] M. Gaberscek and S. Pejovnik, *Electrochimica Acta*, **41**, 1137 (1996)

[90] P. Birke and W. Weppner, *Electrochimica Acta*, **42**, 3375 (1997)

[91] Z. Kerner and T. Pajkossy, *Electrochimica Acta*, **47**, 2055 (2002)

[92] V. A. Alves and C. M. A. Brett, *Electrochimica Acta*, **47**, 2081 (2002)

[93] I. Betova, M. Bojinov, P. Kinnunen, T. Laitinen, P. Pohjanne and T. Saario, *Electrochimica Acta*, **47**, 2093 (2002)

[94] M. M. Lohrengel, S. Heiroth, K. Kluger, M. Pilaski and B. Walther, *Electrochimica Acta*, **51**, 1431 (2006)

[95] R. M. Souto, L. Fernandez-Merida, S. Gonzalez and D. J. Scantlebury, *Corrosion Sci.*, **48**, 1182 (2006)

[96] F. Mansfeld, *J. Appl. Electrochem.*, **25**, 1145 (1995)

[97] D. M. Brasher and A. H. Kingsbury, *Journal of Applied Chemistry*, **4**, 62 (1954)

[98] E. P. M. van Westing, G. M. Ferrari and J. H. W. de Wit, *Corrosion Sci.*, **36**, 957 (1994)

[99] L. D. Rosa, T. Monetta and F. Bellucci, *Materials Science Forum*, **289-292**, 315 (1998)

[100] A. S. Castela and A. M. Simoes, *Corrosion Sci.*, **45**, 1631 (2003)

[101] A. S. Castela and A. M. Simoes, *Corrosion Sci.*, **45**, 1647 (2003)

[102] J. T. Zhang, J. M. Hu, J. Q. Zhang and C. N. Cao, *Progress in Organic Coatings*, **51**, 145 (2004)

[103] H. Marchebois, C. Savall, J. Bernard and S. Touzain, *Electrochimica Acta*, **49**, 2945 (2004)

[104] A. Meroufel and S. Touzain, *Progress in Organic Coatings*, **59**, 197 (2007)

[105] A. Meroufel, C. Deslouis and S. Touzain, *Electrochimica Acta*, **53**, 2331 (2008)

[106] M. Ohman and D. Persson, *Electrochimica Acta*, **52**, 5159 (2007)

[107] M. Ohman, D. Persson and C. Leygraf, *Electrochem. Solid State Lett.*, **10**, C27 (2007)

[108] R. Vlasak, I. Klueppel and G. Grundmeier, *Electrochimica Acta*, **52**, 8075 (2007)

[109] H. Vogel, *Gerthsen Physik*, p. 1262, Springer, Berlin (1997)

[110] A. J. Bard and L. R. Faulkner, *Electrochemical Methods Fundamentals and Application*, p. 833, John Wiley & Sons, Hoboken (2001)

[111] J. R. Macdonald, *Impedance Spectroscopy*
Emphasizineg solid Materials ad Systems, p. 346, John Wiley & Sons, New York (1987)

[112] Gamry, Basics of Electrochemical Impedance Spectroscopy, in (2008)

[113] D. Loveday, P. Peterson and B. Rodgers, *Jct Coatingstech*, **1**, 46 (2004)

[114] D. Loveday, P. Peterson and B. Rodgers, *Jct Coatingstech*, **2**, 22 (2005)

[115] C. Gabrielli, *Identification of Electrochemical Processes by Frequency Response Analysis*, p. 94, Paris

[116] G. W. Walter, *Corrosion Sci.*, **26**, 681 (1986)

[117] R. Hirayama and S. Haruyama, *Corrosion*, **47**, 952 (1991)

[118] E. P. M. van Westing, G. M. Ferrari and J. H. W. de Wit, *Corrosion Sci.*, **34**, 1511 (1993)

[119] W. D. Hinsberg and K. K. Kanazawa, *Review of Scientific Instruments*, **60**, 489 (1989)

[120] K. K. Kanazawa and O. R. Melroy, *Ibm Journal of Research and Development*, **37**, 157 (1993)

[121] G. Sauerbrey, *Zeitschrift Fur Physik*, **155**, 206 (1959)

[122] Maxtec, Maxtek RQCM Quartz Crystal Microbalance Research System Manual, in (2005)

[123] G. T. Fieldson and T. A. Barbari, *Polymer*, **34**, 1146 (1993)

[124] M. Ohman, D. Persson and C. Leygraf, *Progress in Organic Coatings*, **57**, 78 (2006)

[125] K. Wapner, M. Stratmann and G. Grundmeier, *Electrochimica Acta*, **51**, 3303 (2006)

[126] T. Sueoka, J. Inukai and M. Ito, *Journal of Electron Spectroscopy and Related Phenomena*, **64-5**, 363 (1993)

[127] E. Johnson and R. Aroca, *Journal of Physical Chemistry*, **99**, 9325 (1995)

[128] A. Bruckbauer and A. Otto, *J. Raman Spectrosc.*, **29**, 665 (1998)

[129] K. Ataka and M. Osawa, *Journal of Electroanalytical Chemistry*, **460**, 188 (1999)

[130] J. K. Lim and S. W. Joo, *Surf. Interface Anal.*, **39**, 684 (2007)

[131] R. A. Gu, X. Y. Shen, G. K. Liu, B. Ren and Z. Q. Tian, *J. Phys. Chem. B*, **108**, 17519 (2004)

[132] D. Gonnissen, A. Hubin and J. Vereecken, *Electrochimica Acta*, **44**, 4129 (1999)

[133] H. F. Yang, X. J. Sun, J. Zhu, J. H. Ji, X. L. Ma and Z. R. Zhang, *J. Phys. Chem. C*, **111**, 7986 (2007)

[134] G. Wedler, *Lehrbuch der physikalischen Chemie*, Wiley VCH (1997)

[135] M. Hesse, H. Meier and B. Zeeh, *Spektroskopische Methoden in der organischen Chemie*, Georg Thieme Verlag, Stuttgart (1991)

[136] P. W. Atkins, *Physikalische Chemie*, p. 1106, VCH, Weinheim (1996)

[137] G. Wedler, *Lehrbuch der Physikalischen Chemie*, p. 924, VCH, Weinheim (1987)

[138] E. Almeida, M. Balmayore and T. Santos, *Progress in Organic Coatings*, **44**, 233 (2002)

[139] J. Grdadolnik, *Acta Chimica Slovenica*, **49**, 631 (2002)

[140] M. Milosevic, *Appl. Spectrosc. Rev.*, **39**, 365 (2004)

[141] K. Herzog, S. Salzer and B. Ziegler, In-situ Untersuchungen thermischer Vorgänge in Polymeren mittels Kopplung von FTIR-Spektroskopie und Differenz-Thermo Analyse (DTA), in, TU, Institut für Analytische Chemie, Dresden

[142] M. Fleischmann, P. J. Hendra and McQuilla.Aj, *Chemical Physics Letters*, **26**, 163 (1974)

[143] A. Otto, I. Mrozek, H. Grabhorn and W. Akemann, *Journal of Physics-Condensed Matter*, **4**, 1143 (1992)

[144] A. Otto, *Physica Status Solidi a-Applied Research*, **188**, 1455 (2001)

[145] R. Aroca, *Surface-Enhanced Vibrational Spectroscopy*, Wiley, West Sussex (2006)

[146] G. Bertsche, Das Rasterelektronenmikroskop, in

[147] H. Jaksch and J.-P. Vermeulen, New developments in FESEM Technology, in

[148] C. A. Volkert and A. M. Minor, *MRS Bull.*, **32**, 389 (2007)

[149] W. J. MoberlyChan, D. P. Adams, M. J. Aziz, G. Hobler and T. Schenkel, *MRS Bull.*, **32**, 424 (2007)

[150] T. Suter and H. Bohni, *Electrochimica Acta*, **42**, 3275 (1997)

[151] T. Suter and H. Bohni, *Electrochimica Acta*, **47**, 191 (2001)

[152] M. M. Lohrengel, C. Rosenkranz, I. Kluppel, A. Moehring, H. Bettermann, B. Van den Bossche and J. Deconinck, *Electrochimica Acta*, **49**, 2863 (2004)

[153] M. Pilaski, T. Hamelmann, A. Moehring and M. M. Lohrengel, *Electrochimica Acta*, **47**, 2127 (2002)

[154] N. Birbilis, B. N. Padgett and R. G. Buchheit, *Electrochimica Acta*, **50**, 3536 (2005)

[155] M. M. Lohrengel, A. Moehring and M. Pilaski, *Fresenius Journal of Analytical Chemistry*, **367**, 334 (2000)

[156] G. G. Sun and G. Grundmeier, *Thin Solid Films*, **515**, 1266 (2006)

[157] A. W. Hassel, K. Fushimi and M. Seo, *Electrochem. Commun.*, **1**, 180 (1999)

[158] A. Losch, J. W. Schultze and H. D. Speckmann, *Applied Surface Science*, **52**, 29 (1991)

[159] X. G. Zhang, *Corrosion and Electrochemistry of Zinc*, p. 474, Plenum

[160] M. Pourbaix, *Atlas of Electrochemical Equilibria in Aqueous Solutions.*, NACE (National Association of Corrosion Engineers), Houston (1974)

[161] K. Wapner and G. Grundmeier, *Adv. Eng. Mater.*, **6**, 163 (2004)

[162] M. L. Abel, A. Rattana and J. F. Watts, *J. Adhes.*, **73**, 313 (2000)

[163] Z. D. Q. van Ooij W. J., Prasad G., Jayaseelan S., Fu Y., Teredesai N., *Surface Engineering*, **16**, 386 (2000)

[164] M. L. Abel, J. F. Watts and R. P. Digby, *J. Adhes.*, **80**, 291 (2004)

[165] T. Falk, J. E. Svensson and L. G. Johansson, *J. Electrochem. Soc.*, **145**, 2993 (1998)

[166] R. Lindstrom, J. E. Svensson and L. G. Johansson, *J. Electrochem. Soc.*, **147**, 1751 (2000)

[167] N. Sandhyarani, G. Skanth, S. Berchmans, V. Yegnaraman and T. Pradeep, *Journal of Colloid and Interface Science*, **209**, 154 (1999)

[168] I. Gaussian, Gaussian 03, in, Gaussian, Inc., Wallingford (2008)

[169] G. Decher and J. B. Schlenoff, *Multilayer Thin Filmy*, Wiley-VCH, Weinheim (2003)

[170] V. Barranco, P. Thiemann, H. K. Yasuda, M. Stratmann and G. Grundmeier, *Applied Surface Science*, **229**, 87 (2004)